ISSN 2074-272X

науково-практичний журнал 2021/2

Електротехніка і Електромеханіка

Electrical Engineering & Electromechanics

Електричні машини та апарати
Електротехнічні комплекси та системи
Силова електроніка
Теоретична електротехніка
Електричні станції, мережі і системи

Журнал включено до найвищої категорії «А» Переліку фахових видань України

З 2015 р. журнал індексується у міжнародній наукометричній базі Web of Science Core Collection: Emerging Sources Citation Index

«ELECTRICAL ENGINEERING & ELECTROMECHANICS»

Scientific Journal was founded in 2002

Founders are:

National Technical University «Kharkiv Polytechnic Institute» (Kharkiv, Ukraine)

State Institution «Institute of Technical Problems of Magnetism of the NAS of Ukraine» (Kharkiv, Ukraine)

Journal «Electrical Engineering & Electromechanics» from no. 1 2015 is indexing in Web of Science Core Collection : Emerging Sources Citation Index (ESCI).

Also included in DOAJ (Directory of Open Access Journals), in EBSCO's database, in ProQuest's databases – Advanced Technologies & Aerospace Database and Materials Science & Engineering Database, in Gale/Cengage Learning databases.

Editorial office address:

National Technical University «Kharkiv Polytechnic Institute», Kyrpychova Str., 2, Kharkiv, 61002, Ukraine

phones: +380 57 7076281, +380 67 3594696, **e-mail:** a.m.grechko@gmail.com (**Grechko O.M.)**

ISSN (print) 2074-272X

ISSN (online) 2309-3404

Printed 05 April 2021. Format 60 × 90 ⅛. Paper – offset. Laser printing. Edition 200 copies.

Printed by Printing house «Madrid Ltd» (18, Gudanova Str., Kharkiv, 61024, Ukraine)

ELECTRICAL ENGINEERING & ELECTROMECHANICS
Scientific journal

no. 2, 2021

TABLE OF CONTENTS

Electrical Machines and Apparatus

Electrotechnical Complexes and Systems

Power Electronics

Theoretical Electrical Engineering

Power Stations, Grids and Systems

UDC 621.313.8 **doi: 10.20998/2074-272X.2021.2.01**

B.G. Liubarskyi, L.V. Overianova, Ie.S. Riabov, D.I. Iakunin, O.O. Ostroverkh, Y.V. Voronin

ESTIMATION OF THE MAIN DIMENSIONS OF THE TRACTION PERMANENT MAGNET-ASSISTED SYNCHRONOUS RELUCTANCE MOTOR

Goal. *The goal of the research is to develop an algorithm for selecting the main dimensions of a traction permanent magnet-assisted synchronous reluctance motor.* ***Methodology.*** *A method for determining the main dimensions of the motor, which combines the analytical selection of stator parameters and numerical field calculations for the selection of rotor parameters. The need to check the mechanical strength of a rotor with permanent NdFeB magnets in flux barriers is shown.* ***Results****. The article proposes an algorithm for selecting the main dimensions of a traction permanent magnet-assisted synchronous reluctance motor, which combines analytical expressions for selecting stator parameters and numerical field calculations for selecting rotor parameters. It is determined that analytical methods for calculating the magnetic circuit need to be developed in order to reduce the time to select the main dimensions of the motor.* ***Originality.*** *For the first time the sizes of active parts of the permanent magnet-assisted synchronous reluctance motor with power of 180 kW for the drive of wheels of the trolleybus are defined.* ***Practical significance.*** *As a result of research the sizes of active parts, stator winding data and a design of a rotor of the electric motor are defined. The obtained results can be applied when creating an electric motor for a trolleybus.* References 17, tables 3, figures 5.

Key words: **permanent magnet-assisted synchronous reluctance motor, traction electric drive, permanent magnet, energy efficiency.**

У статті розглянуті питання проектування тягового синхронно-реактивного електродвигуна з постійними магнітами потужністю 180 кВт для приводу коліс тролейбуса. Запропоновано спосіб визначення головних розмірів електродвигуна, який поєднує аналітичний вибір параметрів статора та чисельно-польові розрахунки для вибору параметрів ротора. Показана необхідність перевірки механічної міцності ротора, в якому розташовано постійні магніти NdFeB у потокових бар'єрах. У результаті дослідження визначено розміри активних частин, обмоткові дані статора та конструктив ротора електродвигуна. Бібл. 17, табл. 3, рис. 5.

Ключові слова: **синхронно-реактивний двигун з постійними магнітами, тяговий електропривод, постійний магніт, енергоефективність.**

В статье рассмотрены вопросы проектирования тягового синхронно-реактивного электродвигателя с постоянными магнитами мощностью 180 кВт для привода колес троллейбуса. Предложен способ определения главных размеров электродвигателя, который сочетает аналитический выбор параметров статора и численно-полевые расчеты для выбора параметров ротора. Показана необходимость проверки механической прочности ротора, в котором расположено постоянные магниты NdFeB в потоковых барьерах. В результате исследования определены размеры активных частей, обмоточные данные статора и конструктив ротора электродвигателя. Библ. 17, табл. 3, рис. 5.

Ключевые слова: **синхронно-реактивный двигатель с постоянными магнитами, тяговый электропривод, постоянный магнит, энергоэффективность.**

Introduction. At present, the worldwide practice is the use of traction electric drives with induction electric motors on the rolling stock of railways, industrial and urban transport [1-3]. In Ukraine, large-scale traction induction electric drives are used in the rolling stock of urban electric transport and main railways [4]. The main advantages of the traction induction electric drive are high energy and mass-size indicators, high level of reliability, simplicity of design, long service life [5]. However, the requirements for reducing energy and resource consumption of rolling stock pose a task to the scientific and technical community both to the further improvement of traction induction electric drives, and the development and research of other types of electric drives [6]. An alternative approach to increase the efficiency of the traction electric drive is the use of synchronous motors with excitation from permanent magnets [7], but the large mass of high-coercive permanent magnets significantly increases the cost of production of such electric motors.

Analysis of literature data and problem definition. A specific feature of the traction drive is a wide range of speed and torque control, and therefore, it is important to ensure high energy performance of the traction drive in different operating modes. According to various authors, such characteristics are provided by permanent magnet-assisted synchronous reluctance motors (PMSynRM, PMA-SynRel) [8-12]. The weight and size of the motor of this type are comparable to an induction motor, and therefore the traction drive based on a permanent magnet-assisted synchronous reluctance motor is a «direct alternative» to the traction induction electric drive.

PMSynRM is a synchronous reluctance motor (SynRM) with permanent magnets inside the rotor. The configuration of a typical PMSynRM is shown in Fig. 1 [8-10].

In this motor, as a rule, a distributed stator winding is used [10, 11]. To increase the use of reactive torque, in

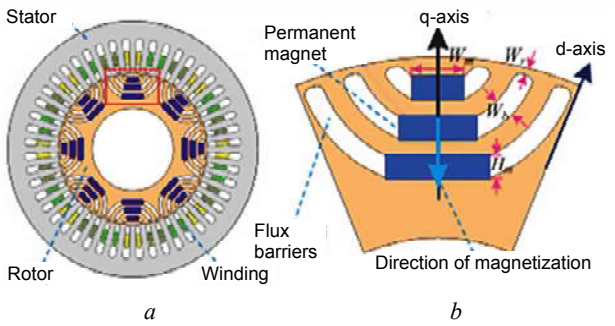

Fig. 1. PMSynRM configuration (*a*) and rotor section (*b*). Marked: W_r, W_b, W_m, H_m – tangential ribs, flux barriers, width and height of permanent rotor magnets, respectively

the radial direction of the rotor after another channels of flux barriers are placed one after another. A feature of the rotor is the presence of permanent magnets (rare earth magnets such as NdFeB, ferrite Y30) inserted into its flux barriers [11-13]. The permanent magnets are uniformly magnetized and form the *q*-axis of the rotor. Because permanent magnets have about the same permeability as air, they create a path with high resistance and magnetic anisotropy in the *q*-axis direction. The steel part of the rotor is formed by small segments isolated from each other by flux barriers. These segments provide a path with low flux resistance along the *d*-axis. To ensure the strength of the rotor structure, it is necessary that the ferromagnetic segments are internally connected to each other, so the rotor structure uses tangential ribs near the air gap with thickness W_r [14]. Due to the installation of permanent magnets, the tangential ribs are saturated during normal operation of the motor and therefore magnetically insulate various steel segments [14]. From the point of view of creating torque, the scattering of the flux caused by tangential ribs should be minimal [11].

A review of publications [10-14] shows that the determination of the dimensions and parameters of electric motors is carried out by numerical field calculations in combination with multicriteria optimization. The varied parameters are usually the geometric dimensions of the elements of the magnetic core. At the same time, since the PMSynRM stator is similar to the stator of an AC motor, it is obvious that the optimization model can be simplified by applying classical methods for calculating the magnetic circuit of electric machines for the stator, and using numerical calculations only to determine the motor's rotor configuration. In addition, this decomposition allows to estimate the size of the active parts of the motor and its fit into the allotted mounting space without numerical calculations of the magnetic field, resulting in a set of allowable geometric stator parameters.

The goal of the work is the development of an algorithm for selecting the main dimensions of a traction permanent magnet-assisted synchronous reluctance motor.

The aim of the study is the adaptation of methods for selecting the main sizes of electric machines for their application to PMSynRM.

A technique for choosing the main dimensions of PMSynRM. The main dimensions of an electric machine are the diameter of the armature or the diameter of the stator bore and their axial length. These dimensions depend on the power, rotation speed and a number of indicators that characterize the use of active parts of electric machines [5]. Features of traction electric machines are, firstly, the regulation of rotation speed in a wide range (the ratio of maximum rotation speed to nominal one can be from 3 to 5 times, and the ratio of maximum torque to nominal one – up to 2 times), and, secondly, restrictions of overall dimensions associated with the placement of the electric machine on the vehicle and its arrangement in the transmission. This in most cases makes it impossible to use the Arnold constant to determine the main dimensions of traction electric machines, so there are special procedures developed for them [3, 5]. With this in mind, it is advisable to use this approach to select the main sizes of PMSynRM.

The number of pole pairs is determined from the condition of ensuring the maximum rotation speed at the highest frequency of the supply voltage:

$$p = \frac{60 f_{\max}}{n_{\max}}, \qquad (1)$$

where $f_{\max}$ is the highest supply frequency; $n_{\max}$ is the highest rotation speed.

Since the traction motor must have a high degree of protection, which is adopted in order to prevent dirt from entering the air gap between the stator and the rotor, cooling of the electric motor is possible only through the axial ventilation ducts in the stator. In the caseless design, the axial channels are made directly in the stator sheet, for example, by stamping. In the case of the stator housing, the axial ventilation channels of the stator are formed by the motor housing, to which the ribs for laminating the stator core are welded, and the outer surface of the stator core. Regardless of the method of formation of axial ventilation ducts, their radial size (diameter or height) can be taken equal to 12–20 mm (smaller values– in the case of the housing). Adding to this size the thickness of the housing of 8–10 mm and technological reserves for the manufacture of holes, we obtain the outer diameter of the stator magnetic core (calculated diameter of the active part). This value is subject to specification based on the results of calculations and design processing of the electric motor.

The inner diameter of the stator D_i (diameter of the «bore») is determined by the expression

$$D_i = K \cdot D_a, \qquad (2)$$

where K is the coefficient equal to, for example, 0.55–0.65 at $2p = 4$, p is the number of pole pairs, D_a is the calculated diameter.

To estimate the length of the stator magnetic core, calculate the departure of the front parts of the stator winding by expression

$$L_v = (0{,}12 + 0{,}15p)\cdot \tau_k + 10, \quad (3)$$

where τ_k is the average width of the stator coil.

Approximately the average width of the stator coil can be determined by expression

$$\tau_k = \beta \frac{Z}{2p} t_{av1}, \quad (4)$$

where β is the reduction of the winding step (approximately assumed to be equal to 0,8); Z is the number of slots in the stator; t_{av1} is the toothed step in the middle of the height of the slot.

The largest number of slots is determined from the expression

$$Z = \frac{(0{,}3\ldots 0{,}4)\pi D_i}{b_z}, \quad (5)$$

where b_z is the width of the stator tooth, which must be at least 5–7 mm;

$$t_{av1} = \frac{\pi(D_i + h_n)}{Z}, \quad (6)$$

where h_n is the height of the slot which is determined by the expression

$$h_n = (3\ldots 4)b_n, \quad (7)$$

where b_n is the width of the slot which is equal to

$$b_n = t_{z1} - b_z, \quad (8)$$

where t_{z1} is toothed step on the inner diameter of the stator

$$t_{z1} = \frac{\pi D_i}{Z}. \quad (9)$$

The size of the axial length of the stator on the front parts

$$L_l = (0{,}7\ldots 0{,}8)L_k, \quad (10)$$

where L_k is the body length (distance between the planes of bearing plates).

The axial length of the stator magnetic core is determined by the expression

$$L_i = L_l - L_v. \quad (11)$$

The phase current of the motor is predetermined by the expression

$$I_{ph} = \frac{P\cdot 10^3}{3\cdot U_{ph}\cdot \eta \cdot \cos\varphi}, \quad (12)$$

where P is the nominal power; U_{ph} is the nominal phase voltage; η is efficiency (approximately 0.93–0.95); cos φ is the power factor (approximately 0.8–0.9).

The magnetic flux of the motor is pre-determined by the expression

$$\Phi = \alpha B_\delta \tau L_i, \quad (13)$$

where α is the coefficient of the pole arc (take equal to $2/\pi$); B_δ is the magnetic flux density in the air gap (take no more than 1 T); τ is the pole division.

The pole division is determined by the expression

$$\tau = \frac{\pi D_i}{2p}. \quad (14)$$

The number of turns in the phase of the stator winding is determined by the expression

$$w = \frac{(0{,}95\ldots 0{,}98)U_{ph}}{4{,}44\Phi f_{nom} k_{w1}}, \quad (15)$$

where U_{ph} is the phase voltage; k_{w1} is the winding coefficient (take equal to 0,9); f_{nom} is the nominal voltage frequency

$$f_{nom} = \frac{pn_{nom}}{60}, \quad (16)$$

where n_{nom} is the nominal rotation speed of the motor.

The number of effective conductors in the slot

$$s_n = \frac{2maw}{Z}, \quad (17)$$

where m is the number of phases of the motor (equal to 3); a is the number of parallel branches (the current of the parallel branch should not exceed 400 A).

It is advisable to choose the number of parallel branches from the condition of providing a whole number of slots per pole and phase

$$q = \frac{Z}{2pma}. \quad (18)$$

Preliminary assessment of the rotor configuration (number of flux barriers, geometric dimensions of permanent magnets) is performed by calculating the magnetic circuit of the motor using substitution circuits. The criterion for selecting a configuration option is to provide nominal torque at nominal phase current. The values of magnetic flux density in the parts of the magnetic core are analyzed and, if necessary, its geometric dimensions are adjusted.

When calculating the parameters of permanent magnets are taken according to the data given in Table 1.

Table 1

Parameters of permanent magnets

Name	Unit	Value
Material of magnets		NdFeB
Remanent flux density	T	1,0
Coercive force	kA/m	850

The next step is to calculate the magnetic field of the motor in the FEMM environment, which clarifies the results of the previous calculation [15-17].

Auxiliary criteria when choosing the configuration of the rotor are to ensure its mechanical strength, as well as satisfactory results of thermal calculation of the electric motor.

As an example, consider the procedure for selecting the main dimensions of PMSynRM to drive the wheels of a trolleybus with the technical parameters listed in Table 2. Technical parameters correspond to traction induction electric motors used in trolleybuses.

Table 2

Technical parameters of PMSynRM

Name	Unit	Value
Power	kW	180
Linear voltage	V	400
Phase current	A	350
Nominal rotation speed	Rpm	1500
Torque	Nm	1110
Maximum rotation speed	Rpm	4000
Maximum supply frequency	Hz	150

The selection criterion is to ensure the torque 1100 Nm at phase current of 350 A. From the analysis of designs of similar induction motors (AD903, DTA-1, 6DTA.002.1) we find that the external diameter of the electric motor should not exceed 500 mm, axial length on the case – 700 mm.

The procedure for determining the main dimensions of the traction PMSynRM is a series of calculations, which consist of calculations by analytical expressions (1) – (17), magnetic field calculations in FEMM environment (Fig. 2) and rotor strength calculations (Fig. 3). The calculations were performed for several values of the number of stator slots, after which the number of effective conductors in the slot was determined. After that, the calculations of the magnetic circuit of the stator were performed to assess the magnetic flux density in the teeth and the yoke (permissible values – not more than 1.7 T. In case of excess –the geometric dimensions of the slots were adjusted). Next, a sketch of the cross section of the motor was developed to calculate the magnetic field in the FEMM environment. Calculations were performed for rotor configuration options with two and three pairs of flux barriers. The thickness of the flux barrier was assumed to be 10 mm. The distance between the flux barriers in one layer is 5 mm. All flux barriers contain permanent magnets with parameters according to Table 1. The calculation of the magnetic field of the electric motor is performed for the stator current 350 A, according to which, taking into account the scheme of the stator winding, the magnetomotive force of the conductors of the stator winding is calculated. Calculations are performed for several positions of the rotor. For calculation options where the electromagnetic torque reaches more than 1100 Nm, calculations of a rotor on strength at frequency of rotation of 4800 rpm are carried out. If the mechanical strength of the rotor is provided (it is assumed that the safety factor should be greater than 2), the option is accepted as working.

After performing the above series of calculations, the configuration of PMSynRM was determined which satisfies the technical parameters specified in Table 2.

The stator data are given in Table 3, the results of the calculation of the magnetic field – in Fig. 2, the results of the calculation of the rotor on strength – in Fig. 3. The sketch of the rotor is shown in Fig 4, the dependence of the torque of the motor on the angle of rotation of the rotor – in Fig. 5.

Table 3

Stator data

Name	Value
Number of slots	36
Number of effective conductors in the slot	6
Number of parallel branches	1
Step reduction ratio	0,778
Number of elementary conductors in the effective one	3 (in height)
Step on the slots	1-8-19
Connection of phases – «star»	
Calculated outer diameter of the stator, m	0,46
Boring diameter, m	0,3
Axial length of the magnetic core, m	0,3
One-side air gap, m	0,001
Dimensions of the stator winding conductor (without insulation), mm	1,6×12,5
Slot height, m	0,040
Slot width, m	0,0145

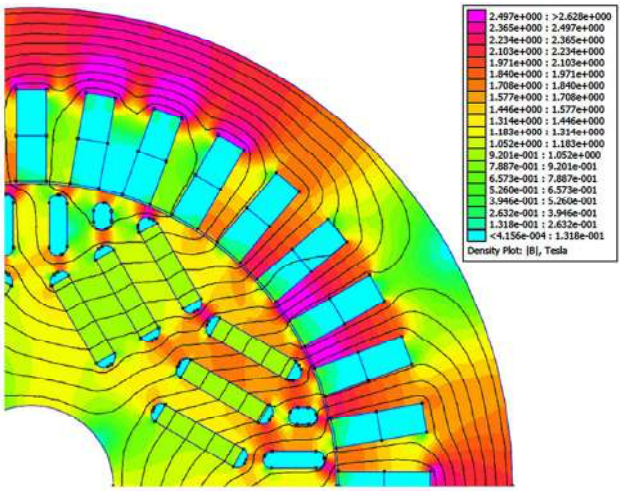

Fig. 2. Results of the calculation of the magnetic field in FEMM

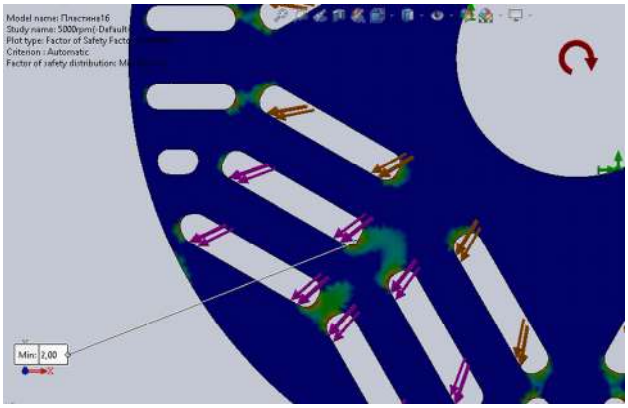

Fig. 3. Results of the calculation of the rotor on strength in SolidWorks Simulation

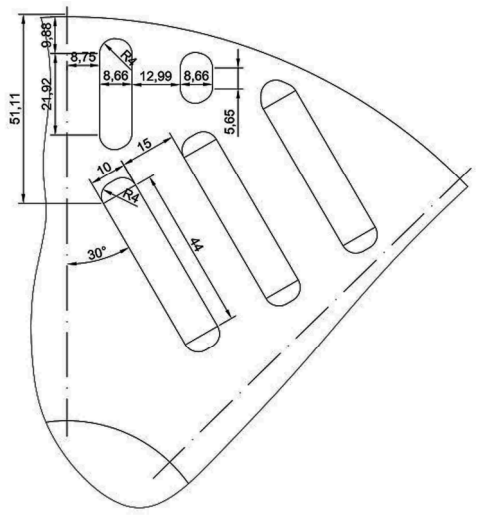

Fig. 4. Sketch of the PMSynRM rotor

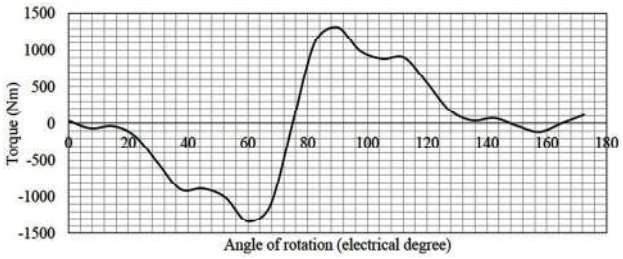

Fig. 5. Dependence of the torque on the angle of rotation of the rotor

As it can be seen from Fig. 5, the required torque equal to 1100 Nm is achieved by the calculated configuration of the active parts of the motor. However, it should be noted that in the given example of the PMSynRM configuration, the maximum torque of the electric motor does not significantly exceed the nominal torque, which can negatively affect the performance of the traction drive of the trolleybus.

Discussion of results. The proposed technique allowed to determine the parameters of the PMSynRM stator analytically, which reduced the number of options for numerical field calculations. The technique was tested in the calculation of PMSynRM with power of 180 kW for the drive of trolleybus wheels. In order to further reduce the numerical field calculations, it is advisable to analytically determine the parameters for assessing the performance of the electric motor. It is necessary to define and apply in the developed methodology criteria that take into account the frequency control of the motor.

Conclusions.

1. The paper proposes an algorithm for selecting the main dimensions of a traction permanent magnet-assisted synchronous reluctance motor which combines analytical expressions for selecting stator parameters and numerical field calculations for selecting rotor parameters. The technique was tested in determining the configuration of PMSynRM with power of 180 kW.

2. It is determined that analytical methods for calculating the magnetic circuit need to be developed in order to reduce the time for choosing the main dimensions of the electric motor.

3. Techniques of heat-ventilation calculations of a traction permanent magnet-assisted synchronous reluctance electric motor and methods of calculation of its characteristics, based on the results of which a decision is made on the conformity of the electric motor to technical requirements, need to be developed.

Conflict of interest. The authors declare no conflict of interest.

REFERENCES

1. Luvishis A.L. Asynchronous drive: the beginning of the path. *Lokomotiv*, 2017, no. 1 (721), pp .44-46. (Rus).

2. Luvishis A.L. New locomotives of the US railways. *Railway transport*, 2018, no. 8, pp. 70-77. (Rus).

3. Lyubarsky B.G. *Teoretychni osnovy dlia vyboru ta otsinky perspektyvnykh system elektromekhanichnoho peretvorennia enerhii elektrorukhomoho skladu: dys. dokt. tekhn. nauk* [Theoretical bases for a choice and an estimation of perspective systems of electromechanical conversion of energy of an electric rolling stock: Dr. tech. sci. dissertation]. Kharkiv, NTU «KhPI», 2014. 368 p. (Ukr).

4. Yatsko S., Sytnik B., Vashchenko Y., Sidorenko A., Liubarskyi B., Veretennikov I., Glebova M. Comprehensive approach to modeling dynamic processes in the system of underground rail electric traction. *Eastern-European Journal of Enterprise Technologies*, Jan. 2019, vol. 1, no. 9 (97), pp. 48-57. doi: https://doi.org/10.15587/1729-4061.2019.154520.

5. Bezruchenko V.M., Varchenko V.K., Chumak V.V. *Tiahovi elektrychni mashyny elektrorukhomoho skladu* [Traction electric machines of electro-rolling stock]. Dnipropetrovsk, DNUZT Publ., 2003. 252 p. (Ukr).

6. Yatsko S., Sidorenko A., Vashchenko Ya., Lyubarskyi B., Yeritsyan B. Method to improve the efficiency of the traction rolling stock with onboard energy storage. *International journal of renewable energy research*, 2019, vol. 9, no. 2, pp. 848-858. Available at: https://www.ijrer.org/ijrer/index.php/ijrer/article/view/9143/pdf (Accessed 15.08.2020).

7. Liubarskyi B., Demydov A., Yeritsyan B., Nuriiev R., Iakunin D. Determining electrical losses of the traction drive of electric train based on a synchronous motor with excitation from permanent magnets. *Eastern-European Journal of Enterprise Technologies*, Apr. 2018, vol. 2, no. 9 (92), pp. 29-39. doi: https://doi.org/10.15587/1729-4061.2018.127936.

8. Stipetic S., Zarko D., Kovacic M. Optimised design of permanent magnet assisted synchronous reluctance motor series using combined analytical–finite element analysis based approach. *IET Electric Power Applications*, May 2016, vol. 10, no. 5, pp. 330-338. doi: https://doi.org/10.1049/iet-epa.2015.0245.

9. Haataja J., Pyrhönen J. Permanent magnet assisted synchronous reluctance motor: an alternative motor in variable speed drives. In: Parasiliti F., Bertoldi P. (eds) *Energy Efficiency in Motor Driven Systems*, 2003. Springer, Berlin, Heidelberg. doi: https://doi.org/10.1007/978-3-642-55475-9_16.

10. Krause P.C., Wasynczuk O., Pekarek S.D. *Electromechanical Motion Devices. 2nd ed.* 2012, Wiley-IEEE, 544 p.

11. Viego-Felipe P.R., Gómez-Sarduy J.R., Sousa-Santos V., Quispe-Oqueña E.C. Motores sincrónicos de reluctancia

asistidos por iman permanente: Un nuevo avance en el desarrollo de los motores eléctricos. *Ingeniería, investigación y tecnología*, Jul. 2018, vol. 19, no. 3, pp. 269-279. doi: https://doi.org/10.22201/fi.25940732e.2018.19n3.023. (Esp).

12. Wu W., Zhu X., Quan L., Du Y., Xiang Z., Zhu X. design and analysis of a hybrid permanent magnet assisted synchronous reluctance motor considering magnetic saliency and PM usage. *IEEE Transactions on Applied Superconductivity*, April 2018, vol. 28, no. 3, pp. 1-6, art no. 5200306. doi: https://doi.org/10.1109/tasc.2017.2775584.

13. Reza R. Moghaddam. *Synchronous Reluctance Machine (SynRM) in Variable Speed Drives (VSD) Applications – Theoretical and Experimental Reevaluation. Doctoral Thesis*. Royal Institute of Technology, Stockholm, Sweden, 2011, 260 p. Available at : http://www.diva-portal.org/smash/get/diva2:417890/FULLTEXT01.pdf (Accessed 21.09.2020).

14. Dehghani Ashkezari J., Khajeroshanaee H., Niasati M., Jafar Mojibian M. Optimum design and operation analysis of permanent magnet-assisted synchronous reluctance motor. *Turkish journal of electrical engineering & computer sciences*, 2017, vol. 25, pp. 1894-1907. doi: https://doi.org/10.3906/elk-1603-170.

15. Juergens J., Fricassè A., Marengo L., Gragger J., De Gennaro M., Ponick B. Innovative design of an air cooled ferrite permanent magnet assisted synchronous reluctance machine for automotive traction application. *2016 XXII International Conference on Electrical Machines (ICEM)*, Lausanne, Switzerland, 2016, pp. 803-810. doi: https://doi.org/10.1109/icelmach.2016.7732618.

16. Trancho E., Ibarra E., Arias A., Kortabarria I., Jurgens J., Marengo L., Fricasse A., Gragger J.V. PM-Assisted Synchronous Reluctance Machine Flux Weakening Control for EV and HEV Applications. *IEEE Transactions on Industrial Electronics*, April 2018, vol. 65, no. 4, pp. 2986-2995. doi: https://doi.org/10.1109/tie.2017.2748047.

17. *Finite Element Method Magnetics*. Available at: https://www.femm.info/wiki/HomePage (accessed 15.06.2020).

Received 22.12.2020
Accepted 07.02.2021
Published 05.04.2021

B.G. Liubarskyi [1], *Doctor of Technical Science, Professor,*
L.V. Overianova[1], *PhD, Associate Professor,*
Ie.S. Riabov [1], *PhD, Senior Researcher,*
D.I. Iakunin [1], *PhD, Associate Professor,*
O.O. Ostroverkh [1], *PhD,*
Y.V. Voronin[2] ,
[1] National Technical University «Kharkiv Polytechnic Institute», 2, Kyrpychova Str., Kharkiv, 61002, Ukraine,
e-mail: lboris1911@ukr.net, overanova@ukr.net, riabov.ievgen@gmail.com, unicomber@ukr.net, ostrov.sasha@gmail.com
[2] JSC «Electromashina», 106, Ozeryanskaya Str., Kharkiv, 61016, Ukraine,
e-mail: designer.voronin@gmail.com

How to cite this article:
Liubarskyi B.G., Overianova L.V., Riabov Ie.S., Iakunin D.I., Ostroverkh O.O., Voronin Y.V. Estimation of the main dimensions of the traction permanent magnet-assisted synchronous reluctance motor. *Electrical Engineering & Electromechanics*, 2021, no. 2, pp. 3-8. **doi: 10.20998/2074-272X.2021.2.01.**

UDC 621.313.33 **doi: 10.20998/2074-272X.2021.2.02**

V.S. Malyar, O.Ye. Hamola, V.S. Maday, I.I. Vasylchyshyn

MATHEMATICAL MODELLING OF STARTING MODES OF INDUCTION MOTORS WITH SQUIRREL-CAGE ROTOR

Purpose. *Development of methods and algorithms for calculation of starting modes of the induction motors with the squirrel-cage rotor.* ***Methodology.*** *Mathematical modelling of starting modes of asynchronous electric drives in various coordinate systems with the use of numerical methods for solving boundary problems for systems of differential equations and nonlinear systems of final equations and calculation with their use of static characteristics.* ***Results.*** *Methods and algorithms for numerical analysis of the starting modes of asynchronous electric drive have been developed, which make it possible to calculate the static characteristics and transients in fixed three-phase and orthogonal two-phase coordinate systems.* ***Academic novelty.*** *Known in the literature methods of calculation of starting modes have in their basis classical equivalent circuits with different approximate methods of calculating the parameters taking into account the saturation of a magnetic core and current displacement in a rotor winding. This approach requires a special solution of the adequacy problem for each problem. The methods described in the article for the saturation accounting use real magnetization characteristics of the main magnetic flux and leakage fluxes separately, and the skin effect phenomenon is taken into account by representing the squirrel-cage rotor winding as multilayer. Such mathematical model of the motor is universal and makes it possible to take into account the saturation and current displacement in any dynamic mode, including the start-up process. Mathematical models developed on the basis of the proposed methods provide the adequacy of results with a minimum amount of calculations and make it possible to perform optimization calculations.* ***Practical value****. Created on the basis of developed algorithms calculation programs allow to carry out with high reliability calculation of starting modes both in three-phase and two-phase axes of coordinates that gives the chance to analyze not only symmetric, but also asymmetric modes and to predict special features of functioning of system of the electric drive in the set technological conditions of operation and to form requirements to development and adjustment of starting systems with the purpose of maintenance of power effective and reliable operation of system of asynchronous electric drives.* References 15, figures 5.

Key words: **induction motor, mathematical models, starting static characteristics, transients, saturation of the magnetic core, current displacement, compensation of reactive power.**

Розроблено методи і алгоритми числового аналізу пускових режимів асинхронного електроприводу, які дають змогу розраховувати статичні характеристики і перехідні процеси з урахуванням насичення магнітопроводу і явища скін-ефекту в стержнях ротора. Математичною основою розроблених алгоритмів є проекційний метод розв'язування нелінійних крайових задач, метод продовження по параметру, метод Ньютона розв'язування нелінійних систем рівнянь, числового інтегрування нелінійних систем диференціальних рівнянь. Розроблені математичні моделі дають змогу здійснювати з високою достовірністю розрахунок пускових режимів у трифазних і двофазних координатних осях, що дає змогу аналізувати не тільки симетричні, але й несиметричні режими і прогнозувати особливості функціонування системи асинхронного електроприводу в заданих технологічних умовах експлуатації. Бібл. 15, рис. 5.

Ключові слова: **асинхронний двигун, математичні моделі, пускові статичні характеристики, перехідні процеси, насичення магнітопроводу, витіснення струму, компенсація реактивної потужності.**

Разработаны методы и алгоритмы численного анализа пусковых режимов асинхронного электропривода, которые позволяют рассчитывать статические характеристики и переходные процессы с учетом насыщения магнитопровода и явления скин-эффекта в стержнях ротора. Математической основой разработанных алгоритмов является проекционный метод решения нелинейных краевых задач, метод продолжения по параметру, метод Ньютона решения нелинейных систем уравнений, численного интегрирования нелинейных систем дифференциальных уравнений. Разработанные математические модели позволяют осуществлять расчет пусковых режимов в трехфазных и двухфазных координатных осях, что позволяет анализировать не только симметричные, но и несимметричные режимы и прогнозировать особенности функционирования системы асинхронного электропривода в заданных технологических условиях эксплуатации. Библ. 15, рис. 5.

Ключевые слова: **асинхронный двигатель, математические модели, пусковые статические характеристики, переходные процессы, насыщение магнитопровода, вытеснение тока, компенсация реактивной мощности.**

Introduction. Three-phase induction motors (IMs) with a squirrel-cage rotor are the most common in modern electric drives. They are the main consumers of electricity in general and reactive power in particular. One of the problems of asynchronous electric drives is significant starting currents, which affect the quality of electrical energy of the network, which negatively affects other receivers. Despite the short duration of the start-up processes, frequent switching on of the IMs affects the reliability of their operation and reduces the service life. Direct connection of the IM to the network is accompanied not only by significant starting currents, but also by significant pulsations of the electromagnetic torque, and the shock torques affect the bearing assemblies and other elements of the electric drive. Finally, the starting currents of the IM cause electrical losses in the supply line, and if under the conditions of the electric drive operation the frequency of starts is significant, then, accordingly, the share of energy expended on starts is significant. This problem is especially relevant for electric drives with difficult starting conditions, including frequency-regulated ones.

Analysis of recent research. During start-up, the winding current of the stator of the IM can reach 5-7 times [1, 2], which is not always acceptable in specific operating conditions [3]. In addition, for some electric drives (ball mills, various crushers, etc.), which are started under load, it is necessary that the driving torque is several times higher than the critical one [4, 5], at which the starting current can exceed the nominal one several times. For long-term operation, this value of current is unacceptable, but it significantly reduces the start-up time [2], and thus reduces the operating time with such current. Prolonged starting of the electric drive with difficult starting conditions can lead to excess of admissible heating of a winding of a stator of the motor, especially in the conditions of frequent starts.

To form the necessary law of change of the electromagnetic torque of the IM in the course of start-up, starting control devices are used [6]. The task of developing an algorithm for the operation of starting equipment under conditions of providing the required driving torque with a minimum value of starting current [2] requires the definition of the laws of change of starting currents and electromagnetic torque.

The starting currents of the IM have a significant reactive component, which can be compensated by static capacitors [6-8]. In particular, to reduce the start-up time of high-power motors, capacitors connected in series to the stator winding can be used, which not only cause an increase in voltage on the motor, but can also cause resonance [9]. In connection with these problems, it is important to choose the starting control equipment, which should provide the necessary mechanical characteristics during the start-up process with the minimum possible power consumption [4, 5]. And since the control equipment and its maintenance requires additional material costs, it is necessary to find a compromise between saving electricity due to the economic flow of start-up processes and the cost of regulation. An overview of methods for improving the energy efficiency of asynchronous electric drives is given in [10].

To optimize the process of starting of the IM, taking into account the operating conditions of the electric drive, it is necessary to analyze it by methods of mathematical modelling. Therefore, the development of methods for calculating start-up processes is an urgent task.

IM is the main element of the electric drive, so the reliability of the calculation results depend on the level of adequacy of its mathematical model, and the speed of calculation codes – on the mathematical method and algorithm for its implementation. High accuracy of calculation of operating modes of the IM cannot be reached with use of their simple mathematical models, and use of a high level of complexity of models demands application of the difficult mathematical apparatus. The level of complexity of the mathematical model of the IM and the methods that must be used to calculate the modes and characteristics of its use are interrelated.

Most methods of calculating start-up modes, including those used in known computing environments, are based on the classic substituting circuits of the IM, which do not always meet the needs of practice. In order to increase the accuracy of calculations, in some works [4, 11] the authors divide the start-up process into separate parts. However, reliable information about the course of processes during start-up can be obtained only with the help of highly developed mathematical models of the IM, which adequately take into account all major factors, in particular, changes in inductive resistances due to saturation and in active resistances due to skin effect. In addition, the mathematical model of the electric drive system must take into account the law of change of the moment of resistance on the shaft of the IM during start-up [1]. Methods [2, 12, 13], which are based on a combination of field methods with circuit ones, allow to increase the accuracy of determining the electromagnetic torque, but due to their cumbersomeness they are not suitable for real-time control of the electric drive.

The goal of the paper is the development of mathematical models, methods and algorithms for calculating the starting modes of IMs.

Presentation of the main material. The equations of electrical equilibrium of the circuits of the IM, written for physical circuits, have the form

$$\frac{d\boldsymbol{\Psi}}{dt} + R\boldsymbol{i} = \boldsymbol{u}, \qquad (1)$$

where $\boldsymbol{\psi} = (\psi_1,\ldots,\psi_k)^*$, $\boldsymbol{i} = (i_1,\ldots,i_k)^*$ are the vectors of flux linkages and currents of k circuits (superscript (*) means transposition); R is the diagonal matrix of active resistances; $\boldsymbol{u}$ is the vector of applied voltages.

The mathematical model of the IM requires the calculation of flux linkages $\boldsymbol{\psi}$ and electromagnetic parameters $L = \partial\boldsymbol{\psi}/\partial\boldsymbol{i}$ according to the selected coordinate system. The flux linkage of each winding is a complex nonlinear function $\boldsymbol{\psi} = \boldsymbol{\psi}(i, \gamma)$ of the currents of all its circuits and the position of the rotor, which is determined by the angular coordinate γ of the rotor rotation. Therefore, differential equations (DEs), written for instantaneous values of physical coordinates, have periodic coefficients that complicate their solution. However, most practically important problems can be solved using transformed coordinate systems, which are based on the theory of image vectors [6, 14], the purpose of transition to which is to subtract the rotor rotation angle from the equations of electrical equilibrium of the circuits of the IM.

The question of choosing a coordinate system is of fundamental importance for the development of mathematical models of specific dynamic modes of electric drives. Both the volume of calculations and the accuracy of the calculation results depend on the chosen coordinate system. The developed methods the following are used:

a) a system of fixed three-phase axes that coincide with the physical axes of the stator phases;

b) a system of orthogonal axes x, y, 0, which rotate at any speed.

Magnetic cores of modern IMs have a high level of saturation, which causes nonlinearity of dependencies of flux linkages of circuits on currents, so mathematical models based on the assumption of their linearity do not provide the possibility of calculating dynamic modes with the required accuracy for modern engineering practice. Linearization of electromagnetic connections in the IM does not solve the problem, because in a real machine the saturation varies widely and is determined by the instantaneous values of the currents of all circuits. In the developed mathematical models for calculation of a matrix L of differential inductances of circuits of the IM, the basic characteristic of magnetization $\psi_\mu = \psi_\mu(i_\mu)$ is used as dependence of working flux linkage on magnetization current i_μ and dependencies of flux linkages of scattering of circuits of stator $\psi_{\sigma s} = \psi_{\sigma s}(i_s)$ and rotor $\psi_{\sigma r} = \psi_{\sigma r}(i_r)$ windings on the respective stator (s) and rotor (r) currents, which are calculated based on the geometric dimensions of the magnetic core and winding data.

In addition to saturation, the processes in the IM in dynamic modes are significantly affected by the phenomenon of current displacement in the rods of the squirrel-cage rotor, taking into account which in the starting modes is essential. Its consideration by artificial methods on the basis of the predicted distribution of penetration into the depth of the slot of the electromagnetic wave is probabilistic. Methods of taking into account the skin effect based on the calculation of the magnetic field in the slot of the machine [12, 13] are unacceptable due to their cumbersomeness. In the developed mathematical models, the rotor rods and short-circuiting rings are divided into n layers in height, which allows to solve the problem based on the theory of circuits [9]. As a result, we obtain n short-circuited windings on the rotor, between which there is a mutual inductive connection due to both the main magnetic flux and the scattering fluxes.

A mathematical model in fixed three-phase coordinates. Processes in the IM are described by a system of finite and differential equations compiled according to the Kirchhoff first and the second laws. To calculate the transients, it is expedient to replace the finite equations drawn up according to the Kirchhoff first law with differential ones. As a result, in a fixed three-phase coordinate system, electromagnetic processes are described by the DE system, which consists of three equations for the stator circuits

$$\begin{aligned}
&\frac{d\psi_A}{dt} - \frac{d\psi_B}{dt} = u_{AB} - r_A i_A + r_B i_B;\\
&\frac{d\psi_B}{dt} - \frac{d\psi_C}{dt} = u_{BC} - r_B i_B + r_C i_C;\\
&\frac{di_A}{dt} + \frac{di_B}{dt} + \frac{di_C}{dt} = 0,
\end{aligned} \tag{2a}$$

and $3n$ equations for n equivalent rotor windings

$$\begin{aligned}
&\frac{d\psi_{aj}}{dt} - \frac{d\psi_{bj}}{dt} = -r_{aj} i_{aj} + r_{bj} i_{bj} - \alpha\left(\psi_{bj} - 2\psi_{cj} + \psi_{aj}\right);\\
&\frac{d\psi_{bj}}{dt} - \frac{d\psi_{cj}}{dt} = -r_{bj} i_{bj} + r_{cj} i_{cj} - \alpha\left(\psi_{cj} - 2\psi_{aj} + \psi_{bj}\right);\\
&\frac{di_{aj}}{dt} + \frac{di_{bj}}{dt} + \frac{di_{cj}}{dt} = 0; \quad (j = 1,\ldots,n),
\end{aligned} \tag{2b}$$

where $\alpha = \omega_0(1-s)/\sqrt{3}$; s is the sliding; ω_0 is the motor supply voltage frequency; ψ_k, i_k, r_k, ($k = A, B, C, a_j, b_j, c_j$) are the phase flux linkages, currents and active resistances, respectively, $j = 1,\ldots,n$; u_{AB}, u_{BC} are the instantaneous values of line voltages.

The problem of starting the electric drive system requires a study of the process of breaking the IM taking into account the mechanical characteristics of the working mechanism [1, 5] in the form of the dependence of the instantaneous value of the load torque on the shaft $M_c = M_c(t)$ on time or angle of rotation of the rotor which may exceed its maximum passport value in operating mode [4, 5]. An important problem is the study of motor acceleration time to nominal speed [2], especially for electric drives with difficult starting conditions. Often speed is the main requirement for the operation of technological equipment. To form the necessary characteristics of the electric drive system, specially programmed starting systems are used [1, 6], which can be done using appropriate mathematical models.

To calculate the electromechanical process of starting the IM it is necessary to supplement the DE system (2) with the equation of mechanical equilibrium

$$\frac{d\omega}{dt} = \frac{p_0}{J}\left(M_e - M_c\right), \tag{3}$$

where ω is the angular speed of rotation of the rotor; p_0 is the number of pole pairs of the IM; J is the moment of inertia of the electric drive system reduced to the motor shaft.

The electromagnetic torque of the IM in the phase coordinates is determined by the formula

$$M_e = p_0\left(\psi_A\left(i_B - i_C\right) + \psi_B\left(i_C - i_A\right) + \psi_C\left(i_A - i_B\right)\right)/\sqrt{3},$$

where ψ_A, ψ_B, ψ_C, i_A, i_B, i_C are the projections of the image coupling vectors of the flux linkage $\boldsymbol{\psi}_\mu$ and the magnetization current $\boldsymbol{i}_\mu$ on the corresponding phase axes.

The DE system (2) together with equation (3) makes it possible to calculate the transient of starting the IM. To do this, it is necessary to integrate it numerically under zero initial conditions, calculating at each step of integration the matrix of differential inductivities and the vector of flux linkages [14].

Example of calculation of the start-up process of the IM 4A160M6Y3 (P_N = 15 kW, U_N = 380/220 V, s_N = 0.026; $k_{M\max}$ = 2.0; k_{M1} = 1.2; n_N = 1000 rpm; k_{I1} = 6; $\cos\varphi_N$ = 0.875) with a nominal load for different values of the moment of inertia of the electric drive system is shown in Fig. 1

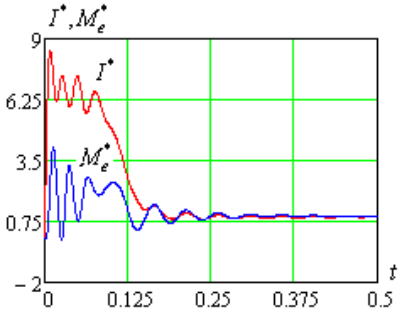

a

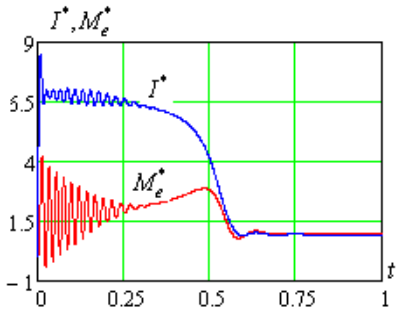

b

Fig. 1. Time dependencies of relative values of stator current (I^*) and electromagnetic torque (M_e^*) during start-up of the IM with nominal moment of loading and various moments of inertia: J – (*a*) and 5J – (*b*)

In order to present the projection method for calculating the steady state, we write system (2) in the form of a vector DE

$$\frac{d\boldsymbol{\psi}(\boldsymbol{i},t)}{dt} = z\left(\boldsymbol{\psi}(\boldsymbol{i},t), \boldsymbol{u}(t)\right), \qquad (4)$$

in which the periodic perturbation is the vector of applied voltages $u(t) = u(t + T)$.

In the steady state (at a constant sliding value s), the solution of the DE system (4) is the T-periodic time dependencies of the components of the vector $\boldsymbol{i}(t) = \boldsymbol{i}(t + T)$. The problem of their definition can be most effectively solved in the timeless domain by solving the boundary value problem using developed on the basis of the general theory of nonlinear oscillations the projection method, the theoretical basis of which is the approximation of state coordinates by splines. To do this, we approximate each coordinate of the vector $\boldsymbol{\psi}$ on the mesh of N nodes of the period by a third-order spline in accordance with what was stated in [15]. As a result, we obtain a continuous function, which is on every j-th time section $h = t_j – t_{j–1}$ (j = 1,...,N) is described by the equation of the form

$$\psi(t) = a_j + b_j\left(t_j - t\right) + c_j\left(t_j - t\right)^2 + d_j\left(t_j - t\right)^3,$$

spline coefficients, the ratio between which is determined by its properties. In particular,

$$\psi\left(t_j\right) = \psi_j = a_j, \quad d\psi/dt\,|_{t=t_j} = -b_j.$$

As a result, we obtain a system of discrete equations

$$H\boldsymbol{\Psi} - \boldsymbol{Z} = 0, \qquad (5)$$

in which H is the transition matrix from the continuous change of coordinates to their nodal values [15], the elements of which are determined only by the mesh of nodes in the period; $\boldsymbol{\Psi} = (\boldsymbol{\psi}_1, \ldots, \boldsymbol{\psi}_N)^*$; $\boldsymbol{Z} = (z_1, \ldots, z_N)^*$; $\boldsymbol{U} = (\boldsymbol{u}_1, \ldots, \boldsymbol{u}_N)^*$ are the column vectors, the components of which are the nodal values of the corresponding vectors of the system (4).

The system (5) of algebraic equations is a discrete analogue of the DE system (4). Its solution is a vector of nodal values of coordinates, the dependence of which on sliding s can be obtained by the differential method. To do this, we differentiate system (5) by s

$$W\frac{d\boldsymbol{\Psi}}{ds} = \frac{d\boldsymbol{Z}}{ds}, \qquad (6)$$

where W is the Jacobi matrix.

As a result of integrating the nonlinear DE system (6) by one of the numerical methods by s we obtain a multidimensional characteristic in the form of a set of periodic time dependencies of nodal coordinates for each sliding, using which we obtain the dependencies of flux linkages, electromagnetic torque and so on. An example of static characteristics calculations for the 4A160M6Y3 motor is shown in Fig. 2.

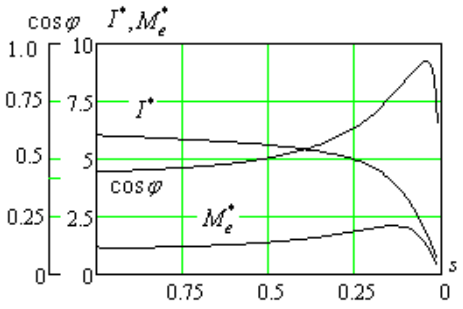

a

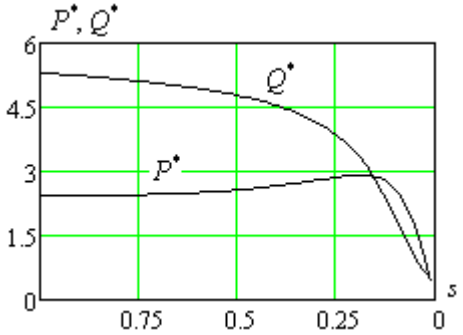

b

Fig. 2. Starting characteristics of the IM for current (I^*), electromagnetic torque (M_e^*) and cosφ (*a*), as well as active (P^*) and reactive (Q^*) powers (*b*) in relative units

Features of mathematical modelling of starting modes of the electric drive with individual compensation of reactive power. The so-called cosine capacitors can be connected in series or in parallel. For mathematical modelling of starting modes of the electric drive with longitudinal compensation it is necessary to replace the first two equations (2a) of the system in the initial DE system DR with those in which the presence of series-connected capacitors is taken into account:

$$\frac{d\psi_A}{dt} - \frac{d\psi_B}{dt} = u_{AB} - r_A i_A + r_B i_B - u_{kA} + u_{kB};$$

$$\frac{d\psi_B}{dt} - \frac{d\psi_C}{dt} = u_{BC} - r_B i_B + r_C i_C - u_{kB} + u_{kC},$$

where u_{kA}, u_{kB}, u_{kC} are the voltages on capacitors, and supplement it with equations

$$\frac{du_{kA}}{dt}=\frac{i_A}{C};\quad \frac{du_{kB}}{dt}=\frac{i_B}{C};\quad \frac{du_{kC}}{dt}=\frac{i_C}{C}.$$

In this case, the voltage drop across the phase capacitors affects the supply voltage of the motor, and therefore the electromagnetic torque, current and power can far exceed the nominal values. An example of the dependencies of the effective values of current, power and electromagnetic torque on the capacitance of series-connected capacitors, made on the basis of the calculation of currents and flux linkages of the circuits of the motor 4A160M6U3 at $s = 1$ is shown in Fig. 3.

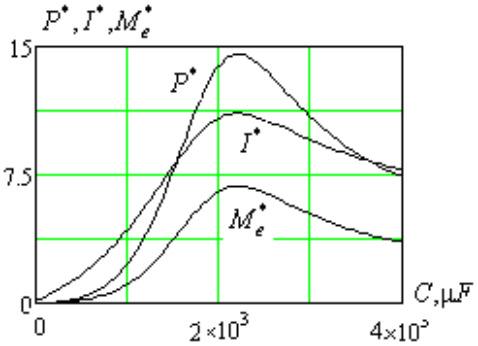

Fig. 3. Dependencies of relative values of current (I^*), active power (P^*) and electromagnetic torque (M_e^*) of the IM on the capacitance of series-connected capacitors

If the capacitors are connected in parallel to the IM, the mathematical model described by the system of equations (2) does not require changes, because the currents in them can be found separately, as the voltage on them is known. The currents in the supply line i'_A, i'_B, i'_C are defined as the sum of the currents of the motor i_A, i_B, i_C and parallel connected capacitors i_{Ak}, i_{Bk}, i_{Ck}. An example of the results of the calculation of the periodic dependences of the instantaneous values of the currents of phase A is shown in Fig. 4, and the dependencies of their effective values (in p.u.) and cosφ on the value of the capacitance of the capacitors – in Fig. 5.

The value of the capacitance selected by the static characteristic must be checked in the dynamic mode by calculating the transient because the capacitors connected in series can lead to the appearance of resonant phenomena [6, 9].

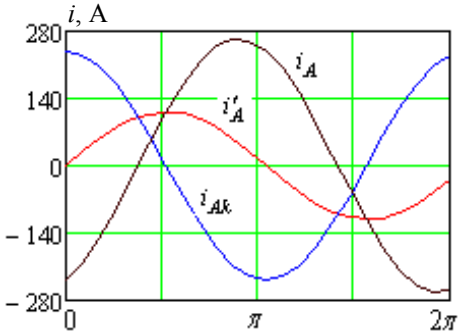

Fig. 4. Curves of currents of phase A: i'_A – supply line; i_{Ak} – capacitor; i_A – motor

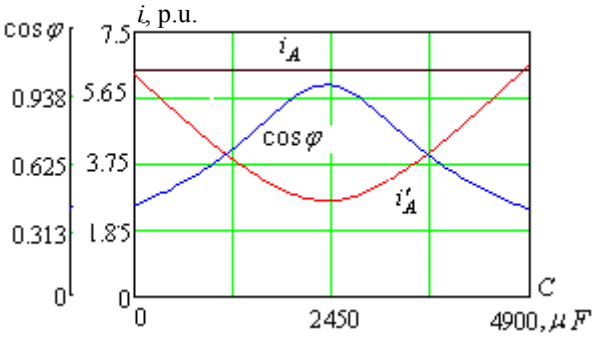

Fig. 5. Dependencies on the capacitance of the effective values of currents of phase A: i'_A – supply line; i_A – motor and of cosφ of the electric drive systems with capacitors connected in parallel

A mathematical model in orthogonal coordinates. In symmetrical modes of operation of the IM in the absence of higher harmonics in the supply voltages of the stator, the starting modes can be considered in orthogonal coordinates. The mathematical model of the electric drive system in the coordinate basis converted to orthogonal axes is much simpler than the model in three-phase axes, but its scope is narrowed.

Consider a mathematical model for studying the starting characteristics of the IM using a system of coordinate axes x, y. To do this, the three-phase stator winding and formed by the rotor rods n equivalent three-phase windings are reduced to the x, y axes. As a result, we will have two windings on the stator and $2n$ windings on the rotor. The DE system of electrical equilibrium of circuits has the form

$$\begin{aligned}
\frac{d\psi_{sx}}{dt}&=\omega_0\psi_{sy}-r_s i_{sx}+u_{sx};\\
\frac{d\psi_{sy}}{dt}&=-\omega_0\psi_{sx}-r_s i_{sy}+u_{sy};\\
\frac{d\psi_{1x}}{dt}&=s\omega_0\psi_{1y}-r_1 i_{1x};\\
\frac{d\psi_{1y}}{dt}&=-s\omega_0\psi_{1x}-r_1 i_{1y};\\
&\vdots\\
\frac{d\psi_{nx}}{dt}&=s\omega_0\psi_{ny}-r_n i_{nx};\\
\frac{d\psi_{ny}}{dt}&=-s\omega_0\psi_{nx}-r_n i_{ny},
\end{aligned}\qquad (7)$$

where ψ_{sx}, ψ_{sy}, ψ_{1x}, ψ_{1y}, ... , ψ_{nx}, ψ_{ny} are the flux linkages and i_{sx}, i_{sy}, i_{1x}, i_{1y}, ... , i_{nx}, i_{ny} are the currents of transformed circuits; r_s, r_1, ... , r_n are their active resistances.

The DE system (7) together with the equation of rotor motion

$$\frac{ds}{dt}=-\frac{p_0}{J\omega_0}\left(\frac{3}{2}p_0\left(\psi_{sx}i_{sy}-\psi_{sy}i_{sx}\right)-M_c\right)$$

allows to investigate the process of starting of the IM with or without load ($M_c = 0$) by solving the Cauchy problem in the time domain.

Under the condition of constant sliding, the DE system (7) is transformed into a system of ordinary nonlinear equations

$$
\begin{aligned}
-\omega_0\psi_{sy} + r_s i_{sx} &= U_m;\\
\omega_0\psi_{sx} + r_s i_{sy} &= 0;\\
-s\omega_0\psi_{1y} + r_1 i_{1x} &= 0;\\
s\omega_0\psi_{1x} + r_1 i_{1y} &= 0;\\
&\vdots\\
-s\omega_0\psi_{ny} + r_n i_{nx} &= 0;\\
s\omega_0\psi_{nx} + r_n i_{ny} &= 0.
\end{aligned} \tag{8}
$$

The multidimensional static characteristic as the dependence of the mode coordinates on the sliding can be calculated by solving the system of equations (8) for the sequence of sliding values s. One of the ways to determine the solution of system (8) at a given value of sliding s is the method of differentiation by parameter. To do this, write it in vector form

$$\boldsymbol{y}(\boldsymbol{\psi}, \boldsymbol{i}, s) = \boldsymbol{u}, \tag{9}$$

multiply the vector $\boldsymbol{u}$ by the scalar parameter ε ($0 \le \varepsilon \le 1$) and differentiate the obtained system by the parameter ε. As a result, we get the DE

$$A\frac{d\boldsymbol{i}}{d\varepsilon} = \boldsymbol{u}. \tag{10}$$

Integrating the vector DE (10) by ε (which can be done by the Euler method in a few steps), we obtain the value of the vector of currents $\boldsymbol{i}$, which is refined by the Newton iterative method. The initial conditions (the value of the vector $\boldsymbol{i}$) are zero, because for $\varepsilon = 0$ the vector of applied voltages is zero. The increment $\Delta\boldsymbol{i}^{(k)}$ of the current vector $\boldsymbol{i}$ at the k-th iteration step is determined by the formula

$$A\Delta\boldsymbol{i}^{(k)} = -\boldsymbol{Z}\left(\boldsymbol{i}^{(k)}\right), \tag{11}$$

where $\boldsymbol{Z}(\boldsymbol{i}^{(k)})$ is the residual vector of system (9) at given values of sliding s and the voltage vector $\boldsymbol{u}^{(k)}$.

In the case of series-connected capacitors, the first two equations of system (8) have the form

$$\omega_0\psi_{sy} - r_s i_{sx} + x_c i_{sy} = u_{sx};$$

$$-\omega_0\psi_{sx} - r_s i_{sy} - x_c i_{sx} = u_{sy},$$

where $x_c = 1/(\omega_0(1-s))$; $u_{sx} = U_m$; $u_{sy} = 0$.

Given a number of sliding values s of the rotor of the IM, we can get a multidimensional static characteristic in the form of the dependence of the coordinates on the sliding.

Conclusions and prospects for the development of the direction. One of the most important modes of asynchronous electric drive is the start-up process, so in the technical literature the problem of its analysis is given considerable attention. Various computer technologies are developed for the design of controlled asynchronous electric drives and their control systems, the basis of which are applied computer codes necessary for the analysis of electromechanical processes in electric drives. Not only quantitative but also qualitative indicators of the electric drive system, which must provide the necessary mechanical characteristics determined by the technological process and meet modern requirements for energy efficiency, depend on their adequacy. To solve these problems, the paper develops mathematical models that adequately reflect the electromagnetic processes in the IM and do not require significant computing resources. In particular, the design of the electric drive system requires the choice of its elements, including the starting control equipment, which can be done by calculating the static characteristics. With their help it is possible to determine the limit values of currents, torque, power, etc. in order to establish the functioning of the starting control equipment.

The developed calculation methods are based on the mathematical model of the IM, which takes into account both the change of natural and mutual differential inductive resistances of the motor due to saturation of the magnetic core and active resistances of squirrel-cage rotor winding due to current displacement in the rods. The mathematical model for the calculation of static characteristics in three-phase braked axes is based on solving the boundary value problem for DE of the first order with periodic boundary conditions and allows to perform optimization calculations with minimal computational costs. A feature of the model is the ability to investigate the processes at asymmetry of supply voltages, as well as at the presence of capacitors with longitudinal compensation of reactive power.

For symmetrical modes of operation the method of calculation of modes and characteristics in orthogonal coordinate axes x, y is developed which allows to carry out calculation with the minimum volume of calculations and accordingly expenses of computation time, and therefore to use the developed algorithm for control of the electric drive system in dynamic modes in real-time process. However, its use is limited to symmetrical modes of operation of the electric drive.

Peculiarities of using the developed mathematical models and algorithms for research of influence of capacitors on parameters of the electric drive at longitudinal and cross compensation of reactive power are presented.

Conflict of interest. The authors declare no conflict of interest.

REFERENCES

1. Chernyiy, A.P., Gladyir, A.I., Osadchuk, Yu.G., Kurbanov, I.R., Voshun, A.N. *Starting systems of unregulated electric drives.* Kremenchug: PF Shcherbatykh A.V., 2006, 280 p. (Rus).

2. Abhishek Garg, Arun Singh Tomar. Starting time calculation for induction motor. *International Journal of Engineering Research and Applications*, May 2015, vol. 5, iss. 5, pp. 56-60. Available at: http://www.ijera.com/papers/Vol5_issue5/Part%20-%203/J505035660.pdf (accessed 12.10.2020).

3. Hashimov A.M., Rahmanov R.N. Starting-Up Impact of Powerful Asynchronous Motors Used at Gas-Compressor Units on GRID Mode. *ENERGETIKA. Proceedings of CIS higher education institutions and power engineering associations*. 2012, no. 1, pp. 17-22. (Rus).

4. Belyaev V.P., Skakun V.V. Dynamics of processes of start-up of the asynchronous electric drive. *Proceedings of BSTU*, 2015, no. 9 (182), pp. 34-40. Available at: https://elib.belstu.by/bitstream/123456789/17345/1/dinamika-

processov-puska-asinxronnogo-ehlektroprivoda-dynamics-of-processes-of-start-up-of-the-asynchronous-electric-drive-v.-p.-belyaev-v.-v.-skakun-v.-p.-belyaev-v.-v.-skakun.pdf (accessed 12.10.2020). (Rus).

5. Khrebtova O. Forming the induction motor torque when starting. *Technical Electrodynamics*, 2020, no. 5, pp. 40-44. doi: https://doi.org/10.15407/techned2020.05.040.

6. Aflyatunov I.F. *Asinkhronnyi elektroprivod s kondensatornym pusko-reguliruiushchim ustroistvom: dis. kand. tekhn. nauk* [Asynchronous electric drive with capacitor start up regulator device. Cand. tech. sci. diss.]. Ulyanovsk, UlGTU Publ., 2016. 150 p. Available at: https://www.dissercat.com/content/asinkhronnyi-elektroprivod-s-kondensatornym-pusko-kompensiruyushchim-ustroistvom (accessed 12.10.2020). (Rus).

7. Vishnevskiy L.V., Muha N.I., Pavlenko S.S. *Pusk asinkhronnykh elektrodvigatelei s kompensatsiei reaktivnoi moshchnosti: monografiia* [Start of asynchronous motors with reactive power compensation]. Odessa, NU OMA Publ., 2016. 160 p. (Rus).

8. Gorbachevskiy N.I., Aflyatunov I.F. Investigation of starting an induction motor with capacitors in series in the stator circuit. *Bulletin of the Kazan Technological University*, 2013, vol. 16, no. 12, pp. 112-114. Available at: https://www.elibrary.ru/download/elibrary_19141286_43355538.pdf (accessed 12.10.2020). (Rus).

9. Malyar V., Hamola O., Maday V., Vasylchyshyn I. Mathematical modeling of processes in asynchronous motors with capacitors connected in series. *2015 16th International Conference on Computational Problems of Electrical Engineering (CPEE)*, Lviv, Ukraine, 2015, pp. 107-109. doi: https://doi.org/10.1109/cpee.2015.7333350.

10. Diachenko G.G., Aziukovskyi O.O. Review of methods for energy-efficiency improvement in induction machines. *Naukovyi Visnyk Natsionalnoho Hirnychoho Universytetu*, 2020, no. 1, pp. 80-88. doi: https://doi.org/10.33271/nvngu/2020-1/080.

11. Khrisanov V.I. Analysis of starting transients of squirrel-cage induction motor. The start-off stage. *Russian Electrical Engineering*, 2010, vol. 81, no. 3, pp. 109-114. doi: https://doi.org/10.3103/S1068371210030016.

12. Kocman S., Orsag P., Pecinka P. Simulation of Start-Up Behaviour of Induction Motor with Direct Online Connection. *Advances in Electrical and Electronic Engineering*, 2018, vol. 15, no. 5, pp. 754-762. doi: https://doi.org/10.15598/aeee.v15i5.2342.

13. Zamchalkin A.S., Tyukov V.A. Numerical modeling of process of start-up of the induction motor. *Proceedings of TUSUR University*, 2012, no. 1 (25), part 1, pp. 171-177. Available at: https://journal.tusur.ru/storage/45503/171.pdf?1466640193 (accessed 12.10.2020). (Rus).

14. Kulagin D.O. The mathematical model of asynchronous traction motor taking into account the saturation of magnetic circuits. *Naukovyi Visnyk Natsionalnoho Hirnychoho Universytetu*, 2014, no. 6, pp. 103-110. Available at: https://nvngu.in.ua/index.php/en/component/jdownloads/finish/50-06/1538-2014-6-kulagin/0 (accessed 12.10.2020). (Ukr).

15. Malyar V.S. Main provisions of the spline method for calculating the periodic operation modes of electric circuits. *Electronics and Communications*, 1998, no. 5, pp. 11-14. (Rus).

Received 12.11.2020
Accepted 01.02.2021
Published 05.04.2021

V.S. Malyar[1], *Doctor of Technical Science, Professor,*
O.Ye. Hamola[1], *PhD, Associate Professor,*
V.S. Maday[1], *PhD, Associate Professor,*
I.I. Vasylchyshyn[1], *PhD, Associate Professor,*
[1] Lviv Polytechnic National University,
12, S. Bandera Str., Lviv, 79013, Ukraine,
e-mail: vasyl.s.maliar@lpnu.ua, orest.y.hamola@lpnu.ua, volodymyr.s.madai@lpnu.ua

How to cite this article:
Malyar V.S., Hamola O.Ye., Maday V.S., Vasylchyshyn I.I. Mathematical modelling of starting modes of induction motors with squirrel-cage rotor. *Electrical Engineering & Electromechanics*, 2021, no. 2, pp. 9-15. **doi: 10.20998/2074-272X.2021.2.02.**

UDC 62.523:621.313.13 **doi: 10.20998/2074-272X.2021.2.03**

S.G. Buriakovskyi, A.S. Maslii, L.V. Asmolova, N.T. Goncharuk

MATHEMATICAL MODELLING OF TRANSIENTS IN THE ELECTRIC DRIVE OF THE TURNOUT OF THE MONO-SLEEPER TYPE WITH SWITCHED-INDUCTOR MOTOR

Introduction. *The study is devoted to the development of the functionality of a railway track switch by introducing a switched-inductor electric drive. This solution justifies simplifying the mechanical part of the switches by changing the gearbox to a ball-screw and locating the all kinematic line of the switches on the mono-sleeper type.* ***Goal.*** *A study of the mono-sleeper turnout type behaviour to meet modern traffic safety requirements and improve operational reliability factors.* ***Methodology.*** *Based on electric drive theory, a kinematic line of a mono-switch turnout type with nonlinear friction characteristic is presented. Using differential equation theory and Laplace transformation, a mathematic description of a four-phase switched-inductor motor with ball-screw in a mechanical line of a single-mass electromechanical system has been made. A simulation mathematical model of the electric drive of mono-sleeper turnout type as the control system with a switched-inductor motor and nonlinear friction characteristic was built in MATLAB.* ***Results.*** *Simulation modelling of a mathematical model of a mono-sleeper turnout type with a switched-inductor motor and ball-screw gear has been developed and implemented. Studies of dynamics of turnout point movement have shown that, in contrast to the motors used today, the switched-inductor motor makes it possible to simplify the mechanical part of the drive, which leads to reduced time spent on laying and maintenance of turnout points, and therefore makes the design more reliable. The application of PID controller and fuzzy speed controller has shown improved dynamics of turnout point, while the fuzzy PID controller provides better performance of the set values and turnout point movements.* ***Originality.*** *First developed a mathematical model of the electric drive of the mono-sleeper turnout type, taking into account nonlinear friction characteristic, as an object of speed control of turnout point movement, is developed.* ***Practical value.*** *The developed mathematical model of a railway track turnout of the mono-sleeper type with a switched-inductor motor and ball-screw gear enables more efficient use of a microprocessor control system, creation of promising electric motor protection means and control of a turnout point.* References 18, table 2, figure 14.

Key words: **switched-inductor electric drive, electromechanical system, control system, fuzzy speed controller**.

Робота присвячена розвитку функціональності залізничного стрілочного переводу шляхом впровадження вентильно-індукторного електроприводу. Таке рішення дає обгрунтування для спрощення механічної частини стрілочного переводу шляхом заміни редуктора на кульково-гвинтову пару, а також розмістити усю кінематичну лінію стрілочного переводу на одній шпалі. Наведено математичний опис чотирифазного вентильно-індукторного двигуна, та спрощеної механічної лінії стрілочного переводу у вигляді одномасової електромеханічної системи. Розроблена імітаційна математична модель електроприводу стрілочного переводу моношпального типу як система підлеглого керування з вентильно-індукторним двигуном, яка враховує нелінійну характеристику навантаження. Наведено результати комп'ютерного моделювання з ПІД та нечітким регулятором швидкості, які показали, що нечіткий ПІД регулятор більш якісно відпрацьовує задані величини та переміщення гостряків. Бібл. 18, табл. 2, рис. 14.

Ключові слова: **вентильно-індукторний електропривод, електромеханічна система, система керування, нечіткий регулятор швидкості.**

Работа посвящена развитию функциональности железнодорожного стрелочного перевода путем внедрения вентильно-индукторного электропривода. Такое решение дает обоснование для упрощения механической части стрелочного перевода путем замены редуктора на шарико-винтовую пару, а также разместить всю кинематическую линию стрелочного перевода на одной шпале. Приведено математическое описание четырехфазного вентильно-индукторного двигателя и упрощенной механической линии стрелочного перевода в виде одномассовой электромеханической системы. Разработанная имитационная математическая модель электропривода стрелочного перевода моношпального типа как система подчиненного управления с вентильно-индукторным двигателем учитывает нелинейную характеристику нагрузки. Приведенные результаты компьютерного моделирования с ПИД и нечетким регулятором скорости показали, что нечеткий ПИД регулятор более качественно отрабатывает заданные величины и перемещения остряков. Библ. 18 табл. 2, рис. 14.

Ключевые слова: **вентильно-индукторный электропривод, электромеханическая система, система управления, нечеткий регулятор скорости**.

Introduction. One of the main directions of implementation of the National Transport Strategy of Ukraine for the period up to 2030 [1] is the renewal of the transport sector of Ukraine and the gradual harmonization of existing Standards and policies in this area with existing ones in the European Union. Among the main goals and objectives for the development of the transport sector is the development of the railway transport sector, technical capacity of the railway, as there is a threat of failure to meet the needs of Ukraine's economy in transportation and the impossibility of passenger traffic.

Today, the technical resource of the railway is almost exhausted, about 11 thousand km of railway tracks (about 30 % of the total length) require overhaul and reconstruction, there is a low speed of trains, exacerbated by the wear of tracks that are in critical condition. The load intensity of Ukrainian railways (annual volume of traffic per 1 km) is 3-5 times higher than the corresponding rate of developed European countries [2].

That is why in the field of railway transport one of the priority areas of formation and implementation of state policy is the transfer of the industry to the European level, renewal and modernization of fixed assets; technical and technological modernization of railway

transport, increasing the level of safety of railway transportation, modernization of track facilities.

The implementation of these areas of technical and technological modernization of railway transport will help increase the level of safety and quality of railway transport, ensure the efficient operation and development of railway transport.

A special role is given to the quality of operation of turnouts. The search for ways to improve the performance of their operation concerns the modernization or replacement of the electric motor [3], the introduction of new types of sensors and mechanisms for locking the sharps [4].

In [5] the improvement of the dynamics of operation and the expansion of the functionality of railway automation were considered by means of adjustable electric drive on the example of the switch SP-6m based on a DC motor, because in Ukraine, unfortunately, drives of this type are still used.

The development of railway transport, increasing the mass of trains and increasing the speed of their movement have led to the need to use drives with AC motors [6]. Induction three-phase AC motors have a number of advantages over DC motors with serial excitation, namely the absence of such a complex and unreliable unit as a collector, which significantly reduces operating costs for maintenance and repair. At present, AC electric motors of the MCT type are used on the railway [7].

In [8] a mathematical model of the turnout SP-6m was developed, which is quite widely used in Ukraine, based on DC and AC motors.

Further modernization of domestic turnouts requires replacement of existing drive designs, which are already morally and technically obsolete. These systems have shown their efficiency in many years of practice, but today they can not meet the new requirements for high-speed rail transport. Therefore, the need to modernize switch systems is obvious and should be carried out by means of electric drive [9-11].

Along with the improvement of existing electric switches by replacing unreliable elements and electric motors, global companies are working to create new types [12]. Increasingly, turnouts are equipped with a modified drive system with microcontroller control.

The Bombardier Transportation [13] EBI Switch 2000 electric drive is a non-detachable built-in sleeper (Fig. 1) which is the best example of a sleeper drive to date.

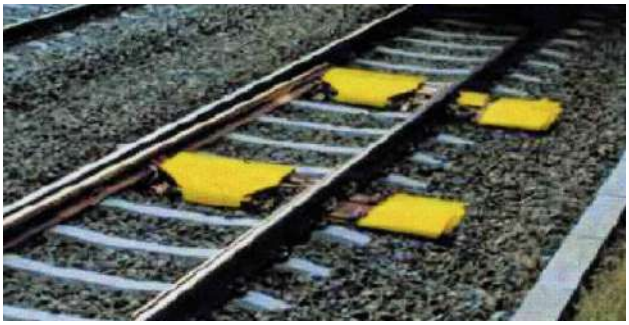

Fig. 1. General view of the EBI Switch 2000 turnout

A feature of EBI Switch 2000 is the presence in the design of a programmable frequency converter. Its application allows to carry out uniform start and braking of the motor, to control current and to stop the motor in case of impossibility of the fine-tuning of wits for a certain time of transfer. Figure 2 shows a diagram of the layout of the turnout EBI Switch 2000, where the following designations are accepted: 1 – electric motor; 2 – frequency converter; 3 – reducer; 4 – shaft with screw-nut transmission.

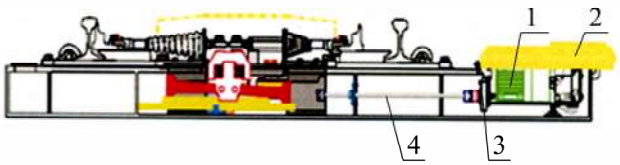

Fig. 2. The layout of the EBI Switch 2000 turnout

Any component of the EBI Switch 2000 system can be replaced in less than 15 minutes without removing the sleeper. The electric drive of this type does not require scheduled maintenance and repair. EBI Switch 2000 is tested in operation for about 10^6 cycles without failures. The average time to failure is 10-15 years.

Along with the development and implementation of microprocessor devices and the creation of modern low-maintenance equipment, creation of new types of switches that should ensure maximum reliability and safety of both normal and high-speed traffic and would reduce installation and maintenance time and costs due to abandonment of pre-assembly on an auxiliary platform is an important task.

The goal of the work is the study of the behaviour of the turnout operation of the mono-sleeper type to ensure modern requirements for traffic safety and improve operational reliability.

To achieve this goal the following tasks are formulated:

- to develop a mathematical model of a mono-sleeper switch with a switched-inductor motor and a ball-screw pair as a promising element of the automation system for express and high-speed electric railways;
- to develop a simulation model of a new switch design, which is obtained by replacing the old type of gearbox with a ball-screw pair, which allows to place the entire design of the switch in the sleeper and reduces the size and installation time;
- on the basis of the proportional-integral-differential (PID) speed regulator synthesized in [14], as well as the fuzzy regulator to investigate the dynamic processes in the turnout of the mono-sleeper type to improve its operation in both normal and transient modes.

Research material. For comparison, the electric drive of the switch type SP-6m (Fig. 3) is chosen, the kinematic scheme of which is given in [5], consisting of an electric motor (EM), a reducer with a built-in clutch of friction type and a gate located inside the housing.

Voltage is applied to the EM to switch turnout. Its shaft begins to rotate through the coupling of the gear shaft 2 of the gearbox, located in the housing 1 of the manual transmission (Fig. 4). The gear shaft with the gear 3 forms

the first transmission stage. The rotation from the gear 3 through the intermediate gear 6 is transmitted to the gear 12 (the second stage). Through the friction located in the housing 1, the rotation is transmitted to the third transmission stage – the gear shaft 11 and the gear 5 of the main shaft 10.

Fig. 3. External view of the SP-6m turnout

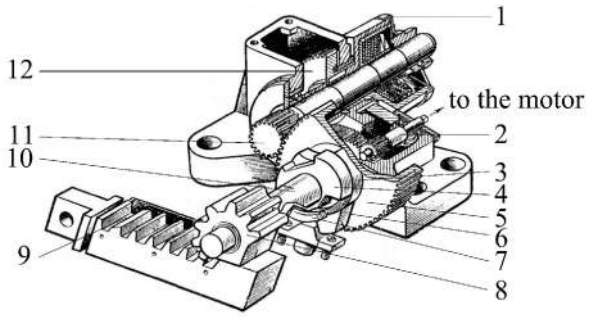

Fig. 4. Mechanical transmission of the SP-6m turnout

The sliding gear 8, which is made integral with the main shaft, moves the slide 9 (the fourth transmission stage). The gear 5 is freely mounted on the main shaft, the protrusion of which after turning at an angle of 46° comes into contact with the disk of the main shaft. Thus, the idling of the drive is 46°. The gear 5 has a trapezoidal protrusion to limit the rotation of the wheel. The presence of a technological gap of 46° is necessary to facilitate the acceleration of the motor and the supply of some kinetic energy in order to disrupt the sharps at the beginning of the transmission process.

Thus, the mechanical transmission allows to obtain the required speed of rotation of the main shaft and the torque of the required value and transmits the rotational motion of the armature to the working rail (gate), converting it into translational motion to transfer the arrowheads. But its design is quite complex, which reduces the overall reliability of the system.

To simplify the design of the turnout, the kinematic link was replaced by a «screw-nut» transmission, which converts the rotational movement of the screw into a translational movement of the nut. This transmission allows to significantly increase the transmission force without increasing the power of the motor [15]. Transmissions of this type have additional losses of friction, but this problem is solved by using a ball-screw pair «screw-nut» (Fig. 5), which has better performance and is used for more accurate movements of sharpeners than conventional screw one.

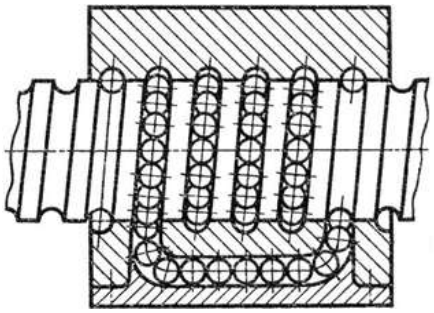

Fig. 5. Ball-screw pair «screw-nut»

The advantages of this pair are that it operates with low friction losses (due to rolling), high transmission efficiency, because the torque from the screw to the nut is transmitted through the balls in the nut. Rotation of the screw causes the nut with the balls to move in a horizontal plane. The nut is connected to the carriage, which in turn moves the slide through a mortise device, which is spring-loaded with a ball.

The modernization also consists in the fact that the authors of the paper propose to replace the DC or AC motor with a switched-inductor motor (SIM) [16, 17]. Because compared to an induction motor, the SIM has a higher starting torque, and with a DC motor – it does not require periodic maintenance and replacement of brushes in the collector-brush assembly, because it is absent. Thus, SIM has design and operational advantages that allow to predict that such machines will help not only to simplify the mechanical part of the drive and the control system of sharps, but also to increase its reliability and speed. In addition, they are the cheapest in production.

The functional diagram of SIM is shown in Fig. 6, which includes three units: an electromechanical power converter (EPF), an electronic switch (ES) and a control unit (CU) as part of the control module (CM) and a rotor position sensor (RPS) as part of the auxiliary equipment unit that controls by moving the sharpshooters. The control unit protects the motor from overloads (current, temperature ones) and controls the electronic switch.

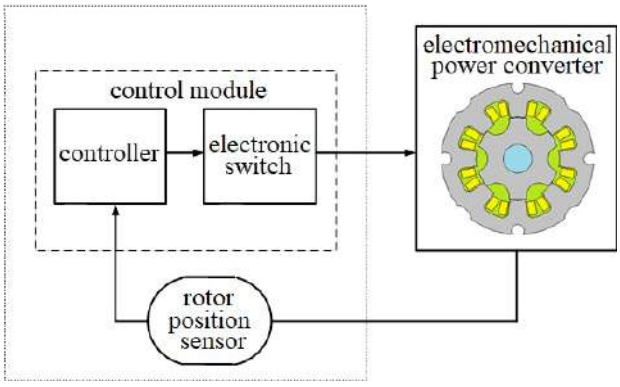

Fig. 6. Functional diagram of the electric drive with SIM

The 4-phase SIM with geometry 8/6 was chosen as a basis, its mathematical model is described by system of differential equations:

$$
\begin{cases}
\frac{di_A}{dt} = AA(i_A,i_B,i_C,i_D,\gamma)\cdot u_A + AB(i_A,i_B,i_C,i_D,\gamma)\cdot u_B + \\
+ AC(i_A,i_B,i_C,i_D,\gamma)\cdot u_C + AD(i_A,i_B,i_C,i_D,\gamma)\cdot u_D + \\
+ KA(i_A,i_B,i_C,i_D,\gamma)\cdot \omega + LAA(i_A,i_B,i_C,i_D,\gamma)\cdot i_A R_A + \\
+ LAB(i_A,i_B,i_C,i_D,\gamma)\cdot i_B R_B + LAC(i_A,i_B,i_C,i_D,\gamma)\cdot i_C R_C + \\
+ LAD(i_A,i_B,i_C,i_D,\gamma)\cdot i_D R_D; \\
\frac{di_B}{dt} = BA(i_A,i_B,i_C,i_D,\gamma)\cdot u_A + BB(i_A,i_B,i_C,i_D,\gamma)\cdot u_B + \\
+ BC(i_A,i_B,i_C,i_D,\gamma)\cdot u_C + BD(i_A,i_B,i_C,i_D,\gamma)\cdot u_D + \\
+ KB(i_A,i_B,i_C,i_D,\gamma)\cdot \omega + LBA(i_A,i_B,i_C,i_D,\gamma)\cdot i_A R_A + \\
+ LBB(i_A,i_B,i_C,i_D,\gamma)\cdot i_B R_B + LBC(i_A,i_B,i_C,i_D,\gamma)\cdot i_C R_C + \\
+ LBD(i_A,i_B,i_C,i_D,\gamma)\cdot i_D R_D; \\
\frac{di_C}{dt} = CA(i_A,i_B,i_C,i_D,\gamma)\cdot u_A + CB(i_A,i_B,i_C,i_D,\gamma)\cdot u_B + \\
+ CC(i_A,i_B,i_C,i_D,\gamma)\cdot u_C + CD(i_A,i_B,i_C,i_D,\gamma)\cdot u_D + \\
+ KC(i_A,i_B,i_C,i_D,\gamma)\cdot \omega + LCA(i_A,i_B,i_C,i_D,\gamma)\cdot i_A R_A + \\
+ LCB(i_A,i_B,i_C,i_D,\gamma)\cdot i_B R_B + LCC(i_A,i_B,i_C,i_D,\gamma)\cdot i_C R_C + \\
+ LCD(i_A,i_B,i_C,i_D,\gamma)\cdot i_D R_D; \\
\frac{di_D}{dt} = DA(i_A,i_B,i_C,i_D,\gamma)\cdot u_A + DB(i_A,i_B,i_C,i_D,\gamma)\cdot u_B + \\
+ DC(i_A,i_B,i_C,i_D,\gamma)\cdot u_C + DD(i_A,i_B,i_C,i_D,\gamma)\cdot u_D + \\
+ KD(i_A,i_B,i_C,i_D,\gamma)\cdot \omega + LDA(i_A,i_B,i_C,i_D,\gamma)\cdot i_A R_A + \\
+ LDB(i_A,i_B,i_C,i_D,\gamma)\cdot i_B R_B + LDC(i_A,i_B,i_C,i_D,\gamma)\cdot i_C R_C + \\
+ LDD(i_A,i_B,i_C,i_D,\gamma)\cdot i_D R_D; \\
M_{em} = FM(i_A,i_B,i_C,i_D,\gamma); \\
J\frac{d\omega}{dt} = M_{em} - M_l,
\end{cases}
$$

where i_A, i_B, i_C, i_D, γ are the currents of phases A, B, C, D respectively and the rotor rotation angle; u_A, u_B, u_C, u_D are the phase voltages; AA, AB, AC, AD, BA, BB, BC, BD, CA, CB, CC, CD, DA, DB, DC, DD are the phase voltage coefficients; KA, KB, KC, KD are the coefficients of angular speed of rotation; LAA, LAB, LAC, LAD, LBA, LBB, LBC, LBD, LCA, LCB, LCC, LCD, LDA, LDB, LDC, LDD are the phase current coefficients; R_A, R_B, R_C, R_D are the active resistances of the corresponding phases of the motor; FM is the motor torque coefficient; J is the moment of inertia of the rotor; ω is the angular speed of the motor; M_{em}, M_l are the electromagnetic moment of the motor and the static moment of loading, respectively.

All the considered coefficients are complex functions that depend on the phase currents and the angle of rotation of the motor rotor.

The use of a new type of electric motor in combination with a ball-screw pair allows to place the entire drive structure in a hollow sleeper, which reduces losses in the gearbox, reduces the size of the switch and simplifies the task of installation or replacement, as well as increases reliability and reduces operating costs. The design of such a turnout is shown in Fig. 7, where a SIM (1) with an electromechanical power converter (2), an electronic switch, which is part of the control module (3) and a rotor position sensor, which is located in the auxiliary equipment unit (4) are separated by a dotted line.

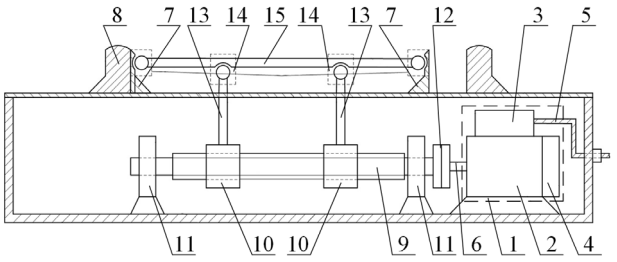

Fig. 7. Constructive scheme of turnout of mono-sleeper type

Depending on the signal of the rotor position sensor, the electronic switch connects the motor phase to the power supply via the cable (5). In this case, the electromechanical power converter (2) converts electrical energy into mechanical energy, driving the shaft of the machine (6). The ball-screw pair «screw-nut» converts the rotational movement of the screw (9) into the translational motion of the nuts (10). The screw is mounted on the support bearings (11) and connected to the motor shaft via a coupling (12). Nuts through vertical rods (13), hinges (14) and longitudinal rod (15) transmit forces to the sharpeners (7), which carry out their movement between the frame rail (8) [18].

To study the processes occurring in the mechanical part of the turnout of the mono-sleeper type, a mathematical simulation model (Fig. 8) was created according to the constructive scheme (Fig. 7), taking into account all the elements, parameters and connections between them.

In contrast to [8], where the kinematic line of the turnout was considered by two-mass and three-mass systems, the mechanical part of the turnout of the mono-sleeper type is considered as a single electromechanical system, i.e. a single-mass one (Fig. 9). This can be considered given that the force to the longitudinal thrust from the nuts is transmitted through two vertical thrusts (the force to the longitudinal thrust is applied at two points), as well as neglect the gaps in the joints, because they appear only in the process of their making.

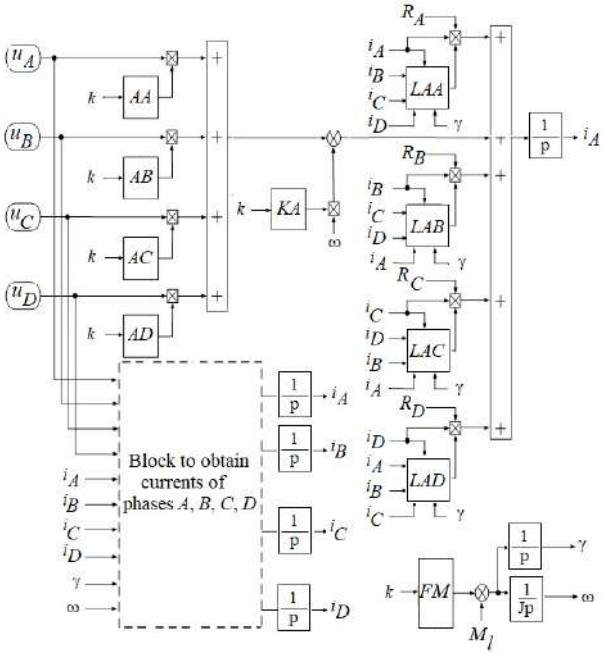

Fig. 8. Block diagram of the turnout of the mono-sleeper type

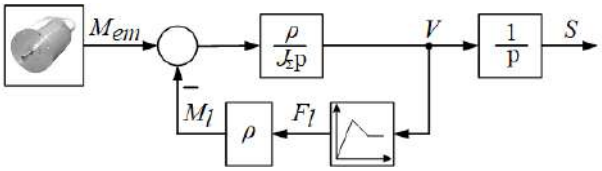

Fig. 9. Block diagram of the mechanical transmission of the turnout of the mono-sleeper type

Block diagram of Fig. 9 has a total reduced moment of inertia to the electric motor J_Σ, which consists of the moments of inertia of the SIM rotor, the transmission «screw-nut» and the masses of the sharps. In the feedback system there is a load unit $V = f(F_l)$, which reflects the characteristics of friction, because the switches operate in different weather conditions under the influence of random factors (fallen leaves, rain, snow, substances that fall out of cars, etc.). The average values of the coefficient of friction on the surface of the rail-cushion (steel-steel) are given in Table 1.

Table 1

Coefficient of friction at rest and sliding

Rubbing materials	Coefficient of friction			
	at rest		at sliding	
	without lubrication	with lubrication	without lubrication	with lubrication
rail-cushion	0,8	0,5-0,4	0,15-0,3	0,05-0,18

The control system of the turnout of the mono-sleeper type is considered as a system of subordinate control of coordinates with PID and fuzzy PID speed regulators, which together with SIM is reduced to the general simulation model in Fig. 10, and Fig. 11 shows a diagram of the mechanical part.

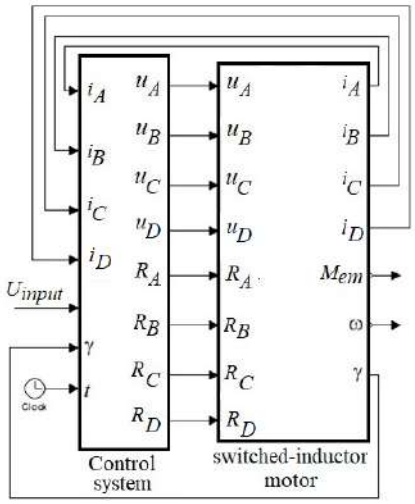

Fig. 10. Generalized SIM simulation model with control system

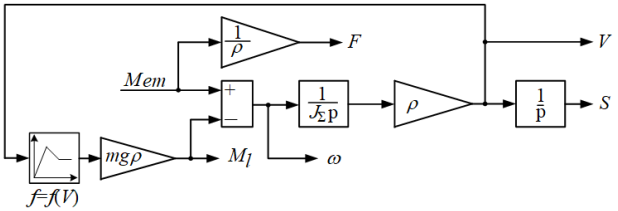

Fig. 11. Simulation model of the mechanical part of the turnout of the mono-sleeper type

The operation of the turnout of the mono-sleeper type was studied at a constant load, taking into account the friction characteristic, which most negatively affects the process of transfer of sharps. As a result of simulation of the kinematic line of the turnout, oscillograms of the distribution of traction force on the sharpeners $F = f(t)$, the speed of their transmission $V = f(t)$ and displacement $S = f(t)$, are obtained and shown in Fig. 12.

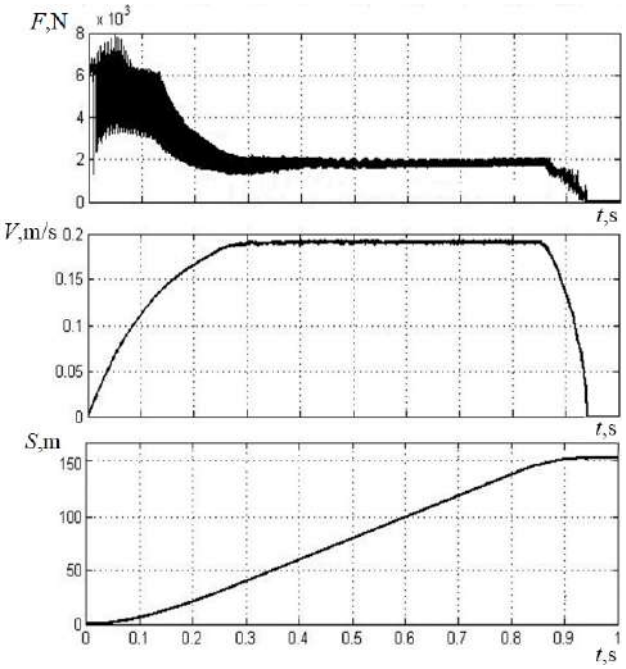

Fig. 12. Transients in mechanical transmission of mono-sleeper turnout

The obtained results show that in the kinematic line of the turnout there are fluctuations of the traction force, the amplitude of which in comparison with the traditional turnout has decreased by 5.5-6 times [8]. Such oscillations depend to a greater extent on the nature of the behaviour of the electromagnetic torque.

Figures 13, 14 show the transients of the electric drive operation, namely the electromagnetic torque and speed with PID speed controller (Fig. 13) and with fuzzy PID speed controller (Fig. 14) with additional constant load at $t = 0.6$ s.

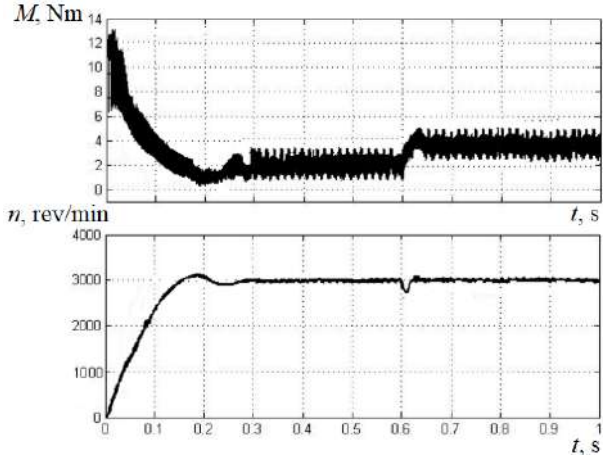

Fig. 13. Transients in turnout of mono-sleeper type with PID speed regulator

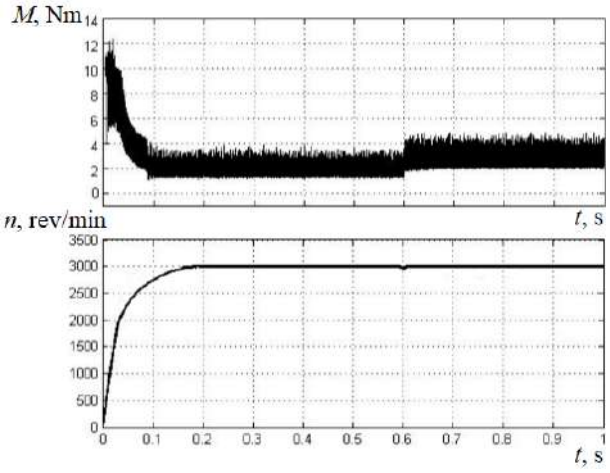

Fig. 14. Transients in the turnout of the mono-sleeper type with fuzzy PID speed controller

From the obtained graphs of transients it is established that the highest quality transient process corresponds to the system with fuzzy PID speed controller (Fig. 14), because the motor speed reaches a constant level without overregulation in contrast to the use of PID speed controller (Fig. 13). The main indicators of the quality of regulators are given in Table 2.

Table 2

Main indicators of the quality of regulatory processes

Quality indicator	PID regulator	Fuzzy PID regulator
Overregulation σ_{max}, %	4,2	0
Adjustment time t_s, s	0,27	0,17
Number of oscillations N	1	0

In addition, the proposed type of turnout works out a given movement of sharps for up to 1 s, which is crucial in terms of its use for high-speed rail transport.

Conclusions.

1. Using the developed mathematical model of mono-sleeper turnout with a switched-inductor motor and a ball-screw pair, a study of the dynamics of the movement of sharps in the MATLAB environment was performed. The results showed that the transition from the traditional turnout to the mono-sleeper type is justified. Unlike electric motors in use today, SIM has design advantages to simplify the mechanical part of the drive, as well as the control system of sharpeners. This has improved the quality of the dynamics of the turnout, which ensures the reliability and safety of both normal and high-speed rail transport.

2. Structural simplification of the kinematic transmission is performed by eliminating the intermediate gearbox in the existing EBI Switch 2000 turnout, which reduces the time spent on installation and maintenance of the switch, as well as makes the design more reliable.

3. The transition to a mono-sleeper turnout allows to more effectively apply the microprocessor control system, create promising means of electric motor protection and ensure control of the position of the sharps.

4. The use of PID and fuzzy PID speed regulators in the control system, taking into account the nonlinear characteristic of friction, showed an improvement in the dynamics of the turnout. In a system with a fuzzy PID controller, not only the transmission speed has increased, but there is also a better process of operation of a mono-sleeper type turnout with SIM.

Conflict of interest. The authors declare no conflict of interest.

REFERENCES

1. *Pro skhvalennia Natsionalnoi transportnoi stratehii Ukrainy na period do 2030 roku: rozporiadzhennia Kabinetu Ministriv Ukrainy vid 30 travnia 2018 r. № 430-r* [On approval of the National Transport Strategy of Ukraine for the period up to 2030. Order of the Cabinet of Ministers of Ukraine of May 30, 2018 № 430-r]. Available at: https://zakon.rada.gov.ua/go/430-2018-%D1%80 (Accessed 20.10.2020). (Ukr).

2. *Ministerstvo infrastruktury Ukrainy. Informatsiia pro ukrainski zaliznytsi* [Ministry of Infrastructure of Ukraine. General information about railway transport]. Available at: https://mtu.gov.ua/en/content/informaciya-pro-ukrainski-zaliznici.html (Accessed 20.10.2020). (Ukr).

3. Kande M., Isaksson A., Thottappillil R., Taylor N. Rotating Electrical Machine Condition Monitoring Automation – A Review. *Machines*, Oct. 2017, vol. 5, no. 4, p. 24. doi: https://doi.org/10.3390/machines5040024.

4. Bemment S.D., Goodall R.M., Dixon R., Ward C.P. Improving the reliability and availability of railway track switching by analysing historical failure data and introducing functionally redundant subsystems. *Proceedings of the Institution of Mechanical Engineers, Part F: Journal of Rail and Rapid Transit*, Sep. 2017, vol. 232, no. 5, pp. 1407-1424. doi: https://doi.org/10.1177/0954409717727879.

5. Buriakovskyi S., Smirnov V., Asmolova L., Obruch I., Rafalskyi O., Maslii A. Analysis of optimization criteria for the process of switch displacement in a DC railroad turnout. *Eastern-European Journal of Enterprise Technologies*, Dec. 2019, vol. 6, no. 2 (102), pp. 58-69. doi: https://doi.org/10.15587/1729-4061.2019.187580.

6. Fathy Abouzeid A., Guerrero J.M., Endemaño A., Muniategui I., Ortega D., Larrazabal I., Briz F. Control strategies for induction motors in railway traction applications. *Energies*, Feb. 2020, vol. 13, no. 3, p. 700. doi: https://doi.org/10.3390/en13030700.

7. Dorohin B.P., Serdyuk T.M. Implementation of new types of points motors. *Electromagnetic compatibility and safety on railway transport*, 2013, no. 6, pp. 71-84. Available at: http://ecsrt.diit.edu.ua/article/view/51291 (Accessed 20.10.2020). (Rus).

8. Buriakovskyi S.G., Maslii A.S., Pasko O.V., Smirnov V.V. Mathematical modelling of transients in the electric drive of the switch – the main executive element of railway automation. *Electrical Engineering & Electromechanics*, 2020, no. 4, pp. 17-23. doi: https://doi.org/10.20998/2074-272X.2020.4.03.

9. Lagos R.F., San Emeterio A., Vinolas J., Alonso A., Aizpun M. The influence of track elasticity when travelling on a railway turnout. *Proceedings of the Second International Conference on Railway Technology: Research, Development and Maintenance*, 2014, p. 11. doi: https://doi.org/10.4203/ccp.104.208.

10. Kuznetsov B.I., Nikitina T.B., Kolomiets V.V., Bovdui I.V. Improving of electromechanical servo systems accuracy. *Electrical Engineering & Electromechanics*, 2018, no. 6, pp. 33-37. doi: https://doi.org/10.20998/2074-272X.2018.6.04.

11. Moiseenko V.I., Poddubnyak V.I. *Avtomatika i komp'iuternye sistemy na stantsiiakh* [Automation and computer systems in stations]. Kiev, Transport of Ukraine Publ., 1999. 142 p. (Rus).

12. Arslan B., Tiryaki H. Prediction of railway switch point failures by artificial intelligence methods. *Turkish journal of electrical engineering & computer sciences*, Mar. 2020, vol. 28, no. 2, pp. 1044-1058. doi: https://doi.org/10.3906/elk-1906-66.

13. Sokol Y.I., Buryakovskiy S.G., Masliy Ar.S. Energy-efficient electric drive of multifunctional turnout. *Problemy Kolejnictwa*, 2014, no. 165, pp. 99-107. Available at: http://atena.ikolej.pl/images/PDF/165_8.pdf (Accessed 20.10.2020).

14. Buriakovskyi S., Maslii A., Pasko O., Denys I. Research and development of an electric traction drive based on a switched

reluctance motor. *Transport Problems*, 2018, vol. 13, no. 2, pp. 69-79. doi: https://doi.org/10.20858/tp.2018.13.2.7.
15. Li F., Jiang Y., Li T., Du Y. An improved dynamic model of preloaded ball screw drives considering torque transmission and its application to frequency analysis. *Advances in Mechanical Engineering*, 2017, vol. 9, no. 7, p. 168781401771058. doi: https://doi.org/10.1177/1687814017710580.
16. Buriakovskyi S., Babaiev M., Liubarskyi B., Maslii A., Karpenko N., Pomazan D., Maslii A., Denys I. Quality assessment of control over the traction valve-inductor drive of a hybrid diesel locomotive. *Eastern-European Journal of Enterprise Technologies*, 2018, vol. 1, no. 2 (91), pp. 68-75. doi: https://doi.org/10.15587/1729-4061.2018.122422.
17. Sezen S., Karakas E., Yilmaz K., Ayaz M. Finite element modeling and control of a high-power SRM for hybrid electric vehicle. *Simulation Modelling Practice and Theory*, Mar. 2016, vol. 62, pp. 49-67. doi: https://doi.org/10.1016/j.simpat.2016.01.006.
18. Buriakovskyi S.H., Maslii Ar.S., Maslii An.S. *Elektropryvid strilochnoho perevodu* [Electric switch point drive]. Patent UA, no. 95497, 2014. (Ukr).

Received 20.01.2021
Accepted 22.02.2021
Published 05.04.2021

S.G. Buriakovskyi [1], *Doctor of Technical Science, Professor,*
A.S. Maslii [2], *PhD, Associate Professor,*
L.V. Asmolova [3], *PhD,*
N.T. Goncharuk [4], *Doctor of Science in Public Administration, Professor,*
[1] Research and Design Institute «Molniya»
of National Technical University
«Kharkiv Polytechnic Institute»,
47, Shevchenko Str., Kharkiv, 61013, Ukraine,
e-mail: sergbyr@i.ua
[2] Ukrainian State University of Railway Transport,
7, Feierbakh Square, Kharkiv, 61050, Ukraine,
e-mail: a.masliy@ukr.net
[3] National Technical University «Kharkiv Polytechnic Institute»,
2, Kyrpychova Str., Kharkiv, 61002, Ukraine,
e-mail: asmolova_larisa@ukr.net
[4] Dnipropetrovsk Regional Institute for Public Administration,
National Academy for Public Administration
under the President of Ukraine,
29, Gogol Str., Dnipro, 49044, Ukraine,
e-mail: goncharuknt@gmail.com

How to cite this article:
Buriakovskyi S.G., Maslii A.S., Asmolova L.V., Goncharuk N.T. Mathematical modelling of transients in the electric drive of the turnout of the mono-sleeper type with switched-inductor motor. *Electrical Engineering & Electromechanics*, 2021, no. 2, pp. 16-22. **doi: 10.20998/2074-272X.2021.2.03.**

UDC 621.3.013 **doi: 10.20998/2074-272X.2021.2.04**

B.I. Kuznetsov, T.B. Nikitina, I.V. Bovdui, V.V. Kolomiets, B.B. Kobylianskiy

OVERHEAD POWER LINES MAGNETIC FIELD REDUCING IN MULTI-STORY BUILDING BY ACTIVE SHIELDING MEANS

Aim. *Reducing of magnetic flux density of magnetic field in multi-storey building, generated by overhead power lines to the sanitary standards level by active shielding means. The tasks of the work are the synthesis, Computer simulation and experimental research of three-circuits system of active shielding, which includes three shielding coils.* ***Methodology***. *When synthesizing the system of active shielding of magnetic field, are determined their number, configuration, spatial arrangement and of shielding coils as well as the shielding coils currents and resulting magnetic flux density value in the shielding space. The synthesis is based on the multi-criteria game decision, in which the payoff vector is calculated on the basis on quasi-stationary approximation solutions of the Maxwell equations. The game decision is based on the stochastic particles multiswarm optimization algorithms.* ***Results***. *Computer simulation and experimental research of three-circuit system of active shielding of magnetic field, generated by overhead power lines with phase conductors triangle arrangements in multi-storey building are given. The possibility of initial magnetic flux density level reducing in multi-storey building to the sanitary standards level is shown.* ***Originality***. *For the first time to reducing of magnetic flux density of magnetic field in multi-storey building the synthesis, Computer simulation and experimental research of three-circuit system of active shielding of magnetic field generated by single-circuit overhead power line with phase conductors triangular arrangements carried out.* ***Practical value***. *Practical recommendations from the point of view of the practical implementation on reasonable choice of the spatial arrangement of three shielding coils of three-circuit system of active shielding of the magnetic field generated by single-circuit overhead power line with phase conductors triangular arrangements in multi-storey building are given.* References 41, figures 15.

Key words: **overhead power lines with phase conductors triangle arrangements, magnetic field, system of active shielding, Computer simulation, experimental research.**

Цель. *Снижение уровня индукции магнитного поля внутри многоэтажного дома, генерируемого одноцепной воздушной линией электропередачи до уровня санитарных норм. Задачами работы являются синтез, компьютерное моделирование и экспериментальные исследования трехконтурной системы активного экранирования, содержащей три экранирующие обмотки.* ***Методология***. *При синтезе системы определены – количество, конфигурация, пространственное расположение экранирующих обмоток, а также токи в экранирующих обмотках и результирующие значения индукции магнитного поля в пространстве экранирования. Синтез трехконтурной системы активного экранирования основан на решении многокритериальной стохастической игры, в которой векторный выигрыш вычисляется на основании решений уравнений Максвелла в квазистационарном приближении. Решение игры находится на основе алгоритмов стохастической мультиагентной оптимизации мультироем частиц.* ***Результаты***. *Приводятся результаты компьютерного моделирования и экспериментальных исследований трехконтурной системы активного экранирования магнитного поля внутри многоэтажного дома, генерируемого воздушной линией электропередачи. Показана возможность снижения уровня индукции исходного магнитного поля внутри многоэтажного дома до уровня санитарных норм.* ***Оригинальность***. *Впервые для снижения уровня индукции магнитного поля внутри многоэтажного дома до уровня санитарных норм, проведены синтез, компьютерное моделирование и экспериментальные исследования трехконтурной системы активного экранирования магнитного поля, генерируемого одноцепной воздушной линией электропередачи с треугольным подвесом проводов.* ***Практическая ценность***. *Приводятся практические рекомендации по обоснованному выбору, с точки зрения практической реализации, пространственного расположения трех экранирующих обмоток трехконтурной системы активного экранирования магнитного поля, от генерируемого внутри многоэтажного дома магнитного поля одноконтурной воздушной линии электропередачи с треугольным подвесом проводов.* Библ. 41, рис. 15.

Key words: **воздушные линии электропередачи с треугольным расположением фазных проводов, магнитное поле, система активного экранирования, компьютерное моделирование, экспериментальное исследование.**

Introduction. Overhead power lines often run near residential buildings. These lines generate a power frequency magnetic field (MF) in residential buildings, the level of which often exceeds sanitary standards [1, 2]. To normalize the level of the magnetic field, it is most effective and economically feasible to use active screening methods [3, 4]. In an active shielding system (SAS), a compensating magnetic field is generated using shielding coils [5-18].

The number, spatial arrangement of shielding windings and their ampere turns are determined by the type of power transmission line and currents in the conductors of power transmission lines, as well as the spatial location of the shielding zone and its size, as well as the level of induction, which must be provided by means of active shielding. The simplest system is the single-circuit system, which contains only one – single shielding coil. With the help of such a system, it is possible to effectively screen a weakly polarized magnetic field, in which the space-time characteristic has the form of a highly elongated ellipse, which approaches a straight line.

However, the greatest difficulty for active shielding is a highly polarized magnetic field. The shape of the space-time characteristic of such a magnetic field approaches a circle. In particular, such a magnetic field is generated by a single-circuit power line with a triangle-shaped arrangement of wires. Active shielding of such a magnetic field requires at least two shielding coils.

In Ukraine, in the zones of old buildings, there are mainly five-storey residential buildings. In this case,

single-circuit 110 kV power lines with wires in the shape of a triangle pass most often near these residential buildings.

Most of the research focuses on reducing the magnetic field in one-story houses or even in a separate room at home [5-19]. Therefore, an urgent task is to reduce the magnetic field in the entire multi-storey building.

The aim of the work is reduce the level of magnetic flux density of the magnetic field in multi-storey building generated by single-circuit overhead power line by active shielding means. The tasks of the work are the synthesis, Computer simulation and experimental research of three-circuits system of active shielding.

Statement of the research problem. Let us consider the synthesis of system of active shielding of a magnetic field in a multi-story building. The magnetic field in a multi-story building is generated by a single-circuit overhead power transmission line with a spatial arrangement of wires in the shape of a triangle. In Fig. 1 are shown the layout of an overhead transmission line, a multi-story building, in which it is necessary to reduce the level of the initial magnetic field to sanitary standards of Ukraine.

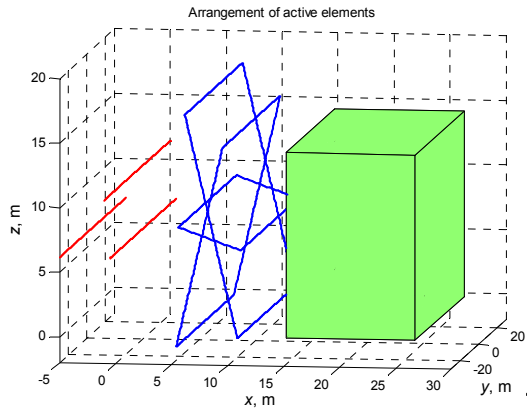

Fig. 1. The location of 110 kV overhead power line, three shielding coils and shielding space in multi-story building

Let us introducing the vector of unknown parameters the components of which are the number and coordinates of shielding coils as well as parameters of the regulator [19-23] and vector of uncertainty parameters [24-28]. Then the calculate of vector of unknown parameters of system of active shielding and of vector of uncertainty parameters in the form of a solution of multi-criteria game. The components vector payoff in this game is levels of magnetic flux density at points of the shielding space. These components are nonlinear functions of the vectors of unknown parameters and uncertainty parameters and are calculated on basis of Maxwell equations quasi-stationary approximation solutions [3]. First player is vector of unknown parameters and its strategy is minimization of vector payoff. Second player is vector of uncertainty parameters and this strategy is maximization of the same vector payoff [29].

Therefore, the solution of multi-criteria game is calculated from the condition of minimum value of vector payoff for the vector of unknown parameters but the maximum value of vector payoff for the vector uncertainty parameters. This technique corresponds to the standard worst-case robust systems synthesis approach [27, 28].

To find multi-criterion game solution from Pareto-optimal set solutions taking into account binary preference relations [29-32] used particle multiswarm optimization algorithm [33-41], in which swarms number equal number of vector payoff components.

Computer simulation results. Consider the result of synthesis of SAS of MF with circular space-time characteristic created by three-phase single-circuit overhead power line 110 kV with phase conductors triangular arrangements in a multi-story building, as it is shown in Fig. 1. In order to reduce the level of magnetic flux density of the initial magnetic field throughout the entire multi-story building to the level of sanitary standards of Ukraine, in this case, it is necessary to use three shielding windings, as it is shown in Fig. 1.

In Fig. 2 are shown lines of equal level of module of the resultant magnetic flux density with the system of active shielding is on. As follows from this figure, the level of magnetic flux density of the resulting magnetic field in the entire space of a multi-storey building does not exceed the level of 0.5 μT, which corresponds to the sanitary standards of Ukraine. Note that in the center of the multi-storey building under consideration, the level of magnetic flux density of the resulting magnetic field does not exceed 0.2 μT. Therefore, in this part of the space, using an system of active shielding, the induction level of magnetic flux density of the initial magnetic field can be reduced by more than 20 times.

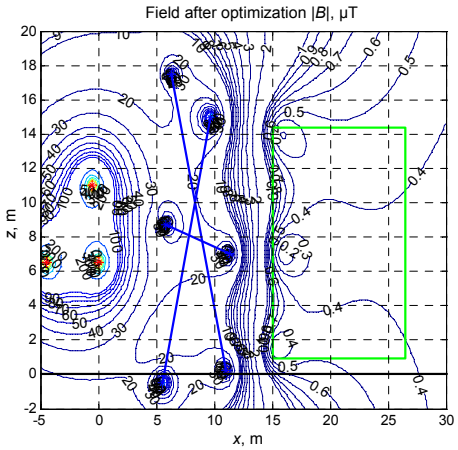

Fig. 2. Isolines of the resultant magnetic flux density with the system of active shielding is on

In Fig. 3 are shown the space-time characteristics of the magnetic flux density vector of magnetic field generated by: 1) overhead power line; 2) all three shielding coils and 3) the resultant magnetic field with the system of active shielding.

In Fig. 4 are shown the dependences of the of levels of the magnetic flux density of the initial magnetic field and the resultant magnetic field when the system of active shielding is on as a function of the distance from the extreme conductor of the power line. As can be seen from this figure, the system of active shielding is reduced the level of the magnetic flux density of the initial magnetic field by more 10 times from 4.25 μT to 0.4 μT and therefore the shielding factor is more 10.

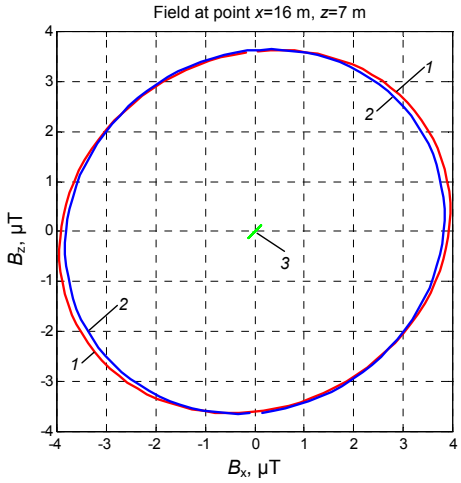

Fig. 3. Comparison between space-time characteristics of magnetic flux density without and with system of active shielding with all three shielding coils and only all three shielding coils

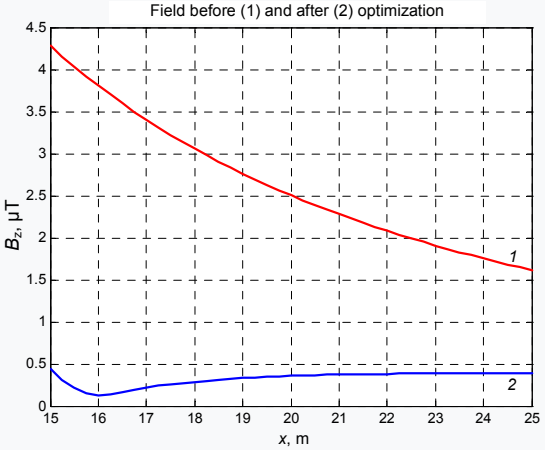

Fig. 4. Comparison of magnetic flux density level between with and without system of active shielding

Now let us consider the shielding efficiency of the original magnetic field when only one single firs shielding coil is used at optimal values of the regulator of this coil.

In Fig. 5 are shown the space-time characteristics of the magnetic flux density vector of magnetic field generated by: 1) overhead power line; 2) only one single firs shielding coils and 3) the resultant magnetic field with the only one single firs shielding coils.

In Fig. 6 are shown the dependences of the of levels of the magnetic flux density of the initial magnetic field and the resultant magnetic field when the only single first shielding coil of system of active shielding is on as a function of the distance from the extreme conductor of the power line.

As can be seen from this figure, with only one single first shielding coil of the active shielding system, the level of magnetic flux density of the initial magnetic field is increased in 1.19 times in the considered space from 4.25 μT to the level of 5 μT due to overcompensation.

Now let us consider the shielding efficiency of the original magnetic field when only one single second shielding coil is used at optimal values of the regulator of this coil. In Fig. 7 are shown the space-time characteristics of the magnetic flux density vector of magnetic field generated by: 1) overhead power line; 2) only one single second shielding coils and 3) the resultant magnetic field with the only one single second shielding coils.

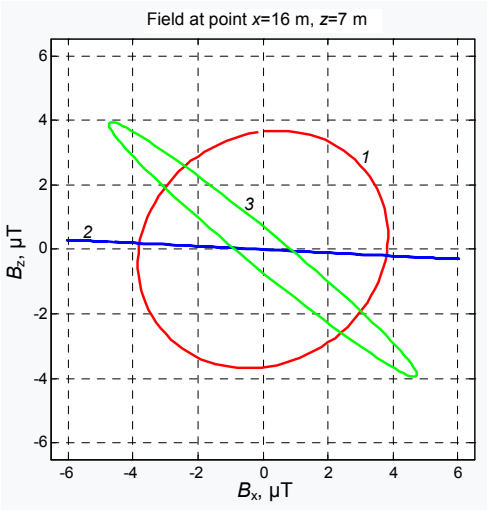

Fig. 5. Comparison between space-time characteristics of magnetic flux density without and with system of active shielding with only single first shielding coil

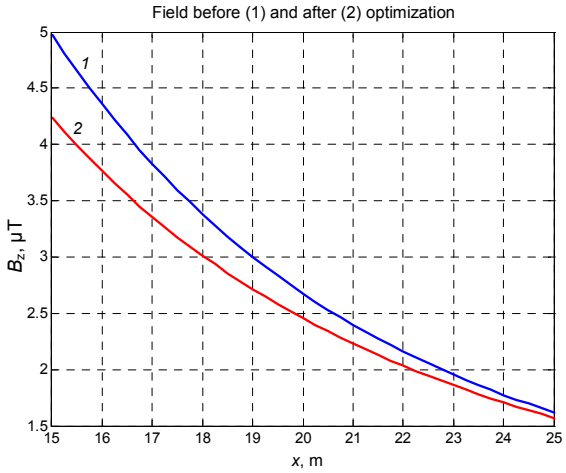

Fig. 6. Comparison of magnetic flux density between with and without system of active shielding with only single first shielding coil

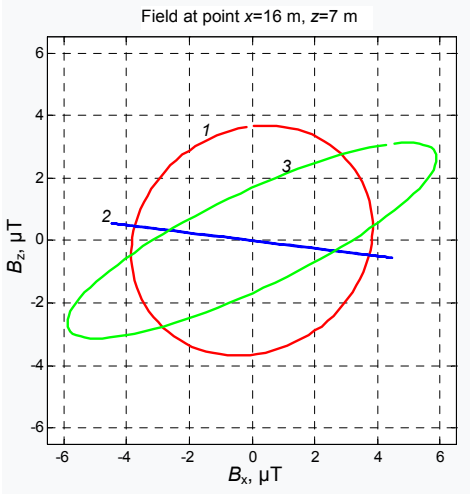

Fig. 7. Comparison between space-time characteristics of magnetic flux density without and with system of active shielding with only single second shielding coil and only single second shielding coil

In Fig. 8 are shown the dependences of the of levels of the magnetic flux density of the initial magnetic field and the resultant magnetic field when the only single second shielding coil of system of active shielding is on as a function of the distance from the extreme conductor of the power line. As can be seen from this figure, with only one single second shielding coil of the active shielding system, the level of magnetic flux density of the initial magnetic field is increased in 1.28 times in the considered space from 4.25 μT to the level of 5.4 μT due to overcompensation.

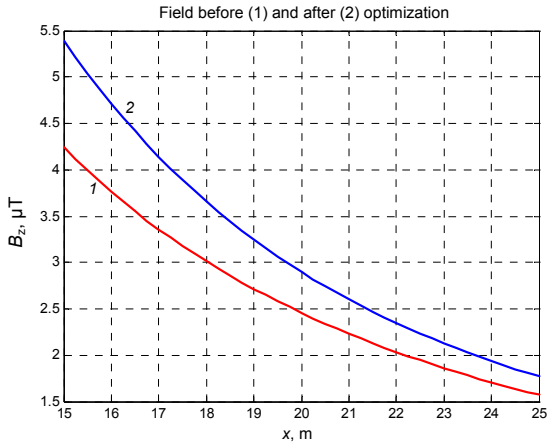

Fig. 8. Comparison of magnetic flux density between with and without system of active shielding with only single second shielding coil

Now let us consider the shielding efficiency of the original magnetic field when only one single third shielding coil is used at optimal values of the regulator of this coil. In Fig. 9 are shown the space-time characteristics of the magnetic flux density vector of magnetic field generated by: 1) overhead power line; 2) only one single third shielding coils and 3) the resultant magnetic field with the only one single third shielding coils.

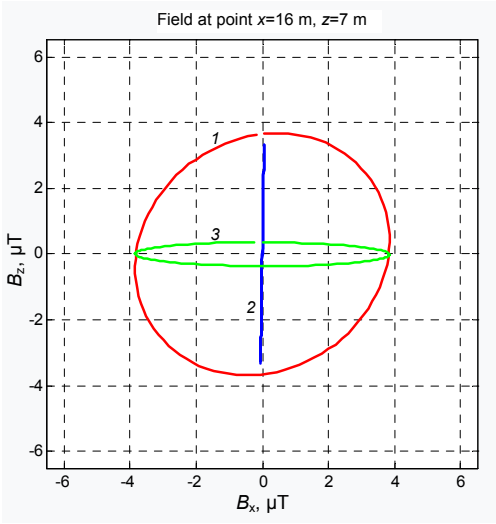

Fig. 9. Comparison between space-time characteristics of magnetic flux density without and with system of active shielding with only single third shielding coil and only single third shielding coil

In Fig. 10 are shown the dependences of the of levels of the magnetic flux density of the initial magnetic field and the resultant magnetic field when the only single third shielding coil of system of active shielding is on as a function of the distance from the extreme conductor of the power line.

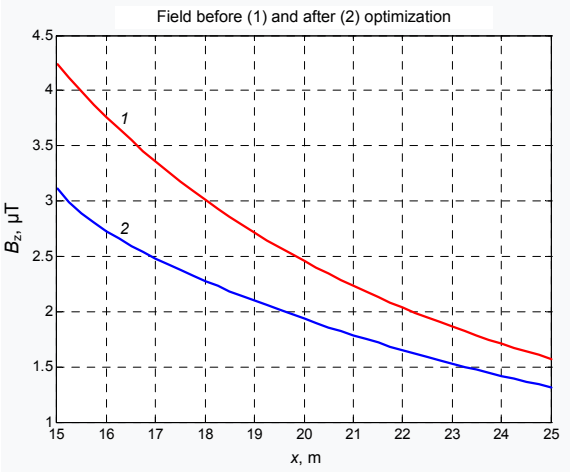

Fig. 10. Comparison of magnetic flux density between with and without system of active shielding with only single third shielding coil

As can be seen from this figure, with only one third of the winding of the active shielding system, the level of the magnetic flux density of the initial magnetic field is reduced in 1.35 times in the considered space from 4.25 μT to the level of 3.25 μT.

Now let us consider the shielding efficiency of the original magnetic field when only both first and second shielding coils are used at optimal values of the regulator of these coils. In Fig. 11 are shown the space-time characteristics of the magnetic flux density vector of magnetic field generated by: 1) overhead power line; 2) only both first and second shielding coils and 3) the resultant magnetic field with the only both first and second shielding coils.

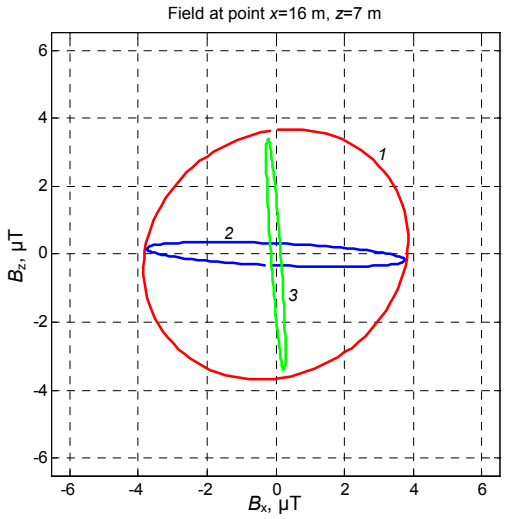

Fig. 11. Comparison between space-time characteristics of magnetic flux density without and with system of active shielding with only both first and second shielding coils and only both first and second shielding coils

In Fig. 12 are shown the dependences of the of levels of the magnetic flux density of the initial magnetic field and the resultant magnetic field when the only both

first and second shielding coils of system of active shielding are on as a function of the distance from the extreme conductor of the power line.

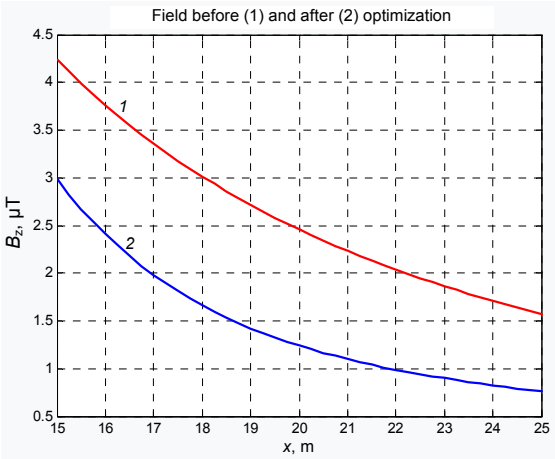

Fig. 12. Comparison of magnetic flux density between with and without system of active shielding with only both first and second shielding coils

As can be seen from this figure, with only both first and second shielding coils of the active shielding system, the level of magnetic flux density of the initial magnetic field is reduced in 1.35 times in the considered space from 4.25 μT to the level of 3.25 μT.

Experimental research. For experimental research, a laboratory model of a three-coil system of active shielding of a magnetic field generated by an air power line in a multi-storey building has been developed.

In Fig. 13 is shown a general view of the layout of the synthesized laboratory model of a three-coil system of active shielding.

Fig. 13. Picture of three shielding coils spatial arrangement of system of active shielding laboratory model

To adjust the model of the system of active shielding, the space-time characteristic of the magnetic field was experimentally measured using two measuring windings and oscilloscope [31, 32].

As an example, in Fig. 14 are shown oscillograms of the output signals of the sensors (*a*) and experimentally measured space-time characteristics (*b*) of the output magnetic field.

In Fig. 15 are shown comparison of magnetic flux density between measurements (solid lines) and simulations (indicated by **+**) with and without system of active shielding.

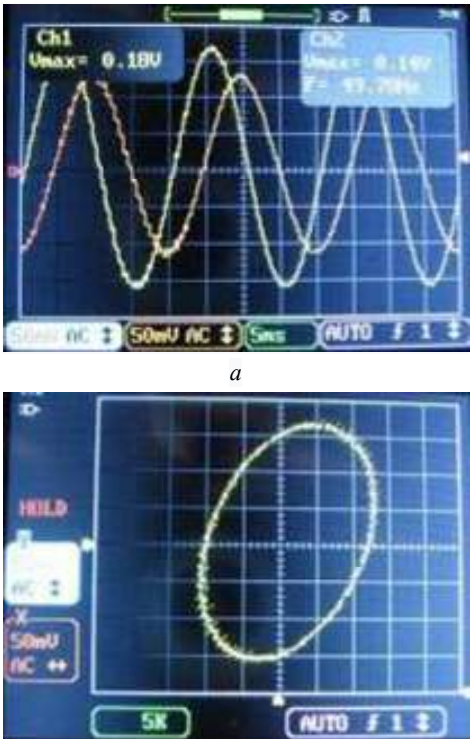

a

b

Fig. 14. Oscillograms of the output signals of the both sensors (*a*) and experimentally measured space-time characteristics (*b*) of the magnetic field

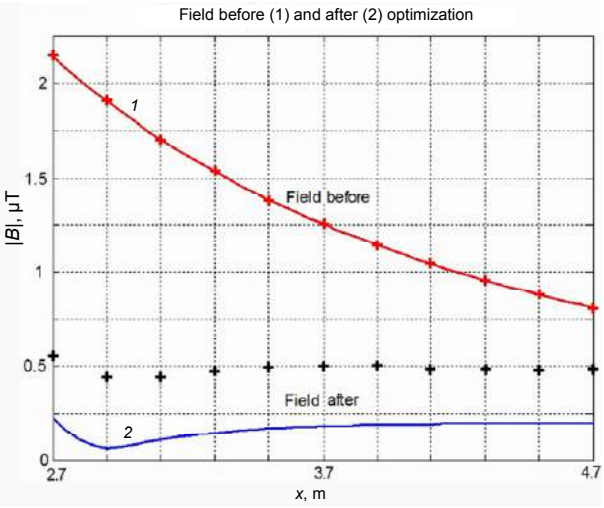

Fig. 15. Comparison of magnetic flux density between measurements (solid lines) and simulations (**+**) with and without system of active shielding

Note that from a comparison of the spatio-temporal characteristics shown in Fig. 9 and Fig. 11 follows that the space-time characteristic of the resulting magnetic field remaining after the operation of the only first and second shielding coil is a highly elongated ellipse. The major axis elongated ellipse spatio-temporal characteristics practically coincides with the space-time characteristics of the magnetic field generated by only one third shielding coil.

As a result, with the help of the third shielding coil, the major axis of the space-time characteristic of the resulting magnetic field, which remains after the operation of the only first and second shielding coils, is compensated effectively. Due to such compensation,

a sufficiently high shielding factor of 10.75 is provided in the system with the simultaneous operation of all three shielding coils.

As can be seen from Fig. 15 the experimental value of the induction level does not exceed 0.5 μT. The deviation of the experimental value of the induction level from the calculated one is due, firstly, to the deviation of the geometric dimensions of the shielding windings from their calculated values, and, secondly, to the inaccuracy of adjusting the parameters of the regulators.

Conclusions.

1. For the first time, to reduce the initial magnetic field in multi-storey building generated by a high-voltage power line by active shielding means, the three-circuits system of active shielding which contains three shielding coils was designed.

2. As a result of computer simulation of the synthesized system, it is shown that with the help of the synthesized system, the level of magnetic flux density of the magnetic field in a multi-storey building generated by a high-voltage power line is reduced by more than 10 times. At the same time, the level of magnetic flux density of the resulting magnetic field in multi-storey building does not exceed the sanitary standards of Ukraine.

3. To set up a laboratory model of a three-circuit system of active shielding, a computer simulation of the effectiveness of shielding the initial magnetic field in a multi-storey building using separate windings was carried out. It is shown, that when only one coil is in operation, the level of the magnetic flux density increases by a factor of 1.2–1.5 due to overcompensation. When only two windings work, it is not possible to ensure the sanitary standards of Ukraine in terms of the magnetic flux density level in the multi-storey building.

4. As the results of experimental studies of a laboratory model of a three-circuit system of active shielding of a magnetic field in a multi-storey building generated by a high-voltage power line are presented, it has been established that the shielding factor is more than 4 units. The deviation of the experimental value of the level of magnetic flux density from the calculated one is due, firstly, to the deviation of the geometric dimensions of the shielding windings from their calculated values, and, secondly, to the inaccuracy of adjusting the parameters of the regulators.

REFERENCES

1. Rozov V.Yu., Grinchenko V.S., Yerisov A.V., Dobrodeyev P.N. Efficient shielding of three-phase cable line magnetic field by passive loop under limited thermal effect on power cables. *Electrical Engineering & Electromechanics*, 2019, no. 6, pp. 50-54. doi: https://doi.org/10.20998/2074-272x.2019.6.07.

2. Rozov V., Grinchenko V. Simulation and analysis of power frequency electromagnetic field in buildings closed to overhead lines. *2017 IEEE First Ukraine Conference on Electrical and Computer Engineering (UKRCON)*, Kyiv, UKraine, 2017, pp. 500-503. doi: https://doi.org/10.1109/ukrcon.2017.8100538.

3. Rozov V.Yu., Kundius K.D., Pelevin D.Ye. Active shielding of external magnetic field of built-in transformer substations. *Electrical Engineering & Electromechanics*, 2020, no. 3, pp. 24-30. doi: https://doi.org/10.20998/2074-272x.2020.3.04.

4. Rozov V.Y., Zavalnyi A.V., Zolotov S.M., Gretskikh S.V. The normalization methods of the static geomagnetic field inside houses. *Electrical Engineering & Electromechanics*, 2015, no. 2, pp. 35-40. doi: https://doi.org/10.20998/2074-272x.2015.2.07.

5. Salceanu A., Paulet M., Alistar B.D., Asiminicesei O. Upon the contribution of image currents on the magnetic fields generated by overhead power lines. *2019 International Conference on Electromechanical and Energy Systems (SIELMEN)*. 2019. doi: https://doi.org/10.1109/sielmen.2019.8905880.

6. Del Pino Lopez J.C., Romero P.C. Influence of different types of magnetic shields on the thermal behavior and ampacity of underground power cables. *IEEE Transactions on Power Delivery*, Oct. 2011, vol. 26, no. 4, pp. 2659-2667. doi: https://doi.org/10.1109/tpwrd.2011.2158593.

7. Ippolito L., Siano P. Using multi-objective optimal power flow for reducing magnetic fields from power lines. *Electric Power Systems Research*, Feb. 2004, vol. 68, no. 2, pp. 93-101. doi: https://doi.org/10.1016/s0378-7796(03)00151-2.

8. Barsali S., Giglioli R., Poli D. Active shielding of overhead line magnetic field: Design and applications. *Electric Power Systems Research*, May 2014, vol. 110, pp. 55-63. doi: https://doi.org/10.1016/j.epsr.2014.01.005.

9. Bavastro D., Canova A., Freschi F., Giaccone L., Manca M. Magnetic field mitigation at power frequency: design principles and case studies. *IEEE Transactions on Industry Applications*, May 2015, vol. 51, no. 3, pp. 2009-2016. doi: https://doi.org/10.1109/tia.2014.2369813.

10. Beltran H., Fuster V., García M. Magnetic field reduction screening system for a magnetic field source used in industrial applications. *9 Congreso Hispano Luso de Ingeniería Eléctrica (9 CHLIE)*, Marbella (Málaga, Spain), 2005, pp. 84-99. Available at: https://www.researchgate.net/publication/229020921_Magnetic_field_reduction_screening_system_for_a_magnetic_field_source_used_in_industrial_applications (Accessed 28.10.2020).

11. Bravo-Rodríguez J., Del-Pino-López J., Cruz-Romero P. A Survey on Optimization Techniques Applied to Magnetic Field Mitigation in Power Systems. *Energies*, 2019, vol. 12, no. 7, p. 1332. doi: https://doi.org/10.3390/en12071332.

12. Canova A., del-Pino-López J.C., Giaccone L., Manca M. Active Shielding System for ELF Magnetic Fields. *IEEE Transactions on Magnetics*, March 2015, vol. 51, no. 3, pp. 1-4. doi: https://doi.org/10.1109/tmag.2014.2354515.

13. Canova A., Giaccone L. Real-time optimization of active loops for the magnetic field minimization. *International Journal of Applied Electromagnetics and Mechanics*, Feb. 2018, vol. 56, pp. 97-106. doi: https://doi.org/10.3233/jae-172286.

14. Canova A., Giaccone L., Cirimele V. Active and passive shield for aerial power lines. *Proc. of the 25th International Conference on Electricity Distribution (CIRED 2019)*, 3-6 June 2019, Madrid, Spain. Paper no. 1096. Available at: https://www.cired-repository.org/handle/20.500.12455/290 (Accessed 28.10.2020).

15. Canova A., Giaccone L. High-performance magnetic shielding solution for extremely low frequency (ELF) sources. *CIRED - Open Access Proceedings Journal*, Oct. 2017, vol. 2017, no. 1, pp. 686-690. doi: https://doi.org/10.1049/oap-cired.2017.1029.

16. Celozzi S. Active compensation and partial shields for the power-frequency magnetic field reduction. *2002 IEEE International Symposium on Electromagnetic Compatibility*, Minneapolis, MN, USA, 2002, vol. 1, pp. 222-226. doi: https://doi.org/10.1109/isemc.2002.1032478.

17. Celozzi S., Garzia F. Active shielding for power-frequency magnetic field reduction using genetic algorithms optimization. *IEE Proceedings - Science, Measurement and Technology*, 2004, vol. 151, no. 1, pp. 2-7. doi: https://doi.org/10.1049/ip-smt:20040002.

18. Celozzi S., Garzia F. Magnetic field reduction by means of active shielding techniques. *WIT Transactions on Biomedicine*

and Health, 2003, vol. 7, pp. 79-89. doi: https://doi.org/10.2495/ehr030091.
19. Buriakovskyi S.G., Maslii A.S., Pasko O.V., Smirnov V.V. Mathematical modelling of transients in the electric drive of the switch – the main executive element of railway automation. *Electrical Engineering & Electromechanics*, 2020, no. 4, pp. 17-23. doi: https://doi.org/10.20998/2074-272X.2020.4.03.
20. Ostroverkhov M., Chumack V., Monakhov E., Ponomarev A. Hybrid Excited Synchronous Generator for Microhydropower Unit. *2019 IEEE 6th International Conference on Energy Smart Systems (ESS)*, Kyiv, Ukraine, 2019, pp. 219-222. doi: https://doi.org/10.1109/ess.2019.8764202.
21. Ostroverkhov M., Chumack V., Monakhov E. Ouput Voltage Stabilization Process Simulation in Generator with Hybrid Excitation at Variable Drive Speed. *2019 IEEE 2nd Ukraine Conference on Electrical and Computer Engineering (UKRCON)*, Lviv, Ukraine, 2019, pp. 310-313. doi: https://doi.org/10.1109/ukrcon.2019.8879781.
22. Tytiuk V., Chornyi O., Baranovskaya M., Serhiienko S., Zachepa I., Tsvirkun L., Kuznetsov V., Tryputen N. Synthesis of a fractional-order $PI^{\lambda}D^{\mu}$-controller for a closed system of switched reluctance motor control. *Eastern-European Journal of Enterprise Technologies*, 2019, no. 2 (98), pp. 35-42. doi: https://doi.org/10.15587/1729-4061.2019.160946.
23. Zagirnyak M., Chornyi O., Zachepa I. The autonomous sources of energy supply for the liquidation of technogenic accidents. *Przeglad Elektrotechniczny*, 2019, no. 5, pp. 47-50. doi: https://doi.org/10.15199/48.2019.05.12.
24. Chornyi O., Serhiienko S. A virtual complex with the parametric adjustment to electromechanical system parameters. *Technical Electrodynamics*, 2019, pp. 38-41. doi: https://doi.org/10.15407/techned2019.01.038.
25. Shchur I., Kasha L., Bukavyn M. Efficiency Evaluation of Single and Modular Cascade Machines Operation in Electric Vehicle. *2020 IEEE 15th International Conference on Advanced Trends in Radioelectronics, Telecommunications and Computer Engineering (TCSET)*, Lviv-Slavske, Ukraine, 2020, pp. 156-161. doi: https://doi.org/10.1109/tcset49122.2020.235413.
26. Shchur I., Turkovskyi V. Comparative Study of Brushless DC Motor Drives with Different Configurations of Modular Multilevel Cascaded Converters. *2020 IEEE 15th International Conference on Advanced Trends in Radioelectronics, Telecommunications and Computer Engineering (TCSET)*, Lviv-Slavske, Ukraine, 2020, pp. 447-451. doi: https://doi.org/10.1109/tcset49122.2020.235473.
27. Sushchenko O.A., Shyrokyi O.V. H2/H∞ optimization of system for stabilization and control by line-of-sight orientation of devices operated at UAV. *2015 IEEE International Conference Actual Problems of Unmanned Aerial Vehicles Developments (APUAVD)*, Kyiv, UKraine, 2015, pp. 235-238. doi: https://doi.org/10.1109/apuavd.2015.7346608.
28. Sushchenko O.A., Golitsyn V.O. Data processing system for altitude navigation sensor. *2016 4th International Conference on Methods and Systems of Navigation and Motion Control (MSNMC)*, Kiev, Ukraine, 2016, pp. 84-87. doi: https://doi.org/10.1109/msnmc.2016.7783112.
29. Gal'chenko, V.Y., Vorob'ev, M.A. Structural synthesis of attachable eddy-current probes with a given distribution of the probing field in the test zone. *Russian Journal of Nondestructive Testing*, Jan. 2005, vol. 41, no. 1, pp. 29-33. doi: https://doi.org/10.1007/s11181-005-0124-7.
30. Halchenko, V.Y., Ostapushchenko, D.L. & Vorobyov, M.A. Mathematical simulation of magnetization processes of arbitrarily shaped ferromagnetic test objects in fields of given spatial configurations. *Russian Journal of Nondestructive Testing*, Sep. 2008, vol. 44, no. 9, pp. 589-600. doi: https://doi.org/10.1134/S1061830908090015.
31. Chystiakov P., Chornyi O., Zhautikov B., Sivyakova G. Remote control of electromechanical systems based on computer simulators. *2017 International Conference on Modern Electrical and Energy Systems (MEES)*, Kremenchuk, Ukraine, 2017, pp. 364-367. doi: https://doi.org/10.1109/mees.2017.8248934.
32. Zagirnyak M., Bisikalo O., Chorna O., Chornyi O. A Model of the Assessment of an Induction Motor Condition and Operation Life, Based on the Measurement of the External Magnetic Field. *2018 IEEE 3rd International Conference on Intelligent Energy and Power Systems (IEPS)*, Kharkiv, 2018, pp. 316-321. doi: https://doi.org/10.1109/ieps.2018.8559564.
33. Ummels M. *Stochastic Multiplayer Games Theory and Algorithms*. Amsterdam University Press, 2010. 174 p.
34. Shoham Y., Leyton-Brown K. *Multiagent Systems: Algorithmic, Game-Theoretic, and Logical Foundations*. Cambridge University Press, 2009. 504 p.
35. Ray T., Liew K.M. A Swarm Metaphor for Multiobjective Design Optimization. *Engineering Optimization*, 2002, vol. 34, no. 2, pp. 141-153. doi: https://doi.org/10.1080/03052150210915.
36. Zilzter Eckart. *Evolutionary algorithms for multiobjective optimizations: methods and applications*. PhD Thesis Swiss Federal Institute of Technology, Zurich, 1999. 114 p.
37. Xiaohui Hu, Eberhart R.C., Yuhui Shi. Particle swarm with extended memory for multiobjective optimization. *Proceedings of the 2003 IEEE Swarm Intelligence Symposium*. SIS'03 (Cat. No.03EX706), Indianapolis, IN, USA, 2003, pp. 193-197. doi: https://doi.org/10.1109/sis.2003.1202267.
38. Pulido G.T., Coello C.A.C. A constraint-handling mechanism for particle swarm optimization. *Proceedings of the 2004 Congress on Evolutionary Computation* (IEEE Cat. No.04TH8753), Portland, OR, USA, 2004, vol. 2, pp. 1396-1403. doi: https://doi.org/10.1109/cec.2004.1331060.
39. Michalewicz Z., Schoenauer M. Evolutionary Algorithms for Constrained Parameter Optimization Problems. *Evolutionary Computation*, 1996, vol. 4, no. 1, pp. 1-32. doi: https://doi.org/10.1162/evco.1996.4.1.1.
40. Parsopoulos K.E., Vrahatis M.N. Particle swarm optimization method for constrained optimization problems. *Proceedings of the Euro-International Symposium on Computational Intelligence*, 2002, pp. 174-181.
41. Xin-She Yang, Zhihua Cui, Renbin Xiao, Amir Hossein Gandomi, Mehmet Karamanoglu. *Swarm Intelligence and Bio-Inspired Computation: Theory and Applications*, Elsevier Inc., 2013. 450 p.

Received 28.12.2020
Accepted 05.02.2020
Published 05.04.2021

B.I. Kuznetsov[1], *Doctor of Technical Science, Professor,*
T.B. Nikitina[2], *Doctor of Technical Science, Professor,*
I.V. Bovdui[1], *PhD, Senior Research Scientist,*
V.V. Kolomiets[3], *PhD, Associate Professor,*
B.B. Kobylianskiy[3], *PhD, Associate Professor,*
[1] State Institution «Institute of Technical Problems of Magnetism of the National Academy of Sciences of Ukraine»,
19, Industrialna Str., Kharkiv, 61106, Ukraine.
e-mail: kuznetsov.boris.i@gmail.com
[2] Kharkov National Automobile and Highway University,
25, Yaroslava Mudroho Str., Kharkov, 61002, Ukraine,
e-mail: tatjana55555@gmail.com
[3] Educational scientific professional pedagogical Institute of Ukrainian Engineering Pedagogical Academy,
9a, Nosakov Str., Bakhmut, Donetsk Region, 84511, Ukraine,
e-mail: nnppiuipa@ukr.net

How to cite this article:
Kuznetsov B.I., Nikitina T.B., Bovdui I.V., Kolomiets V.V., Kobylianskiy B.B. Overhead power lines magnetic field reducing in multi-story building by active shielding means. *Electrical Engineering & Electromechanics*, 2021, no. 2, pp. 23-29. **doi: 10.20998/2074-272X.2021.2.04.**

UDC 621.314 **doi: 10.20998/2074-272X.2021.2.05**

D.S. Krylov, O.I. Kholod

THE EFFICIENCY OF THE ACTIVE CONTROLLED RECTIFIER OPERATION IN THE MAINS VOLTAGE DISTORTION MODE

Goal. *Checking the efficiency of the active rectifier with differences types of control systems in conditions of deep voltage distortions of a three-phase three-wire supply network.* ***Methodology***. *The authors have used the Matlab/Simulink software environment to create a model of an active rectifier with various types of control systems as part of a frequency electric drive. We performed a series of simulations of the operating modes of an active rectifier with various control systems when the supply voltage is distorted.* ***Results***. *When the active rectifier is operating in an unregulated mode, the distortions of the current and mains voltage exceed the maximum permissible values. The quality indicators of the mains current and mains voltage are significantly higher than the normally permissible values. In the absence of voltage distortions in the supply network, the operation of the active rectifier can effectively eliminate the distortions of the mains current, regardless of the type of control system of the active rectifier. In conditions of deep distortions of the supply network voltage, the operation of an active rectifier with a vector control system is more efficient than with a parametric control system.* ***Originality***. *Criteria for determining the quality of consumed electricity at the connection point of the circuit are proposed.* ***Practical significance***. *Recommendations have been developed for the use of active rectifier control systems when working with a distorted power supply voltage.* References 8, tables 4, figures 11.

Key words: **active rectifier, vector control system, parametric control system, PWM frequency, mains voltage distortion, mains current distortion, total harmonic distortion.**

Розглянуто роботу активного керованого випрямляча-джерела напруги (АВДН) з параметричною та векторною системами управління, які працюють з фіксованою частотою модуляції в складі електроприводу потужністю 315 кВт паралельно з іншими навантаженнями в умовах спотворення напруги джерела живлення. Виконано математичне моделювання АВДН з різними системами управління. Запропоновано критерії визначення якості споживаної електроенергії в точці підключення схеми. Розроблено рекомендації щодо використання систем управління АВДН при роботі зі спотвореною напругою джерела живлення. Бібл. 8, табл. 4, рис. 11.

Ключові слова: **активний випрямляч, векторна система управління, параметрична система управління, частота ШІМ, спотворення напруги мережі, спотворення струму мережі, сумарний коефіцієнт гармонійних спотворень.**

Рассмотрена работа активного управляемого выпрямителя-источника напряжения (АВИН) с параметрической и векторной системами управления, работающих с фиксированной частотой модуляции в составе электропривода мощностью 315 кВт параллельно с другими нагрузками в условиях искажённого напряжения источника питания. Выполнено математическое моделирование АВИН с различными системами управления. Предложены критерии определения качества потребляемой электроэнергии в точке подключения схемы. Разработаны рекомендации по использованию систем управления АВИН при работе с искажённым напряжением источника питания. Библ. 8, табл. 4, рис. 11.

Ключевые слова: **активный выпрямитель, векторная система управления, параметрическая система управления, частота ШИМ, искажения напряжения сети, искажения сетевого тока, суммарный коэффициент гармонических искажений.**

Introduction. Voltage-sources active rectifiers (VSARs) are increasingly used in the input circuits of medium-power industrial drives based on autonomous voltage inverters, providing a two-way exchange of energy between the motor and the mains with an almost sinusoidal current at the input of the circuit with a zero phase shift relative to the phase voltage [1-3]. The efficiency of the VSAR circuit is ensured, first of all, by the correct choice of the structure of its control system [4, 5]. In [6], the authors analyzed the efficiency of the basic circuits of control systems (CS) of the VSAR when they implement the main functions assigned to the power circuit of the converter, and also proposed a new structure of the CS based on the theory of representing instantaneous currents and voltages of a three-phase network in the form of generalized vectors in *p-q-r* coordinates. The complication of the CS of the VSAR is justified when using the converter in an industrial workshop, where several loads can be powered from a common source, which mutually influence each other, i.e. in conditions where long-term distortion is possible in the supply voltage.

The goal of the work is to test the efficiency of the VSAR operation with various types of control systems in conditions of deep voltage distortions of a three-phase three-wire mains supply.

The structure of the drive power supply circuit. The block diagram of the investigated frequency electric drive of medium power using a three-phase voltage-sources active rectifiers is shown in Fig. 1.

It contains: a source of three-phase AC voltage u_S; converter transformer T; input reactors of the VSAR, which, if necessary, can be combined with a high pass filter HPF; an active rectifier AR, made in bridge circuit on alternating current switches; two capacitors C_1 and C_2 of the same capacitance connected in the intermediate DC circuit; a three-phase bridge autonomous voltage inverter VI, also made according to a bridge circuit on alternating current keys and loaded on a three-phase induction machine (load) L. The converter transformer T, in the general case, can also supply other loads OL connected to the terminals of its valve windings in parallel to the circuit under study.

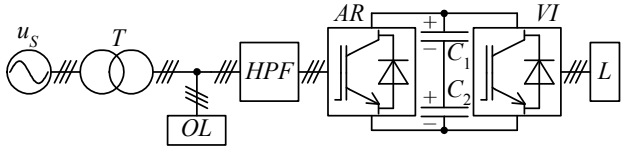

Fig. 1. Block diagram of a frequency electric drive with VSAR

In practice, this circuit should also contain switching and protective devices, as well as the output filter of the voltage inverter. They are not shown in Fig. 1, since they do not have a significant effect on the operation of the VSAR and are not the subject of this paper.

For the correct perception of the results obtained in the framework of studies consistently carried out by the authors, the parameters of the main elements of the system under consideration were taken the same as in [6].

The prototype of the load was an ABB induction motor type M3BP 355 SMC4, whose passport data are given in Table 1.

Table 1

Load parameters

Parameter	Value
Stator line voltage, V	400
Rated frequency, Hz	50
Rated power, kW	315
Rated stator current, A	553

Since the study of the dynamics of the operation of an induction electric drive is not the purpose of this paper, and most VSAR control systems easily cope with the task of recuperation, the load model is represented by an equivalent *RL* circuit that provides the same power at the load.

The CS of the VI is built on the principle of sinusoidal pulse-width modulation with a frequency and depth of regulation fixed at 4 kHz, set by a closed-loop automatic control system with feedback on the input power of the inverter, maintained in any mode at the level of the rated active power of the motor, i.e. 315 kW. The frequency of operation of the VSAR switch in all modes is also adopted equal to 4 kHz.

The total capacitance of the DC link is selected equal to 28 mF from the condition of ensuring the required level of ripple of the rectified voltage, both in uncontrolled and in the active mode of AR operation. The value of the input inductance of the VSAr phase is taken equal to 150 μH, which, in combination with the present inductance of the supply mains, ensures stable operation of the circuit in all modes.

The short-circuit power of the supply mains at the connection point of the converter is 150 MVA.

The converter transformer with installed power of 1 MVA ensures the conversion of the line voltage of the supply mains at the level of 6 kV into line voltage 0.4 kV with the possibility of parallel connection of two more similar converters or another load of the corresponding power.

Quality assessment criteria. When assessing the quality of consumed electricity and the level of influence of the converter on the supply mains, it is necessary to set the main criteria by which we will assess the degree of success in the application of a particular technical solution.

According to [7, 8], it is possible to accurately determine the degree of mutual influence of the converter and the supply mains by calculating the *total harmonic distortion THD* of the voltage and current of the supply mains, as well as *the voltage unbalance factor for the reverse and zero sequence* at the converter connection point to the mains.

The total harmonic distortion is defined [7, 8] as the ratio of the root-mean-square sum of the higher harmonics of the signal to its first harmonic and is usually taken as a percentage. For phase current and mains voltage, it is defined as

$$THD_I = \frac{\sqrt{\sum_{k=2}^{\infty} I_k^2}}{I_1} 100\%, \quad (1)$$

$$THD_U = \frac{\sqrt{\sum_{k=2}^{\infty} U_k^2}}{U_1} 100\%, \quad (2)$$

where I_k and U_k are the effective values of the k-th harmonic of the phase current and voltage at the point where the converter is connected to the network; I_1 and U_1 are the effective values of the 1st harmonic of the phase current and voltage at the connection point.

The voltage unbalance factor in the reverse sequence can be determined from the expression [7]

$$K_{NS2} = \frac{U_{2(1)}}{U_{1(1)}} 100\%, \quad (3)$$

where $U_{1(1)}$ and $U_{2(1)}$ are the effective voltage values, respectively, of the positive and negative sequence of the fundamental frequency of the three-phase voltage system, which can be defined as [7]

$$U_{1(1)} = \sqrt{\frac{1}{12}\left[\left(\sqrt{3}U_{AB(1)} + \sqrt{4U_{BC(1)}^2 - \left(\frac{U_{BC(1)}^2 - U_{CA(1)}^2}{U_{AB(1)}} + U_{AB(1)}\right)^2}\right)^2 + \left(\frac{U_{BC(1)}^2 - U_{CA(1)}^2}{U_{AB(1)}}\right)^2\right]}; \quad (4)$$

$$U_{2(1)} = \sqrt{\frac{1}{12}\left[\left(\sqrt{3}U_{AB(1)} - \sqrt{4U_{BC(1)}^2 - \left(\frac{U_{BC(1)}^2 - U_{CA(1)}^2}{U_{AB(1)}} + U_{AB(1)}\right)^2}\right)^2 + \left(\frac{U_{BC(1)}^2 - U_{CA(1)}^2}{U_{AB(1)}}\right)^2\right]}, \quad (5)$$

where $U_{AB(1)}$, $U_{BC(1)}$, $U_{CA(1)}$ are the effective values of the first harmonics of the line voltages of the supply mains at the converter connection point.

Zero-sequence voltage unbalance factor [7] in the circuit of Fig. 1 is not determined due to the absence of a neutral wire in it.

The structure of the VSAR control system. In [6], the authors showed that among the tracking structures of the CS of the VSAR with a fixed modulation frequency, it is advisable to use the voltage-controlled circuit shown in Fig. 2.

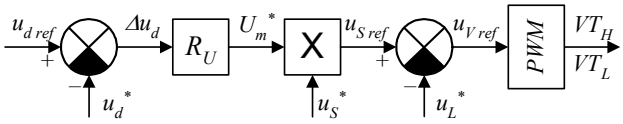

Fig. 2. Block diagram of the CS with voltage control

Its principle of operation is based on the generation of the reference signal of the PWM generator in the form of a voltage difference proportional to the voltage of the mains phase, and a voltage drop across the converter input choke. This allows to eliminate the uncertainty in setting the phase of the current of the supply mains, which arises when fixing the modulation frequency of the circuit, and to maintain its zero value in all operating modes of the circuit [6]. The disadvantage of the structure shown in Fig. 2 is the dependence of the reference signal of the PWM generator on the shape and phase of the supply voltage. This is unacceptable in the mode of deep distortion of the mains voltage and can lead to a significant decrease in the efficiency of VSAR operation.

To combat this, in [6], a structure was proposed that forms a signal for setting the PWM generator which is obtained as a result of representing the mains voltage and current in the form of spatial vectors in a rotating *p-q-r* coordinate system and extracting components proportional to direct sequences of a three-phase system from their projections. This made it possible to create the structure of the VSAR control system, shown in Fig. 3, insensitive to distortion of the power supply voltage.

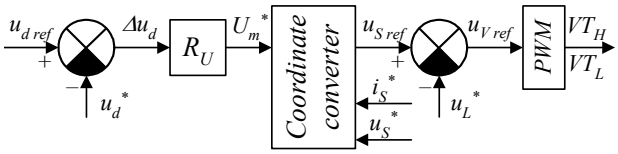

Fig. 3. Block diagram of the CS with vector control

Modelling the operation of the circuit. Modelling the operation of an active rectifier with two structures of control systems is carried out in the Matlab/Simulink software package in relation to a single power circuit corresponding to Fig. 1. The view of the Matlab model of the power circuit of the converter is shown in Fig. 4. It contains the following blocks:

- power circuit – blocks 1, 2, 5, 6, 10-12, 15, 16, 19;
- control systems – blocks 4, 13, 17;
- current and voltage sensors – blocks 3, 7-9, 14;
- parameter calculators – blocks 25, 27, 29;
- information output – blocks 20-24, 26, 28, 30.

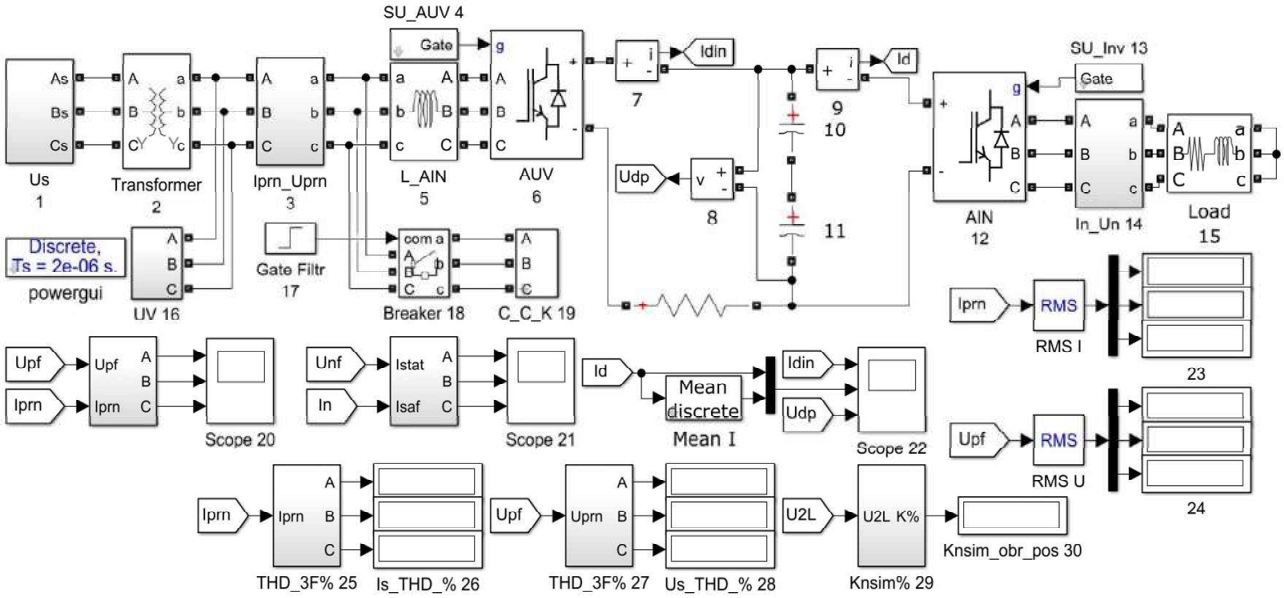

Fig. 4. Matlab model of VSAR power circuit

Purpose of the main blocks of the power circuit: 1 – three-phase AC voltage network; 2 – power transformer; 5 – input reactors of the VSAR; 6 – VSAR bridge; 10, 11 – capacitances of the DC link; 12 – VI bridge; 15 – load; 16 – additional load; 19 – high pass filter.

The parameters of the power circuits of the model are set in strict accordance with the data of the power circuit of the electric drive (Fig. 1), given above. An additional load of the circuit (16) is a six-pulse bridge controlled rectifier with installed power of 300 kW, operating with control angle of 60 electrical degrees. It introduces switching distortions into the voltage of the valve winding of the converter transformer. The high pass filter (19) is designed to combat distortions in the supply voltage at the frequency of VSAR operation. It can be connected to the circuit through the switch (18) at the time specified by block 17. Parameter calculation blocks (25, 27, 29) allow calculating the voltage unbalance factor in negative sequence, harmonic distortions of current and voltage of each phase of the valve winding of the converter transformer and display this data as a percentage (blocks 26, 28, 30). Blocks 23 and 24 display the effective values of the current and voltage of each

phase of the valve winding of the transformer to assess their possible unbalance. Oscilloscope blocks (20-22) allow to visually evaluate the instantaneous values of the circuit parameters.

Simulation is carried out for three variants of VSAR control systems operation (block 4): unregulated mode – transistor control pulses are not generated and VSAR operates in the mode of a diode rectifier; mode of operation with a parametric CS according to the structure of Fig. 2; mode of operation with a vector CS according to the structure of Fig. 3.

The following were taken as long-term distorting factors: switching distortions introduced by an additional load during its parallel operation with the main converter; decrease in the supply voltage of phase *B* by 10 % of the nominal value; phase *C* voltage shift by 130 electrical degrees with respect to phase *B* voltage. All measurements are taken with the high pass filter on.

Figure 5 shows the timing diagrams of the mains voltage and current for an unregulated operating mode (VSAR operates as a diode rectifier) in the absence of additional distortions introduced into the mains voltage as a result of external factors. It can be seen from the diagrams that the shape of the mains current differs significantly from the sinusoid, and its total harmonic distortion (THD_I) is several times higher than the maximum acceptable values, which is confirmed by the data, given in Table 2.

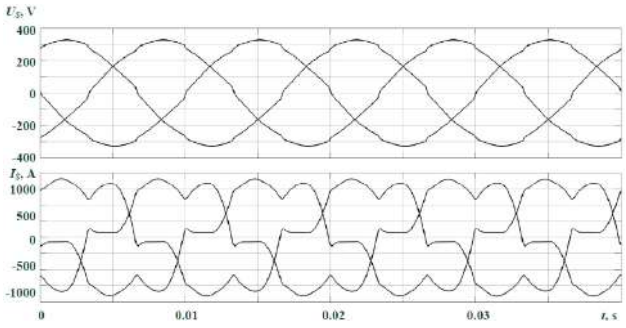

Fig. 5. Mains voltage and current in unregulated mode without distortion of mains parameters

Table 2

Mains parameters for three options of VSAR control systems operation in the absence of external network distortions

Circuit type	Diode rectifier			Parametric VSAR CS			Vector VSAR CS		
phase / parameter	A	B	C	A	B	C	A	B	C
I_2	499,8	499,0	499,9	468	468,1	468,3	467,7	467,8	468,2
U_2	228,2	228,2	228,2	229,4	229,4	229,4	229,4	229,4	229,4
THD_I	25,23	25,37	25,36	2,88	2,86	2,88	2,88	2,85	2,86
THD_U	2,99	2,99	2,99	4,44	4,43	4,44	4,43	4,42	4,43
K_{NS2}	0,002			0,0007			0,0007		

Table 2 also shows that, regardless of the type of the CS, the VSAR allows to effectively eliminate the unwanted generation of higher harmonics of the current into the network and obtain the normally permissible values of THD_I and THD_U.

Analyzing the data from the Table 2, we can talk about the same efficiency of the parametric and vector control systems of the VSAR in the symmetric undistorted network mode. Timing diagrams of the mains voltage and current for this case, shown in Fig. 6 are identical for both types of the CS.

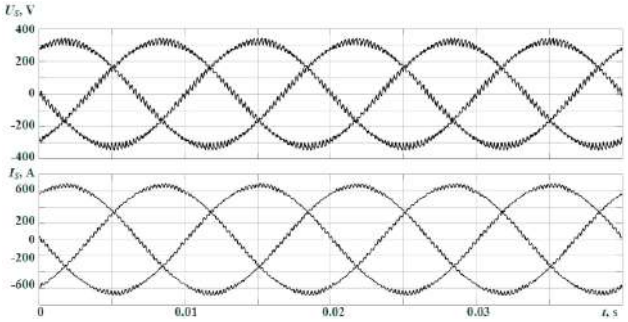

Fig. 6. Mains voltage and current with VSAR in the mode of symmetrical undistorted power supply

The introduction of symmetrical switching distortions from an additional load operating in parallel with the main converter significantly aggravates the picture of the circuit's operation in an unregulated mode and, according to Table 3 provide minor advantages to the vector control system. Timing diagrams of the operation of the circuit in an unregulated mode are shown in Fig. 7. Figure 8 shows diagrams illustrating the operation of the VSAR in the symmetric distortion mode, characteristic of both control systems.

Table 3

Mains parameters for three options of VSAR control system operation in conditions of external symmetric distortions

Circuit type	Diode rectifier			Parametric VSAR CS			Vector VSAR CS		
phase / parameter	A	B	C	A	B	C	A	B	C
I_2	548,0	547,8	549,1	496,9	496,3	496,0	496,6	495,7	496,0
U_2	215,3	215,3	215,3	217,6	217,6	217,6	217,7	217,7	217,7
THD_I	29,75	30,33	30,13	4,95	4,99	5,04	4,75	4,79	4,73
THD_U	7,45	7,43	7,46	9,36	9,39	9,42	9,44	9,47	9,45
K_{NS2}	0,004			0,0006			0,0005		

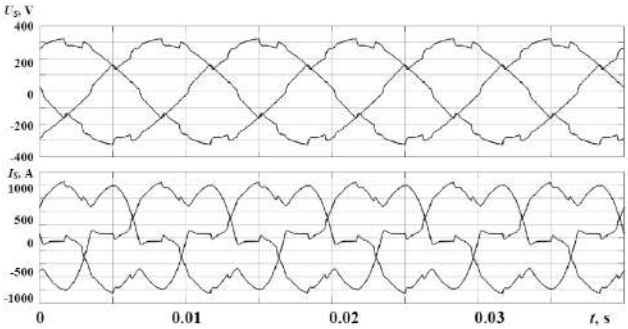

Fig. 7. Mains voltage and current in unregulated mode in conditions of external symmetrical distortions

Let us evaluate the quality of operation of the control systems under consideration, introducing additional asymmetry into the supply voltage.

Figures 9-11 show timing diagrams of the mains voltage and current for three operating modes of the VSAR CS under conditions of external asymmetric distortions of the power supply.

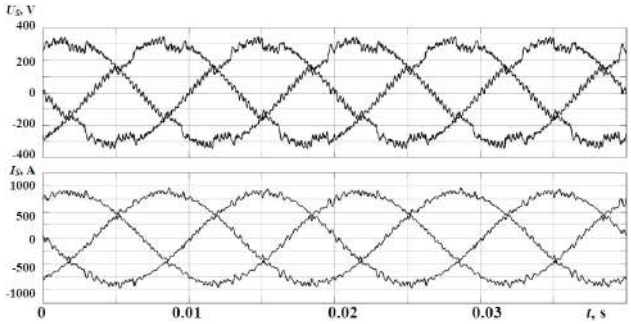

Fig. 8. Mains voltage and current with VSAR in conditions of external symmetric distortions

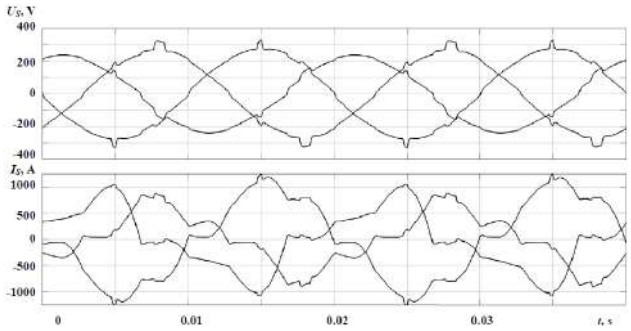

Fig. 9. Mains voltage and current in unregulated mode in deep unbalanced distortion conditions

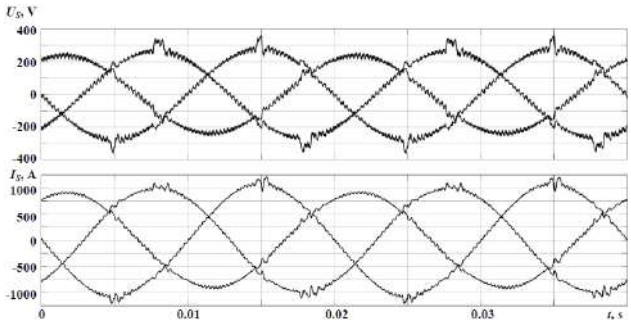

Fig. 10. Mains voltage and current with parametric CS in deep unbalanced distortion conditions

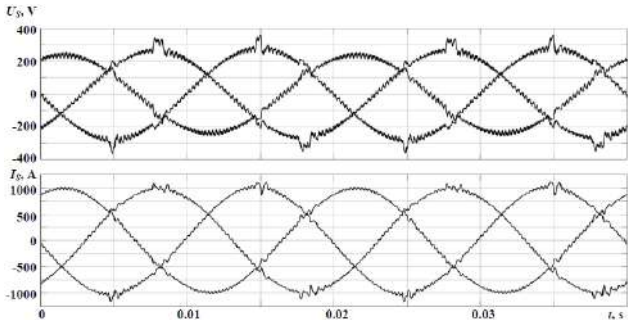

Fig. 11. Mains voltage and current with vector VSAR CS in deep unbalanced distortion conditions

Table 4 shows the indicators for assessing the quality of the mains with deep asymmetric distortions of the power supply voltage for three operating modes of the VSAR CS.

Analysis of the data obtained shows that with deep distortion of the mains parameters and VSAR operation in uncontrolled mode, the mains current and voltage differ significantly from the sinusoid, there is an asymmetry of currents and voltages in phases, THD_I and THD_U indicators are exceeded. When VSAR operates under such conditions, the vector CS is already significantly more efficient than the parametric one – it balances the currents consumed from the network much better.

Table 4

Mains parameters for three options of VSAR control system operation in conditions of deep network distortions

Circuit type	Without VSAR			Parametric CS			Vector CS		
phase / parameter	A	B	C	A	B	C	A	B	C
I_2	775,6	579,4	516,6	611,6	517,1	576,9	580,6	559,6	572,5
U_2	198,4	168,4	193,7	200,6	170,6	194,2	200,9	170,8	194
THD_I	17,08	39,34	30,8	3,5	3,14	3,48	3,4	2,95	3,47
THD_U	4,15	6,54	7,21	6,31	6,66	8,18	6,39	6,69	8,31
K_{NS2}	9,85			9,5			9,51		

The THD_I and THD_U values during operation of the two types of CS are practically the same and comply with the standards [8]. None of the considered CS can improve the symmetry of the supply voltages.

Conclusions.

1. In the conditions of symmetric distortions of the supply voltage, the VSAR vector control system proposed by the authors has a slight advantage over the parametric one.

2. In the presence of unbalance in the voltage of the power source, VSAR with a vector control system consumes a current from the mains, the deviation of the effective value from the nominal value of which does not exceed 2 % in each phase. The deviation of the effective value of the phase current from the nominal in the parametric system reaches 10 % both up and down. That is, in the mode of deep voltage distortion of the supply mains, VSAR with a vector control system balances the current consumed from a three-phase network much better than with a parametric one.

3. VSAR has shown high efficiency in all modes of operation, demonstrating the values permissible by the standards for the total harmonic distortion of the current and voltage of the mains at the connection point. The studies carried out allow to say that the use of vector control systems, according to the authors, is the most promising, and their further research and optimization is an urgent task.

Conflict of interest. The authors declare that they have no conflicts of interest.

REFERENCES

1. Vaideeswaran V., Sankar N. Control Techniques of Three Phase PWM Rectifier. *International Journal of Engineering and Advanced Technology*, 2018, vol. 8, iss. 2S, pp. 148-152. Available at: https://www.ijeat.org/wp-content/uploads/papers/v8i2s/B10391282S18.pdf (Accessed 10.10.2020).

2. Jamma M., Akherraz M., Barar M. ANFIS Based DC-Link Voltage Control of PWM Rectifier-Inverter System with Enhanced Dynamic Performance. *IECON 2018 - 44th Annual Conference of the IEEE Industrial Electronics Society*, Washington, DC, USA, 2018, pp. 2219-2224. doi: https://doi.org/10.1109/iecon.2018.8591620.

3. Premkumar K., Prema Kandasamy, Vishnu Priya M., Thamizhselvan T., Ron Carter S.B. Three-Phase Rectifier Control Techniques: A Comprehensive Literature Survey.

International Journal of Scientific and Technology Research, January 2020, vol. 9, iss. 1, pp. 3183-3188. Available at: http://www.ijstr.org/final-print/jan2020/Three-phase-Rectifier-Control-Techniques-A-Comprehensive-Literature-Survey.pdf (Accessed 10.10.2020).

4. Trinh Q.N., Choo F.H., Tang Y., Wang P. Control Strategy to Compensate for Current and Voltage Measurement Errors in Three-Phase PWM Rectifiers. *IEEE Transactions on Industry Applications*, May 2019, vol. 55, no. 3, pp. 2879-2889. doi: https://doi.org/10.1109/tia.2019.2894107.

5. Zhou D., Li X., Tang Y. Multiple-Vector Model-Predictive Power Control of Three-Phase Four-Switch Rectifiers With Capacitor Voltage Balancing. *IEEE Transactions on Power Electronics*, Jul. 2018, vol. 33, no. 7, pp. 5824-5835. doi: https://doi.org/10.1109/tpel.2017.2750766.

6. Krylov D., Kholod O., Radohuz S. Active rectifier with different control system types. *2020 IEEE 4th International Conference on Intelligent Energy and Power Systems (IEPS)*, Istanbul, Turkey, 2020, pp. 273-278. doi: https://doi.org/10.1109/ieps51250.2020.9263226.

7. Tlili F., Bacha F., Guesmi M. New switching lookup table for direct power control of a three-phase PWM rectifier. *2018 9th International Renewable Energy Congress (IREC)*, Hammamet, Tunisia, 2018, pp. 1-5. doi: https://doi.org/10.1109/irec.2018.8362513.

8. *IEEE STD 519-2014*. Recommended Practice and Requirements for Harmonic Control in Electric Power Systems. doi: https://doi.org/10.1109/IEEESTD.2014.6826459.

Received 10.11.2020
Accepted 29.12.2020
Published 05.04.2021

D.S. Krylov [1]*, PhD, Associate Professor,*
O.I. Kholod [1]*, PhD,*
[1] National Technical University «Kharkiv Polytechnic Institute», 2, Kyrpychova Str., Kharkiv, 61002, Ukraine,
e-mail: Denis.Krylov@khpi.edu.ua, Olha.Kholod@khpi.edu.ua

How to cite this article:
Krylov D.S., Kholod O.I. The efficiency of the active controlled rectifier operation in the mains voltage distortion mode. *Electrical Engineering & Electromechanics*, 2021, no. 2, pp. 30-35. **doi: 10.20998/2074-272X.2021.2.05.**

UDC 620.91:621.31 **doi: 10.20998/2074-272X.2021.2.06**

A.A. Shavelkin, J. Gerlici, I.O. Shvedchykova, K. Kravchenko, H.V. Kruhliak

MANAGEMENT OF POWER CONSUMPTION IN A PHOTOVOLTAIC SYSTEM WITH A STORAGE BATTERY CONNECTED TO THE NETWORK WITH MULTI-ZONE ELECTRICITY PRICING TO SUPPLY THE LOCAL FACILITY OWN NEEDS

Purpose. *Improving the principles of management of photovoltaic system with storage battery and with autonomous functioning during daylight hours for a local object, connected to the grid with multi-zone payment when excluding the generation of energy into the grid.* ***Methodology.*** *Modeling and analysis of energy processes in the photovoltaic system was performed using the Matlab software package. The simulation model of energy processes is based on calculated expressions taking into account the characteristics of the battery. Operability of the proposed solutions are confirmed on an experimental setup based on a standard hybrid inverter.* ***Results.*** *It's shown, that due to the battery energy during the most loaded peak hours and part of the daytime the system operates autonomously and does not depend on possible violations of the quality of electricity in the grid. Scenarios of the recommended load schedule are proposed in accordance with the ratio of the predicted value of the daily energy generation of the photovoltaic battery to its possible maximum value. A simulation model of energy processes in the system with the correction of the recommended load value was developed.* ***Originality.*** *A method of the recommended load calculation with current correction for the actual generation and degree of battery charge is proposed, which allows taking into account differences the actual generation of the photovoltaic battery from its predicted value and the actual load from the recommended one.* ***Practical value****. The obtained solutions are the basis for the design of new and modernization of existing photovoltaic systems of local objects using software and hardware complexes for power consumption management.* References 18, figures 4.

Key words: **multi-zone electricity pricing, energy redistribution, storage battery state of charge, PWM, recommended load scenarios with current correction, simulation.**

Удосконалено принципи управління і перерозподілу енергії, яка накопичується в акумуляторній батареї, в фотоелектричній системі локального об'єкта, підключеного до мережі з багатозонною тарифікацією при виключенні генерації енергії в мережу. За рахунок енергії батареї в найбільш навантажені пікові години та частково в денний час система працює автономно і не залежить від можливих спотворень якості електроенергії в мережі. Запропоновано сценарії рекомендованого графіка навантаження відповідно до відношення прогнозованого значення денної генерації енергії фотоелектричної батареї до її можливого максимального значення. Запропоновано методику розрахунку рекомендованого навантаження з поточним корегуванням за фактичною генерацією і ступенем заряду батареї, що дозволяє врахувати відхилення фактичної генерації фотоелектричної батареї від прогнозного значення і фактичного навантаження від рекомендованого. Розроблено імітаційну модель енергетичних процесів в системі з корегуванням значення рекомендованого навантаження. Працездатність запропонованих рішень підтверджено моделюванням в Matlab і на експериментальній установці на базі стандартного гібридного інвертора. Отримані рішення є основою для проектування нових і модернізації існуючих фотоелектричних систем локальних об'єктів з використанням програмно-технічних комплексів управління електроспоживанням. Бібл. 18, рис. 4.

*Ключові слова***: багатозонний тариф, перерозподіл енергії, ступінь заряду акумулятора, ШІМ, сценарії рекомендованого навантаження з поточним корегуванням, моделювання.**

Усовершенствованы принципы управления и перераспределения энергии, накапливаемой в аккумуляторной батарее, в фотоэлектрической системе локального объекта, подключенного к сети с многозонной тарификацией при исключении генерации энергии в сеть. За счет энергии батареи в наиболее нагруженные пиковые часы и частично в дневное время система работает автономно и не зависит от возможных нарушений качества электроэнергии в сети. Предложено сценарии рекомендованного графика нагрузки в соответствии с отношением прогнозируемого значения дневной генерации энергии фотоэлектрической батареи к ее возможному максимальному значению. Предложена методика расчета рекомендованной нагрузки с текущей корректировкой по фактической генерации и степени заряда батареи, что позволяет учесть отличия фактической генерации фотоэлектрической батареи от прогнозного значения и фактической нагрузки от рекомендованной. Разработана имитационная модель энергетических процессов в системе с корректировкой значения рекомендованной нагрузки. Работоспособность предложенных решений подтверждена моделированием в Matlab и на экспериментальной установке на базе стандартного гибридного инвертора. Полученные решения являются основой для проектирования новых и модернизации существующих фотоэлектрических систем локальных объектов с использованием программно-технических комплексов управления электропотреблением. Библ. 18, рис. 4.

Ключевые слова: **многозонный тариф, перераспределение энергии, степень заряда аккумулятора, ШИМ, сценарии рекомендованной нагрузки с текущей корректировкой, моделирование.**

Introduction. «Green» energy and, first of all, photovoltaic systems (PVSs) are becoming more widespread in modern conditions. This also applies to «small» energy, in particular, economic entities – local facilities (LFs) for various purposes. Here, the use of combined (hybrid) PVSs with a storage battery (SB) and connection to a distribution network (DN) allows: to increase the reliability of power supply due to the uninterruptible power supply function in conditions of voltage outages when using solar generation and SB energy; to increase the power consumption of the LF, this is especially important if there is a limit on the power from the power system, when the use of PVSs is cheaper than the construction of a new power transmission line and equipment for connecting to the DN.

The interest in the sale of electricity at the «green» tariff, along with the provision of their own needs, is not decisive for the LF which is associated with the overestimation of the power of the PVS and with the need for registration of permits. In addition, approaches to «green» tariffs are changing, and the tariffs themselves are decreasing [1]. In this regard, the approach adopted in world practice is promising, when the consumer is a prosumer [2], and energy is consumed where it is generated. This partly alleviates the problems with the management of generation in the power system and the need to ensure the balance of energy.

The effectiveness of the introduction of PVS for business entities is determined in accordance with the increase in production and improved working conditions. At the same time, the introduction of such systems should ensure a reduction in the cost of paying for electricity consumption from the DN, especially taking into account the constant growth of tariffs. It is promising to use a PVS with a SB when connected to DN with multi-zone tariffication with the redistribution of energy between tariff zones [3-5].

The real need for such PVSs is evidenced by the fact that ready-made solutions [6-8] and the development of «hybrid» inverters are widely represented on the electrical market. These solutions represent modern software and hardware complexes: with power supply of the LF from an autonomous voltage inverter (AVI) and switching the LF load to the DN (bypass) with insufficient generation of a photovoltaic battery (PB) and SB energy; with a network inverter (NI), when the load and NI operate in parallel with the DN. These solutions are intended for use in a one-part tariff, have a developed interface with the possibility of remote control of parameters, for example, with output to a smartphone. They have the ability to reconfigure the parameters, but everything is done by the operator, and their effective use requires experience and skills. There are no functions for generating recommendations and automatic adjustment according to the weather forecast.

The cycle of operation of hybrid inverters provides for the power supply of the LF load from the PB with recharging the SB; if the PB energy is insufficient, the SB energy is used. When the state of charge of the SB drops to the threshold value, the transition to the bypass mode is carried out, and the LF load is connected to the DN with the SB charge (from the PB and the DN); if the SB energy is sufficient, the LF is powered again from the SB. The improvement of PVS in the conditions of multi-zone tariffication is associated with the binding of switching of operating modes to the hours of tariff zones, control of the energy supply from the PB and the SB charge. Here, it becomes possible to exclude energy consumption during peak loads [4, 5], the discharge of the SB charged from the night (according to the night rate) in the morning hours until the morning peak is excluded, and the SB is charged until the evening peak.

In real conditions, when using worn out and overloaded DNs, the option with AVI has an advantage, which, if energy consumption is excluded from the DN during peak loads and during light time, ensures the autonomous operation of the LF. In this case, the quality of the LF voltage is determined by the AVI, which will contribute to the normal functioning of the LF in the event of deterioration in the quality of the DN voltage. When using a NI operating in parallel with a DN, switching to stand-alone mode can be accomplished by disconnecting from the DN.

In solutions of PVS with hybrid inverters, the use of a SB is considered, the energy consumption of which W_B varies within wide limits – W_B = 1–4.8 kW·h for a PB with power of P_r=1 kW. Obviously, the W_B value is determined by the system functioning algorithm. At the same time, the cost of the SB is significant and requires justification from the condition of sufficiency.

The use of daily meteorological forecast looks promising with the formation of recommendations on the LF load schedule $P_L(t)$ which will allow planning operation modes and ensuring a reduction in energy consumption from the DN at more expensive tariffs. It becomes possible to automatically adjust according to the season and forecast. Various approaches are used using data from meteorological sites [9]. An interesting and modern solution is forecasting using neural networks [10, 11]. At the same time, the availability of the most accurate forecast does not solve the issue of efficient use of the energy of the PB and SB without linking $P_L(t)$ to it. And here it seems appropriate to use the system with the formation of the $P_{LR}(t)$ load schedule recommended in accordance with the forecast under various operating scenarios. Since it is impossible to ensure an exact match of the $P_{LR}(t)$ load, it is advisable to use the current $P_{LR}(t)$ correction. The correction can be carried out according to the actual parameters of the PVS. This issue requires further study. In this case, the forecast accuracy of the PB generation $P_{PV}(t)$ at the level of the meteorological site data can be sufficient for effective correction [12].

Simulation modelling is an effective tool for studying the possibilities of controlling energy processes in PVS [13-15]. Here, the introduction of additional elements makes it possible to assess the possibilities and efficiency of correcting the $P_{LR}(t)$ load schedule for various deviations of the actual $P_{PVF}(t)$ and the predicted $P_{PVP}(t)$ generation of the PB.

The goal of the work is to improve the management principles for a photovoltaic system with a storage battery and autonomous operation during the daytime for a local facility connected to a multi-zone billing network while excluding the generation of energy to the network.

It is necessary to solve the following tasks:

- to study the possibility of using a limited number of scenarios of operation with the recommended load schedule based on the forecast of the PB generation with the current correction based on the actual values of generation and the degree of SB charge;
- to develop a simulation model of the system to study energy processes in the daily cycle using the recommended load correction;
- to carry out experimental validation using a standard hybrid inverter.

The structure of the power circuits of the PVS. The structure of a PVS with a SB (using the example of a single-phase version of the PVS implementation, see

Fig. 1) is based on a standard approach and contains: an autonomous inverter (VSI) with an output LC filter, PB (PV), SB, Load, DN (G) and switching devices. The PB is connected to the AVI input through a DC/DC1 step-up converter with the Maximum Power Point Tracking (MPPT) function, the SB is connected through a DC/DC2 (charge controller) with two-way conduction. As a starting point, a variant with the use of a hybrid inverter of the Axioma Energy ISMPPT 3000 type (3 kVA) is considered. The LF load is connected to the AVI output and through the K1 contactor with the VS triac – to the DN. The AVI with PWM and an output filter is used as a source of sinusoidal voltage, and when the load is connected to the network, it is used in the SB charging mode. K1 is needed to disconnect the PVS from the DN when the voltage disappears in it (emergency mode). VS is used to exclude a pause when connecting to the DN when the voltage is restored in it (first, K1 is closed, and after synchronizing the AVI voltage u_C with the network voltage u_g, the triac is switched on). Relay K2 is used to switching off the PB. Voltage and current sensors in Fig. 1 are not shown.

Let us consider the operation of the PVS in a daily cycle with autonomous operation when the energy of the PB and the SB is sufficient to consume the LF load and switching to bypass when the energy of the PB and SB is insufficient. A variant of the load graph $P_L(t)$ is shown in Fig. 2 (bypass zones are highlighted). The following conventional zones and relative tariffs have been adopted: daytime T_d=1 (t_2=11:00 – t_5=20:00), nighttime T_n=0.4 (t_6=22:00 – t_1=7:00), peak morning T_m=1.5 (t_1=7:00 – t_2=11:00) and evening T_e=1.5 (t_5=20:00 – t_6=22:00). In this case, an unfavorable option is considered, when the peak loads are shifted by the hours of minimum PB generation.

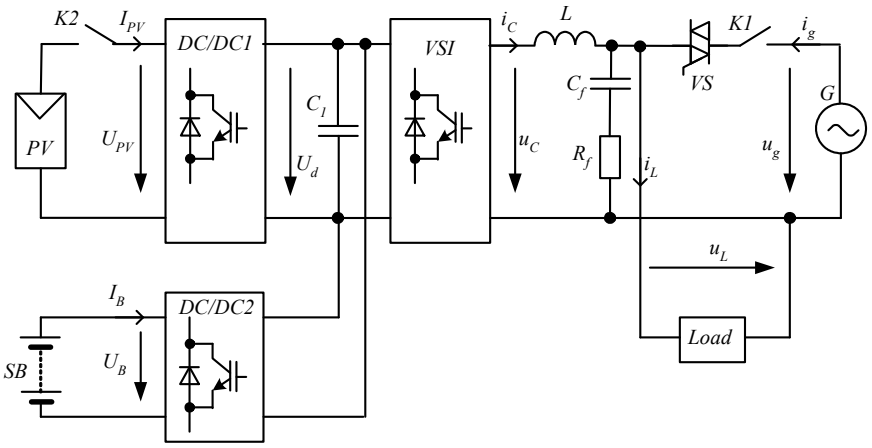

Fig. 1. Structure of the power circuits of the PVS

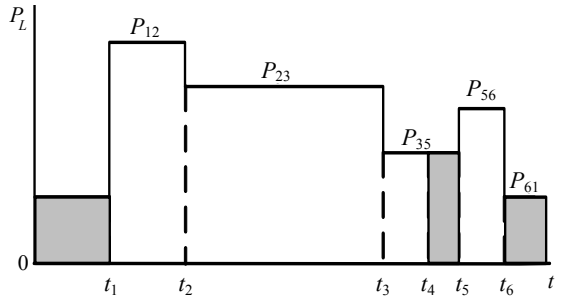

Fig. 2. Dependence $P_L(t)$

In this case, it is necessary to take into account the peculiarities of the charging characteristics of the SB. The standard solution uses a charge in three stages [16, 17]. In this case, the «active» is the first stage when the state of charge (SOC) of the SB Q^*=100·Q/Q_r≤80 % (Q and Q_r are the current and nominal values, respectively), when the charge current I_B for different SB types can vary from 0 to $I_{B\max}$ = (2÷3)I_{Br}= (0.2÷0.3)C_B (C_B is the SB capacitance, I_{Br}=0.1C_B is the nominal value). With further charging, the current decreases significantly and, accordingly, the ability of the SB to receive energy decreases.

The depth of discharge (DOD) and the number of discharge cycles n_{rc} determine the SB life. Usually the acceptable DOD does not exceed 30-50 %. Thus, DOD must be controlled, limited (not lower than 50 %), and SOC must be maintained in the active zone, for example, 75-80 %. This is possible with the use of a relay regulator acting on relay K2 (Fig. 1) with PB disconnection. This applies to the time interval when P_{PV}>P_L and it is possible to charge the SB using the energy of the PB. In the early evening, when $P_{PV} \le P_L$, when Q^* drops to the set value Q^*_d, the load and the inverter are connected to the DN with the SB charge from the PB and the network.

The autonomous operation of the PVS with limited SB capacitance also imposes an additional limitation – the need to reduce the generation of the SB when its energy is excessive and there is nowhere to put it.

We proceed from the data on the generation of the PB $P_{PV}(t)$ in the conditions of Kyiv according to the archival data [18]. As an indicator of the efficiency of PVS, we use a simplified indicator $k_E = C_1 / C_2$ (C_1 and C_2 are the cost of electricity consumed by the LF and the cost of electricity consumed from the DN). Let us consider various options for LF load schedules with constant generation $P_{PV}(t)$ and with a change in the SB capacitance. Energy W_{Bf}, given by the SB, taking into account the efficiency η_B of the SB and the efficiency η_C of the converter is $W_{Bf} = W_B\eta_B\eta_C$ ($W_B = U_BC_B$, U_B is the SB voltage). We accept W_{Bf} values from 1kW·h to 4.8 kW·h. We are considering the option of using lead-

acid SBs of the OPzV12-100 type (12 V, 100 Ah), which at DOD up to 50 % provide for at least 2500 discharge cycles. With a two-hour discharge at U_B=1.85 V, I_B=29.5 A, the discharge power is 57.6 W, and, accordingly, η_B= 0.947 [17]. In this case, the SB is used in the active charging zone up to Q^* = 80 %, and only in the hours preceding the peak hours, it is possible to charge the SB from the network over 80 %.

Mode of operation with constant load from 7:00 to 20:00. In the evening, with a decrease in PB generation, connection to the DN is inevitable at time t_4. We accept the control values Q^*_1=95 %, Q^*_5=85 %, Q^*_4=62 %, Q^*_{min}≥50 %. In accordance with [17], the duration of the SB charge from Q^*_4=62 % to Q^*_5=83-85 % is approximately Δt = 2.5 hours, respectively, t_4=17:30.

In the hours of the evening peak (t_5, t_6) at ΔQ^*_{56} = = $Q^*_5 - Q^*_{min}$, the value of the load power P_{56} can be taken from the condition of providing a two-hour discharge (t_{56} = 2 h)

$$P_{56} = \frac{\Delta Q^*_{56} W_{Bf}}{(t_6 - t_5)100}. \quad (1)$$

For the interval (t_1, t_4) $\Delta Q^*_{14}=Q^*_1-Q^*_4$, W_{PV14} is the energy generated by the PB on the interval (t_1, t_4) in accordance with $P_{PV}(t)$, and the load power $P_L=P_{14}=P_{15}$

$$W_{B14} = \frac{\Delta Q^*_{14} W_{Bf}}{(t_4 - t_1)100}, \quad (2)$$

$$P_{14} = \frac{W_{B14} + W_{PV14}\eta_C}{t_4 - t_1}. \quad (3)$$

To exclude a deep discharge of the SB (Q^*_2≥62 %) during the morning peak hours (t_1, t_2), a similar calculation is performed for P_{12}. The lower power value is taken as P_L.

When charging the SB from the network, energy is consumed:

- on the interval (t_6, t_1) – $W_{BC} = 0.01\Delta Q^*_{61} W_{Bf}$;
- on the interval (t_4, t_5) – $W_{BC45} = 0.01\Delta Q^*_{45} W_{Bf}$.

Part of the SB energy is compensated by the energy W^l_{PV45} generated by the PB at this time – $W^l_{PV45}=W_{PV45}\eta_B\eta_C$ (by t_1 the SB is practically charged, and the PB energy is not used).

We accept the LF night load $P_{LN}=P_{14}/3$. Then

$$k_E = \frac{0.4(t_6 - t_1)P_{LN} + 1.5[P_L(t_2 - t_1) + P_{56}(t_6 - t_5)] + P_L(t_5 - t_2)}{0.4(t_6 - t_1)P_{LN} + 0.4W_{BC} + 1.0W_{BC45} + P_L(t_5 - t_4) - W^l_{PV45}}.$$

The values of the index k_E at W_{PVC} = const (W_{PVC} is the total energy generated by the PB) decrease with increasing W_B. For example, with W_B = 1828 W·h – k_E=3.45, with an increase in capacitance by 1.5 times (W_B=2742 W·h) – k_E=3.4, with an increase in capacitance by 2 times (W_B=3656 W·h) – k_E=3.17. When W_B = 2742 W·h values $Q^*_2=Q^*_4$ i.e. there is a balance between the energy generated by the PB and the consumed by the load. With a smaller SB capacitance, the values $Q^*_2<Q^*_4$, and there is an excess of PB energy after 11:00, which leads to a SB charge Q^*≥80 % and the need to regulate the energy supply from the PB, i.e. the energy of the PB is underused. With a larger SB capacitance, the situation is reversed and $Q^*_4<Q^*_2$. With close values of k_E for W_B=1828 W·h and W_B=2742 W·h, it should be borne in mind that at W_B=1828 W·h, the value of the load power $P_{12}\approx P_{AVD}$ (P_{AVD} is the average value of the PB generation power per day), and in the evening peak P_{56} is almost half as low. At W_B=2742 W·h, the value of P_{56} is close to P_{AVD}, and P_{12} exceeds P_{AVD}, i.e. this value of the SB capacitance is preferable.

The solar activity time for the summer period is limited to t_3=16:30 and the k_E value can be increased (up to k_E=(4.1–4.6)) with a decrease in P_L in the interval (t_3, t_5). Here, P_{13} increases. However, the capacity of the SB is underused during the morning peak hours.

Let us consider the option $P_L(t)$ (Fig. 2) while ensuring the maximum value of P_{12} and reducing the load P_{35}. This will reduce the bypass time to 1.5 hours (t_4=18:30), which is enough to charge the SB by 10 %. We assume that Q^*_1=95 %, Q^*_2=55 %, Q^*_3=78 % (less than 80 %), Q^*_4=75 %, Q^*_5=85 %.

The values of W_{B12}, W_{B23}, W_{B34} are determined in accordance with (2), P_{12}, P_{23}, $P_{34}=P_{45}$ – in accordance with (3), P_{56} – in accordance with (1). Then

$$k_E = \frac{0.4(t_6 - t_1)P_{LN} + 1.5[P_{12}(t_2 - t_1) + P_{56}(t_6 - t_5)] + P_{23}(t_3 - t_2) + P_{34}(t_5 - t_3)}{0.4(t_6 - t_1)P_{LN} + 0.4W_{BC} + W_{BC45} + P_{45}(t_5 - t_4) - W^1_{PV45}}.$$

According to the calculation results, we have the same situation with respect to k_E at different values of the SB capacitance: W_B=1828, 2742, 3656 kW·h, when k_E=5.47, 5.15, 4.73. Based on the possibility of providing close to P_{AVD} values of P_{23} and P_{56} with an increase in P_{12}, it is preferable to use a SB with W_B=2742 kW·h. Also, the SB must be able to accept the energy of the PB. Typically allowable charging current is $I_B \le (0.2 \div 0.3)C_B$. The maximum value of the PB power for a clear day in June [18] is $P_{PV\max}=0.76P_{PV}$. The SB with W_B=2742 W·h is capable of accepting the excess energy of the PB at $P_L \ge 0.42P_{PVAD}$ and current $I_B=0.2C_B$, and at $I_B=0.277C_B$ – even at P_L=0. Thus, P_{PV}: W_B=1:2.74 is accepted.

Solar generation depends on the season of the year and weather conditions, and the recommended load also needs to be changed. At the first stage of development, three $P_{LR}(t)$ scenarios were considered, which are determined by the ratio $w=W_{PVP}/W_{PV\max}$ (W_{PVP} is the energy generated by the PB for the current day according to the forecast, $W_{PV\max}$ is the maximum value of the PB generation according to statistical data on a clear summer day). With PB power of 1 kW in the conditions of Kyiv [18], according to $W_{PV\max}$, the average power value per 24 hours is $P_{PVC}\approx 250$, for a day P_{AVD}=500 W. If $w \ge 0.7$, the load scenario CS1 is selected, if $0.7 > w \ge 0.4$ – CS2, if $0.4 > w$ – CS3.

The CS1 scenario is focused on the maximum use of the energy of the PB and the SB during peak hours and in the daytime (Fig. 2), the calculation of power values is discussed above.

The goal of the CS2 scenario is to increase the average load power during the day, with a certain increase in the duration of the bypass in the evening from 17:30 (t_4) to 20:00. In this case, we have three stages of load change: (t_1, t_3=16.30), (t_3, t_5), (t_5, t_6). We take the value $P_{35}=0.7P_{13}$, Q^*_4=62 %, Q^*_1=95 %. The energy consumed in the interval (t_1, t_4) by the load is $W_{L14}=P_{13}(t_3 - t_1)+0.7P_{13}(t_4 - t_3)=P_{13}[(t_3 - t_1)+0.7(t_4 - t_3)]$. The value

$W_{L14}=\eta_C \cdot W_{PV14}+W_{B14}$. The value of P_{12} is also determined from the condition $\Delta Q^*_{12} \le 40$ %. Accordingly, the condition $P_{13} \le P_{12}$ must be satisfied. The P_{56} value is determined by (1). Thus, until 17:30, 1/3 of the SB energy ($\Delta Q^*_{14}=33$ %) is used, which is added to the PB energy, which, at $w=0.7$, allows providing an average value of the load power at the level of $0.8P_{AVD}$, at $w=0.4$ – at the level of $0.5P_{AVD}$.

In the CS3 scenario, bypass prevails, and it is realistic to exclude energy consumption from the DN during peak hours due to the SB power. Load schedule is similar to CS2. It makes no sense to take P_{LR} by calculation, since this value is small. Therefore, the value of P_{12} is taken at the level of $P_{12}=0.5P_{AVD}$ with a conscious increase in the cost of paying for electricity. Also, in the daytime, a restriction of $Q^* \ge 60$ % is introduced, since in the event of an emergency shutdown of the DN with low PB generation, it is possible to remain without electricity at night. The P_{56} value is determined by (1). On a clear winter day at $w \approx 0.3$ in the midday hours, P_{PV} exceeds the value of P_{AVD}, therefore, the PVS operates autonomously at this time.

The basis for the formation of the recommended load schedule is the meteorological forecast, which can change during the day, the predicted values of P_{PVP} differ from the actual generation P_{PVF}. The values that the actual LF load can take have a certain discreteness and cannot exactly correspond to the recommendations; the peculiarities of the LF functioning should also be taken into account. Thus, there is a need for current adjustment of the recommendations, which is possible based on the values of P_{PVP} and P_{PVF}, as well as the actual degree of charge in Q^*_F.

The averaged value of P_{PVFi} is used in the 5-10 min interval preceding the time t_i when the correction is made. The value $p_i=P_{PVFi}/P_{PVPi}$ (P_{PVPi} is the value at the moment t_i) is determined. The value of the PB energy at the corresponding stage $P_{LR}(t)$, starting from t_i, is taken equal to $W_{PVi}=p_i W_{PVPi}$ (W_{PVPi} is the predicted value). The $P_{LR}(t)$ value is recalculated according to the expressions (1)–(3) corresponding to the current stage of the schedule. At the next correction point t_{i+1}, the procedure is similar.

To test the effectiveness of this method, a simulation model of energy processes in a PVS was developed using a Correction Load Unit (CLU). Here, it is possible to adjust the LF load in a step-by-step mode with the use of a programmable pause and subsequent continuation of the simulation. The correction step is 0.5 h. The CLU includes a set of sampling-storage devices with a 0.5 h step for measuring the values of P_{PVF}, P_{PVP}, Q^*_F. PLR(t) is calculated using expressions corresponding to the selected scenario.

W_{PVP} values for the time intervals corresponding to the correction points 7:00, 7:30,… 20:00 (for example, for point 7:30 in the CS1 scenario this is the interval (7:30 – 11:00)), the duration of the intervals (in this case, $t_2-t_i=3.5$ h), as well as the control values Q^*_C by intervals (in this case $Q^*_C=Q^*_2=55$ %) are set in tabular form. Also, the dependencies $P_{PVP}(t)$ are set in tabular form (according to archival data [18] for Kyiv city at $P_{PVr}=1$ kW), $P_{PVF}(t)$ and $P_{LR1}(t)$ is the recommended load schedule according to the forecast at the moment t_1=7:00. The P_L correction is carried out directly in the $P_{LR1}(t)$ table. The k_E value per 24 h is also calculated.

The SB model is made according to the catalog data. SB charge taking into account energy losses $Q = Q_S + \int I^1_B \cdot dt$, where Q_S is the initial value, $I^1_B = I_B \eta_B$ – when charging and $I^1_B = I_B/\eta_B$ – when discharging the SB. The I_B value is formed in accordance with the SB charging characteristics [17] in the form of $I_B(Q^*)$. In the discharge mode, a limitation of the permissible value of $I_{Brc\max}$ was introduced for 30 min. This is implemented using an adjustable limit, when the upper limit is set as $I_B(Q^*)$, and the lower limit is $I_{Brc\max}$. The SB voltage is also set as the $U_B(Q^*)$ dependence. I_B value in the stand-alone mode

$$I_B = \frac{K_2 P_{PV} \cdot \eta_C - P_L}{U_B},$$

where K_2 is the relay stay (K_2=1, when the relay is on, and K_2=0, when the relay is off).

Since $Q^* \le 80$ % is maintained in stand-alone mode, there is no current I_B limitation.

When connected to the network (bypass)

$$I_B = \frac{P_{PV} \cdot \eta_C + P_{ga} \cdot \eta_C}{U_B},$$

where P_{ga} is the power consumed from the network when P_{PV} is not enough to provide SB charging at the specified current value, subject to the limitation specified as $I_B(Q^*)$.

The K_2 value is set by the relay element, which switches to the state: K_2=0 at $P_{PV} \cdot \eta_C \ge P_L$ and condition $Q^* \ge 80$ %; K_2=1 at $P_{PV} \cdot \eta_C < P_L$ and condition $Q^* \le 75$ %. The load is connected to the network provided that 20:00$\ge t \ge$12:00, $P_{PV} \cdot \eta_C < P_L$, $Q^* \le Q^*_d$, and also regardless of other factors at $Q^* \le 50$ %.

Simulation results in Matlab. The use of correction on the interval (t_1, t_3) is considered. Under ideal conditions for a clear day in June ($P_{PVF}(t)=P_{PVP}(t)$) and load $P_{LR1}(t)$, the value k_E=5.63. With a slight discrepancy between the values of $P_{PVF}(t)$ and $P_{PVP}(t)$ at separate time intervals (Fig. 3) and $P_{LR1}(t)$, the value k_E=4.91. In the case of load power correction (Fig. 3) k_E=5.302.

At the value $P_{PVF}(t)=0.9P_{PVP}(t)$ and $P_{LR1}(t)$ k_E=4.01. When using correction (Fig. 4) k_E=5.098. In the case when the actual generation is higher $P_{PVF}(t)>P_{PVP}(t)$, there is no special need for correction, since k_E increases, with $P_{PVF}(t)=1.15P_{PVP}(t)$ the value k_E=5.735. When using correction k_E=6.206.

At present, an experimental setup has been manufactured on the basis of the Axioma Energy ISMPPT 3000 hybrid inverter (with a built-in MPPT controller for connecting a PB and a SB charge controller) with a developed software module for power consumption control. The first tests with PB in CS3 conditions (according to weather conditions of early December) were carried out, which are planned to be continued (without waiting for summer) on an experimental setup using an electronic PB emulator.

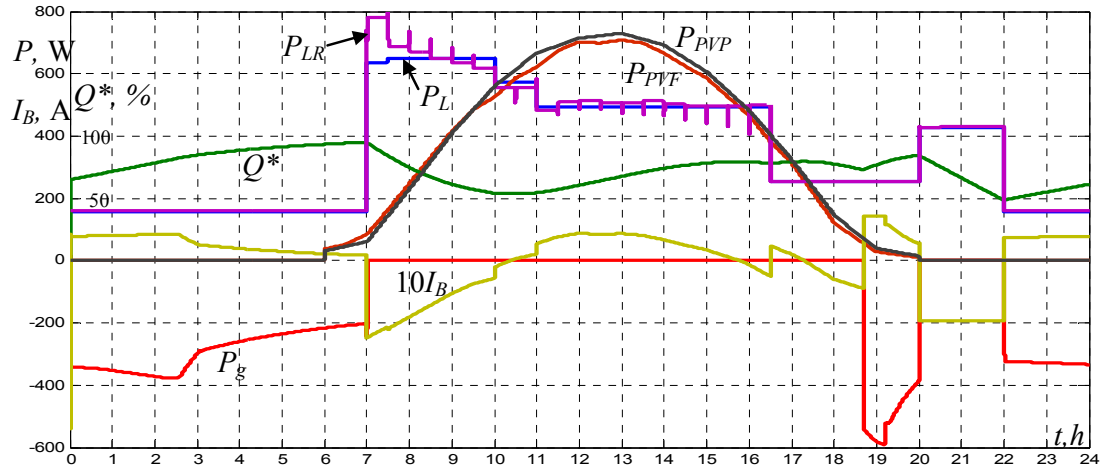

Fig. 3. Oscillograms of the 24 h cycle of the PVS operation

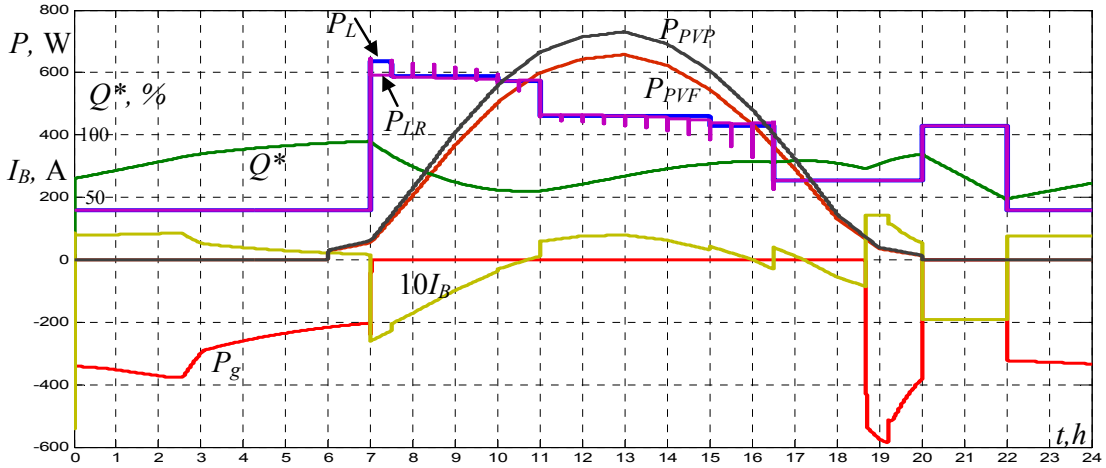

Fig. 4. Oscillograms of the 24 h cycle of the PVS operation at $P_{PVF}(t)=0.9P_{PVP}(t)$

Conclusions. The key to ensuring the efficiency of PVS is the use of software and hardware complexes that provide power consumption control, as well as recommendation functions with their correction. In this case, the subject-consumer is provided with information that allows organizing energy consumption for the day ahead while reducing the cost of paying for electricity. In the absence of a response to the recommendations, the system remains operational, eliminating the SB discharge below the set level. The approaches discussed in the article can be also used with a different schedule of tariff zones during peak hours.

The proposed solutions can be used in the development of new and modernization of existing PVS with hybrid inverters when connected to a network with multi-zone tariffication. The considered solution does not imply parallel operation of the inverter with the DN. This limits the possibilities of its application, since the load power depends on solar generation. Therefore, the further development of the work is to improve the principles of PVS implementation using a network inverter, when the load is supplied from the AVI and DN.

Conflict of interest. The authors declare that they have no conflicts of interest.

REFERENCES

1. *Pro vnesennia zmin do deiakykh zakoniv Ukrainy shchodo udoskonalennia umov pidtrymky vyrobnytstva elektrychnoi enerhii z alternatyvnykh dzherel enerhii: Zakon Ukrainy vid 21 lypnia 2020 r. № 810-IX* [On amendments to some laws of Ukraine regarding the improvement of conditions for supporting the production of electrical energy from alternative energy sources: Law of Ukraine of July 21, 2020 No. 810-IX]. Available at: https://zakon.rada.gov.ua/laws/show/810-20#Text (Accessed 15.08.2020). (Ukr).

2. Rao B.H., Selvan M.P. Prosumer participation in a transactive energy marketplace: a game-theoretic approach. *2020 IEEE International Power and Renewable Energy Conference*, Karunagappally, India, 2020, pp. 1-6. doi: https://doi.org/10.1109/iprecon49514.2020.9315274.

3. Moira L. Nicolson, Michael J. Fell, Gesche M. Huebner. Consumer demand for time of use electricity tariffs: A systematized review of the empirical evidence. *Renewable and Sustainable Energy Reviews*, December 2018, vol. 97, pp. 276-289. doi: https://doi.org/10.1016/j.rser.2018.08.040.

4. Shavelkin A., Shvedchykova I. Management of generation and redistribution electric power in grid-tied photovoltaic system of local object. *Technical electrodynamics*, 2020, no. 4, pp. 55-59. doi: https://doi.org/10.15407/techned2020.04.055.

5. El-Hendawi M., Gabbar H.A., El-Saady G., Ibrahim E.-N. A. Optimal operation and battery management in a grid-connected microgrid. Journal of International Council on Electrical Engineering, 2018, vol. 8, no. 1, 195-206. doi: https://doi.org/10.1080/22348972.2018.1528662.

6. *Hybrid Grid Inverter Growatt Hybrid 10000 HY*. Available at: https://alfa.solar/ru/gibridnyj-setevoj-invertor-growatt-hybrid-10000-hy-id494.html (Accessed 15.08.2020). (Rus).

7. *Conext SW. Hybrid Inverter*. Available at: https://www.se.com/ww/en/product-range-presentation/61645-conext-sw/ (Accessed 15.08.2020).
8. *ABB solar inverters. Product manual REACT-3.6/4.6-TL (from 3.6 to 4.6 kW)*. Available at: https://www.x-win.it/wp-content/uploads/2017/03/REACT-3.6_4.6-TL-Product-manual-EN-RevBM0000025BG.pdf (Accessed 15.08.2020).
9. Shvedchykova I.O., Kravchenko O.P., Romanchenko J.A., Kozakov E.V. Development of a database for predicting the solar generation in the software and technical complex for the management of electrical supply of the local object. *Scientific papers of Donetsk National Technical University. Series: Electrical and Power Engineering*, 2020, no. 1 (22), pp. 55-61. (Ukr). doi: https://doi.org/10.31474/2074-2630-2020-1-55-61.
10. Kaplun V., Shtepa V., Makarevych S. Neuro-network model for providing electricity generation by renewable sources in energy management system of local object. *Power Engineering: Economics, Technique, Ecology*, 2019, no. 2, pp. 27-39. (Ukr). doi: https://doi.org/10.20535/1813-5420.2.2019.190002.
11. Naderipour A., Abdul-Malek Z., Zahedi Vahid M., Mirzaei Seifabad Z., Hajivand M., Arabi-Nowdeh S. Optimal, Reliable and Cost-Effective Framework of Photovoltaic-Wind-Battery Energy System Design Considering Outage Concept Using Grey Wolf Optimizer Algorithm – Case Study for Iran. *IEEE Access*, 2019, vol. 7, pp. 182611-182623. doi: https://doi.org/10.1109/access.2019.2958964.
12. *Forecast. Solar*. Available at: https://forecast.solar/ (Accessed 15.08.2020).
13. Traore A., Taylor A., Zohdy M., Peng F. Modeling and Simulation of a Hybrid Energy Storage System for Residential Grid-Tied Solar Microgrid Systems. *Journal of Power and Energy Engineering*, 2017, vol. 5, no. 5, pp. 28-39. doi: https://doi.org/10.4236/jpee.2017.55003.
14. Barelli L., Bidini G., Bonucci F., Castellini L., Castellini S., Ottaviano A., Pelosi D., Zuccari A. Dynamic Analysis of a Hybrid Energy Storage System (H-ESS) Coupled to a Photovoltaic (PV) Plant. *Energies*, Feb. 2018, vol. 11, no. 2, p. 396. doi: https://doi.org/10.3390/en11020396.
15. Shavolkin O., Shvedchykova I., Demishonkova S. Simulation model of the photovoltaic system with a storage battery for a local object connected to a grid with multi-zone tariffication. *2020 IEEE 7th International Conference on Energy Smart Systems (ESS)*, Kyiv, Ukraine, 2020, pp. 368-372. doi: https://doi.org/10.1109/ess50319.2020.9160112.
16. Lawder M.T., Suthar B., Northrop P.W.C., De S., Hoff C.M., Leitermann O., Crow M.L., Santhanagopalan S., Subramanian V.R. Battery Energy Storage System (BESS) and Battery Management System (BMS) for Grid-Scale Applications. *Proceedings of the IEEE*, Jun. 2014, vol. 102, no. 6, pp. 1014-1030. doi: https://doi.org/10.1109/jproc.2014.2317451.
17. *DG12-100 (12V100Ah)*. Available at: https://www.ritarpower.com/products/176.html (Accessed 15.08.2020).
18. *Photovoltaic geographical information system*. Available at: https://re.jrc.ec.europa.eu/pvg_tools/en/tools.html#SA (Accessed 15.08.2020).

Received 08.11.2020
Accepted 14.02.2021
Published 05.04.2021

A.A. Shavelkin[1], *Doctor of Technical Science, Professor,*
J. Gerlici[2], *Professor, Dr. Ing.,*
I.O. Shvedchykova[1], *Doctor of Technical Science, Professor,*
K. Kravchenko[2], *PhD,*
H.V. Kruhliak[1],
[1] Kyiv National University of Technologies and Design,
2, Nemirovich-Danchenko Str., Kyiv, 01011, Ukraine,
e-mail: ishved89@gmail.com
[2] University of Žilina,
Univerzitná 8215/1, SK 01026 Žilina, Slovak Republic,
e-mail: juraj.gerlici@fstroj.uniza.sk
kateryna.kravchenko@fstroj.uniza.sk

How to cite this article:
Shavelkin A.A., Gerlici J., Shvedchykova I.O., Kravchenko K., Kruhliak H.V. Management of power consumption in a photovoltaic system with a storage battery connected to the network with multi-zone electricity pricing to supply the local facility own needs. *Electrical Engineering & Electromechanics*, 2021, no. 2, pp. 36-42. **doi: 10.20998/2074-272X.2021.2.06.**

UDC 621.3.011 **doi: 10.20998/2074-272X.2021.2.07**

Yu.M. Vasetsky

PENETRATION OF NON-UNIFORM ELECTROMAGNETIC FIELD INTO CONDUCTING BODY

The study is based on the exact analytical solution for the general conjugation problem of three-dimensional quasi-stationary field at a flat interface between dielectric and conducting media. It is determined that non-uniform electromagnetic field always decreases in depth faster than uniform field. The theoretical conclusion is confirmed by comparing the results of analytical and numerical calculations. The concept of strong skin effect is extended to the case when penetration depth is small not only compare to the characteristic body size, but also when the ratio of the penetration depth to the distance from the surface of body to the sources of the external field is small parameter. For strong skin effect in its extended interpretation, the influence of external field non-uniformity to electromagnetic field formation both at the interface between dielectric and conducting media and to the law of decrease field in conducting half-space is analyzed. It is shown, at the interface the expressions for the electric and magnetic intensities in the form of asymptotic series in addition to local field values of external sources contain their derivatives with respect to the coordinate perpendicular to the interface. The found expressions made it possible to generalize the approximate Leontovich impedance boundary condition for diffusion of non-uniform field into conducting half-space. The difference between the penetration law for the non-uniform field and the uniform one takes place in the terms of the asymptotic series proportional to the small parameter to the second power and to the second derivative with respect to the vertical coordinate from the external magnetic field intensity at the interface. References 25, figures 8.

Key words: **three-dimensional electromagnetic field, electromagnetic field formation, exact analytical solution, skin effect.**

Дослідження засноване на точному аналітичному розв'язку загальної задачі спряження тривимірного квазістаціонарного поля на межі розділу діелектричного і електропровідного середовищ. Встановлено, що неоднорідне електромагнітне поле завжди зменшується в глибині швидше, ніж однорідне. Теоретичний висновок підтверджується зіставленням результатів аналітичних і чисельних розрахунків. Поняття сильного скін-ефекту поширюється на випадок, коли глибина проникнення мала порівняно не тільки з характерними розмірами тіла, але також коли відношення глибини проникнення до відстані від поверхні тіла до джерел зовнішнього поля є малим параметром. Для сильного скін-ефекту в його розширеної інтерпретації проаналізовано вплив неоднорідності зовнішнього поля на формування електромагнітного поля на межі і на закон зменшення поля в провідному півпросторі. Показано, що на межі вирази у вигляді асимптотичних рядів крім локальних значень поля зовнішніх джерел містять їх похідні по координаті, перпендикулярної граничної поверхні. Отримані вирази дозволили узагальнити наближену імпедансну граничну умову Леонтовича для дифузії неоднорідного поля в провідний півпростір. Відмінність законів проникнення для неоднорідного і однорідного полів має місце в членах асимптотичного ряду, пропорційних малому параметру в другому ступені і другій похідній по вертикальній координаті від напруженості зовнішнього магнітного поля у граничній поверхні. Бібл. 25, рис. 8.

Ключові слова: **тривимірне електромагнітне поле, формування електромагнітного поля, точний розв'язок задачі, скін-ефект.**

Исследование основано на точном аналитическом решении общей задачи сопряжения трехмерного квазистационарного поля на границе раздела диэлектрической и проводящей сред. Установлено, что неоднородное электромагнитное поле всегда убывает по глубине быстрее, чем однородное. Теоретический вывод подтверждается сопоставлением результатов аналитических и численных расчетов. Понятие сильного скин-эффекта распространяется на случай, когда глубина проникновения мала по сравнению не только с характерными размерами тела, но также когда отношение глубины проникновения к расстоянию от поверхности тела до источников внешнего поля является малым параметром. Для сильного скин-эффекта в его расширенной интерпретации проанализировано влияние неоднородности внешнего поля на формирование электромагнитного поля на границе и на закон убывания поля в проводящем полупространстве. Показано, что на границе выражения в виде асимптотических рядов для напряженностей полей помимо локальных значений поля внешних источников содержат их производные по координате, перпендикулярной граничной поверхности. Полученные выражения позволили обобщить приближенное импедансное граничное условие Леонтовича для диффузии неоднородного поля в проводящее полупространство. Отличие законов проникновения для неоднородного и однородного полей имеет место в членах асимптотического ряда, пропорциональных малому параметру во второй степени и второй производной по вертикальной координате от напряженности внешнего магнитного поля у граничной поверхности. Библ. 25, рис. 8.

Ключевые слова: **трехмерное электромагнитное поле, формирование электромагнитного поля, точное решение задачи, скин-эффект.**

Introduction. The interaction of electromagnetic field with conducting medium is the subject of study in many technical and electrophysical applications. Examples include equipment for high frequency induction heat treatment of metals [1-3], installations for processing of metals under the action of high intensity electromagnetic field and high density currents [4-6], devices for electromagnetic forming or high-speed forming technology using pulse magnetic field [7-9]. A strong skin effect occurs in conducting elements of this equipment, in which the current and electromagnetic field are concentrated in a thin skin layer. The features of the electromagnetic field penetration into a conducting body, including its decrease in depth, depend not only on the electrical conductivity, the relative magnetic permeability of the medium and the field frequency, but also on the geometric properties of boundary surfaces and the character of the field distribution at the surface. Also, in the mentioned devices the wavelength of the

electromagnetic field is usually much larger than any characteristic dimensions of the system and the processes can be considered quasi-stationary, in which wave phenomena can be neglected.

These two circumstances determine the main limitations – it is considered the formation of a quasi-stationary electromagnetic field in systems with strong skin effect. Under the indicated limitations as it note in [10], the use of simplified approaches to the calculation of specific problems, and their use in the development of a number of numerical methods are of methodological and practical importance. Despite the long history of development, the study of the formation of electromagnetic field with strong skin effect remains an actual task.

Approximate calculation methods are often used to determine the electromagnetic field with strong skin effect. For body of infinite conductivity the penetration depth is equal to zero $\delta \to 0$, and it is sufficient to use a mathematical model in which the tangential component of the electric field intensity and the normal component of the magnetic field intensity are equal to zero at the surface of the conducting body [11, 12]. The finite penetration depth is taken into account in approximate mathematical models using the concept of the impedance boundary condition formulated by M. Leontovich [13]. It is assumed that locally the electromagnetic field penetrates into a metal body in the same way as a uniform field penetrates into a conducting half-space. The local values of the electromagnetic field at the interface correspond to the model body with perfect conductivity.

Based on the perturbation method, it became possible to calculate the fields inside and outside of conductors with a curved surface [14]. Using integral equations for curved surfaces, the solution of the problem in the second-order approximation was obtained in [15]. The expansion in a power series in a small parameter proportional to the depth of field penetration includes the Leontovich condition as a first-order approximation. The field penetration depth for such conductors dependents on the average surface curvature [16]. For curved conductors, first- and second-order corrections to the field distribution corresponding to the diffusion of uniform field into conducting half-space are found in [17].

The concept of surface impedance makes it possible to use it in modeling problems of electrodynamics, taking into account the geometric and physical properties of real boundary surfaces. Detailed results of research in this direction are given in a number of reviews. For example, in [18] the experience of many years of research on the application of the impedance approach in mathematical modeling is systematized. The article describes the types of structures for which methods of theoretical determination of the values of surface impedances are known. The generalized boundary conditions for the analytical determination of the electromagnetic field characteristics at the interface between media with two-dimensional inhomogeneities are analyzed in [19]. A comprehensive analysis of studies of the skin effect in problems of electrodynamics is presented in the book [10] where, among other things, the systematic method for constructing boundary conditions of any order based on a perturbation approach is considered, general approaches to the numerical methods application are formulated such as the boundary integral equations method, the finite element method, and the finite difference method, and also specific examples of calculations are presented.

In most of the cited papers, mathematical models of the diffusion of non-uniform electromagnetic field are limited of a small penetration depth value or insignificant field non-uniformity at the body surface. The exact solution of the problem of the diffusion of non-uniform field into conducting half-space is presented in [17] for the specific case of a field created by a thin rectilinear conductor with a current directed parallel to the interface between the media. The exact solution made it possible to justify the limitations under which the impedance boundary condition is valid for the considered non-uniform field.

In [20], we obtained a complete analytical solution to the problem of the penetration of a three-dimensional quasi-stationary electromagnetic field created by external sources in the form of current contours of arbitrary configuration located near conducting half-space. There are no restrictions on field non-uniformity in the obtained solution. For the same mathematical model, an analytical solution is found for the electromagnetic field also in the dielectric half-space [21]. The exact solution made it possible to obtain some justified results of the electromagnetic field formation. In particular, the main property is that in a conducting half-space the current density and electric field intensity do not contain components perpendicular to the boundary surface for any system of initial currents and arbitrary dependence of currents on time. In addition, in a short report, it is noted as a general property that a non-uniform electromagnetic field is decreased in a conducting medium faster than a uniform field [22]. Analytical expressions are also obtained for the field intensities at the interface between the media, consequence of which is the generalization of the Leontovich approximate impedance boundary condition to the case of penetration of a non-uniform electromagnetic field into conducting medium [23]. The cited works contain separate parts of the problem of non-uniform field penetration into a conducting medium and do not sufficiently represent the solution of the problem for an arbitrary three-dimensional quasi-stationary electromagnetic field and for any properties of the media.

The purpose of this work is to generalize the results of studying the penetration of a three-dimensional non-uniform electromagnetic field into conducting half-space, which unlike many well-known studies, is based on exact analytical solution of the problem for an external field created by sources in the form of an arbitrary system of contours with alternating currents without restrictions on the properties of the media and the field frequency. The following objectives are to achieve the aim: substantiation of the consequence that a non-uniform electromagnetic field decreases in depth always faster than an uniform field; investigation of the distribution of a non-uniform electromagnetic field at the interface between dielectric and conductive media; estimation of the influence of field non-uniformity on its distribution in the skin layer in the case of strong skin effect.

Mathematical model and analytical solution of the three-dimensional problem. The present work differs from most of the previous studies in that it is based on a complete analytical solution of the three-dimensional problem of the electromagnetic field in an enough general formulation [20, 21] and this allows to obtain a number of substantiated general consequences. Note that numerical methods, which also make it possible not to limit the penetration depth, presuppose a specific formulation of problems, and conclusions usually do not go beyond the performed calculations.

Mathematical model for a single contour with current. The analytical solution is obtained for the linear problem of conjugation at a plane interface between dielectric and conducting media of the three-dimensional quasi-stationary field. The solution satisfies Maxwell's equations and boundary conditions including the equality of the normal components of the conduction current density in a conducting medium and the displacement current density in a dielectric medium. It is based on the well-known analytical solution of the problem for an emitting current dipole near the interface. A closed contour l located in a nonconducting nonmagnetic medium with a relative dielectric permittivity ε_e, without loss of generality, was represented by a serial system of dipoles with a constant initial current $\dot{I}_0$ along the contour. A conducting body is modeled as a half-space with electrical conductivity γ and relative magnetic permeability μ, in which eddy currents are induced.

The element of the external current contour is shown in Fig. 1 as a segment of curve in the upper half-space $z > 0$. The position of the field source point on the contour M relative to the observation point Q is determined by vector $\boldsymbol{r}$. The axis z is oriented perpendicular to the interface surface in the direction of the single vector $\boldsymbol{e}_z$. For an arbitrary spatial contour, the unit tangent vector to the contour $\boldsymbol{t} = \boldsymbol{t}_{\parallel} + \boldsymbol{t}_{\perp}$ has nonzero projections onto the vertical direction $\boldsymbol{t}_{\perp} = (\boldsymbol{t}\cdot\boldsymbol{e}_z)\boldsymbol{e}_z$ and onto the interface between the media $\boldsymbol{t}_{\parallel} = \boldsymbol{t} - (\boldsymbol{t}\cdot\boldsymbol{e}_z)\boldsymbol{e}_z$.

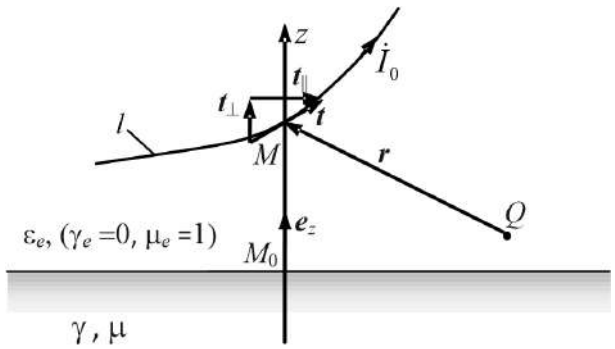

Fig. 1. Element of arbitrary spatial contour l with current $\dot{I}_0$ located near conducting half-space

For the system under consideration all characteristics of the electromagnetic field in conducting and dielectric media are found in the form of expressions for the complex-value amplitudes of the vector and scalar potentials, the intensities of the electric and magnetic fields. (Complex-value amplitudes we will mark with a dot over the corresponding symbols). Since the linear problem is considered, it can easily be extended to the general case of an arbitrary external field created by the corresponding system of current contours and to an arbitrary dependence of currents on time $I_0(t)$ using the Fourier transform.

Electromagnetic field in conducting half-space. The expression for electric intensity in conducting half-space at point $Q(\rho,\theta,z)$ is the following [20]

$$\dot{\boldsymbol{E}}_i = -\frac{\mu_0 \dot{I}_0}{4\pi} 2i\omega \oint_l \left[\boldsymbol{t}_{\parallel} T_1(\rho,\theta,z) + (\boldsymbol{t}\cdot\boldsymbol{e}_z)\boldsymbol{e}_\rho T_2(\rho,\theta,z)\right] dl \,, \quad (1)$$

where ω is cyclic frequency, i is imaginary unit, μ_0 is permeability of vacuum. Here the local cylindrical coordinates (ρ,θ,z) with its unit basis vectors $(\boldsymbol{e}_\rho, \boldsymbol{e}_\theta, \boldsymbol{e}_z)$ are used (Fig. 2). The center of the coordinate system is located at point M_0 intersection of the vertical axis with the interface. The angle θ is defined relative to the axis directed along the unit vector $\boldsymbol{e}_{\parallel} = \boldsymbol{t}_{\parallel}/|\boldsymbol{t}_{\parallel}|$. The values of local coordinates depend on the position of the source point M during integration along the contour.

The functions $T_1(\rho,\theta,z)$ and $T_2(\rho,\theta,z)$ in (1) are as follows

$$T_1(\rho,\theta,z) = \int_0^\infty \exp(qz)\frac{\exp(-\vartheta z_M)J_0(\vartheta\rho)}{w(\vartheta)}\vartheta d\vartheta \,,$$
$$T_2(\rho,\theta,z) = \int_0^\infty \exp(qz)\frac{\exp(-\vartheta z_M)J_1(\vartheta\rho)}{w(\vartheta)}\vartheta d\vartheta \,, \quad (2)$$

where $q = \sqrt{\vartheta^2 + p^2}$, $p = \sqrt{i\omega\mu\mu_0\gamma}$ is propagation constant, $w(\vartheta) = \vartheta + q/\mu$, $J_0(\cdot)$ and $J_1(\cdot)$ are Bessel functions of the first kind of zero and first orders. Since the decrease of the field with respect to depth is considered, the functions that depend on the coordinate z are distinguished by a separate factor in (2).

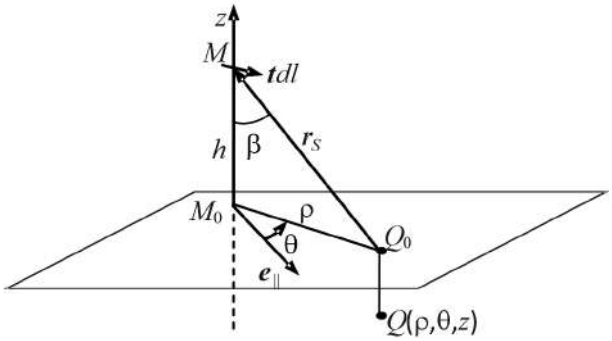

Fig. 2. Geometric parameters for determining the values of the electromagnetic field intensities at the point $Q(\rho,\theta,z)$ in conducting half-space $z < 0$

The expression for the magnetic field intensity $\dot{\boldsymbol{H}}_i$ in conducting half-space follows from the Maxwell equation $\nabla\times\dot{\boldsymbol{E}} = -i\omega\mu\mu_0\dot{\boldsymbol{H}}$

$$\dot{\boldsymbol{H}}_i = \frac{\mu_0\dot{I}_0}{4\pi\mu}\oint_l \left[\boldsymbol{t}_{\parallel}\left[\boldsymbol{e}_z \sin\theta\frac{\partial T_1}{\partial\rho} + [\boldsymbol{e}_{\parallel}\times\boldsymbol{e}_z]\frac{\partial T_1}{\partial z}\right] - (\boldsymbol{t}\cdot\boldsymbol{e}_z)\boldsymbol{e}_\theta\frac{\partial T_2}{\partial z}\right] dl \,. \quad (3)$$

As follows from (1), the projection of the electric field intensity to the direction perpendicular to the plane interface between the media is always equal to zero $\dot{\boldsymbol{E}}_i\cdot\boldsymbol{e}_z = 0$. On the other hand, in this medium all

components of the magnetic field intensity in the general case can have nonzero values.

To study other general features of the electromagnetic field formation associated with the penetration of non-uniform field into conducting half-space, it is advisable to introduce dimensionless parameters, whose values are due to the form of expressions (2). In this case, we use dimensionless integration variable $\chi = \vartheta\mu/\sqrt{\omega\mu\mu_0\gamma}$ and take into account that $pz = \sqrt{2i}\,\frac{z}{\delta}$, where $\delta = 1/\mathrm{Re}(p) = \sqrt{2/(\omega\mu\mu_0\gamma)}$ is the penetration depth of a uniform field into conducting half-space [24]. As a result, the functions $T_1(\rho,\theta,z) = \frac{p}{\mu} f_1\left(\frac{z}{\delta},\varepsilon,\beta\right)$ and $T_2(\rho,\theta,z) = \frac{p}{\mu} f_2\left(\frac{z}{\delta},\varepsilon,\beta\right)$ will be expressed in terms of dimensionless parameters where

$$f_1\left(\frac{z}{\delta},\varepsilon,\beta\right) = \int_0^\infty K\left(\frac{z}{\delta},\chi\right)\cdot\frac{\exp\left(-\frac{\chi\cos\beta}{\varepsilon}\right)J_0\left(\frac{\chi\sin\beta}{\varepsilon}\right)}{w_1(\chi)}\chi d\chi, \quad (4)$$

$$f_2\left(\frac{z}{\delta},\varepsilon,\beta\right) = \int_0^\infty K\left(\frac{z}{\delta},\chi\right)\cdot\frac{\exp\left(-\frac{\chi\cos\beta}{\varepsilon}\right)J_1\left(\frac{\chi\sin\beta}{\varepsilon}\right)}{w_1(\chi)}\chi d\chi,$$

$$K\left(\frac{z}{\delta},\chi\right) = \exp(qz) = \exp\left(\sqrt{2i}\,\frac{z}{\delta}\sqrt{1+\left(\frac{\chi}{\mu\sqrt{i}}\right)^2}\right), \quad (5)$$

here the parameter $\varepsilon = \mu\delta/\sqrt{2}r_S$ is proportional to the ratio of the penetration depth δ to the distance r_S from the field source at a point M on the contour to the body surface at a point Q_0 (Fig 2). The denominator $w_1(\chi)$ in the integrands (4) is written as

$$w_1(\chi) = \frac{\chi}{\sqrt{i}} + \sqrt{1+\left(\frac{\chi}{\mu\sqrt{i}}\right)^2}. \quad (6)$$

Expressions (1) and (3) describe the penetration of the electromagnetic field of arbitrary contour with current into conducting half-space and in the general case they differ from approximate description of the penetration of uniform field. Both the values of the intensity of the electric and magnetic fields on the boundary surface $z = 0$, and the law of their decrease depending on the coordinate z are differed. Usually, in approximate models, the initial value is the tangential component of the magnetic field intensity $\dot{\boldsymbol{H}}_\tau$ at the boundary, the local value of which for a body of arbitrary shape is found from the solution of the external problem under the assumption of the perfect skin effect $\delta\to 0$ [11]. The local value on the body surface $\dot{\boldsymbol{H}}_\tau$ is taken as the value of the uniform field. Its penetration into conducting half-space is described by the known distribution of the electric $\dot{\boldsymbol{E}}_i$ and magnetic $\dot{\boldsymbol{H}}_i$ intensities: $\dot{\boldsymbol{E}}_i = \dot{\boldsymbol{E}}_\tau e^{-pz}$, $\dot{\boldsymbol{H}}_i = \dot{\boldsymbol{H}}_\tau e^{-pz}$ [24]. The field vectors are related by the Leontovich approximate impedance boundary condition $\dot{\boldsymbol{E}}_\tau = \varsigma\left[\boldsymbol{e}_z\times\dot{\boldsymbol{H}}_\tau\right]$, where the surface impedance $\varsigma = \sqrt{i\omega\mu\mu_0\gamma}/\gamma$ in this case connects the values of the field vectors not only at the interface between dielectric and conducting media $\dot{\boldsymbol{E}}_\tau$, $\dot{\boldsymbol{H}}_\tau$, but also in the entire conducting half-space $\dot{\boldsymbol{E}}_i$, $\dot{\boldsymbol{H}}_i$. In the general case of non-uniform electromagnetic field penetration, expressions (1) and (3) show the difference both from the values of the electric $\dot{\boldsymbol{E}}_\tau$ and magnetic $\dot{\boldsymbol{H}}_\tau$ intensities at the boundary surface with perfect skin effect, and the law of their decrease depending on the coordinate z.

Electromagnetic field in dielectric half-space. The expressions for electric $\dot{\boldsymbol{E}}_e$ and magnetic $\dot{\boldsymbol{H}}_e$ intensities in dielectric half-space where the current contour is located are determined by single function G_e [21]

$$\dot{\boldsymbol{E}}_e = \dot{\boldsymbol{E}}_{e1} + \dot{\boldsymbol{E}}_{e2} + \dot{\boldsymbol{E}}_{e3} = -i\omega\frac{\mu_0\dot{I}_0}{4\pi}\oint_l\left(\frac{\boldsymbol{t}}{r} - \frac{\boldsymbol{t}_1}{r_1} - \boldsymbol{e}_z\times\left[\boldsymbol{t}_1\times\nabla G_e\right]\right)dl, \quad (7)$$

$$\dot{\boldsymbol{H}}_e = \dot{\boldsymbol{H}}_{e1} + \dot{\boldsymbol{H}}_{e2} + \dot{\boldsymbol{H}}_{e3} = -\frac{\dot{I}_0}{4\pi}\oint_l\left[\frac{\boldsymbol{t}\times\boldsymbol{r}}{r^3} - \frac{\boldsymbol{t}_1\times\boldsymbol{r}_1}{r_1^3} - \boldsymbol{t}_1\times\nabla\left(\frac{\partial G_e}{\partial z}\right)\right]dl, \quad (8)$$

where function G_e using dimensionless values are determined by following improper integral

$$G_e = \frac{2}{\sqrt{i}}\int_0^\infty\frac{\exp\left(-\frac{\chi\cos\beta_1}{\varepsilon_1}\right)J_0\left(\frac{\chi\sin\beta_1}{\varepsilon_1}\right)}{w_1(\chi)}d\chi. \quad (9)$$

The geometric quantities included in expressions (7) – (9) are shown in Fig. 3. The elements $\boldsymbol{t}dl$ of the initial contour and $\boldsymbol{t}_1 dl$ of the mirror reflection contour relative to the interface are located at the points M and M_1 respectively. Projections of tangent vectors onto the vertical axis are equal in absolute value and opposite in their direction ($\boldsymbol{t}_{1z} = -\boldsymbol{t}_z$), and the projections $\boldsymbol{t}_\parallel$ and $\boldsymbol{t}_{1\parallel}$ onto the plane of interface between media are equal in their lengths and directions $\boldsymbol{t}_{1\parallel} = \boldsymbol{t}_\parallel$, i.e. $\boldsymbol{t} = \boldsymbol{t}_\parallel + \boldsymbol{t}_z$, $\boldsymbol{t}_1 = \boldsymbol{t}_{1\parallel} + \boldsymbol{t}_{1z} = \boldsymbol{t}_\parallel - \boldsymbol{t}_z$. Vectors $\boldsymbol{r} = (z_M - z)\boldsymbol{e}_z + \boldsymbol{\rho}$ and $\boldsymbol{r}_1 = (z_{M1} - z)\boldsymbol{e}_z + \boldsymbol{\rho} = -(z_M + z)\boldsymbol{e}_z + \boldsymbol{\rho}$ (the vector $\boldsymbol{\rho}$ is the projection of vector $\boldsymbol{r}$ or vector $\boldsymbol{r}_1$ onto interface) determine positions of points M and M_1 relative to the observation point Q. The angle β_1 shows the orientation of the vector $\boldsymbol{r}_1$ relative to the vertical axis. The parameter $\varepsilon_1 = \mu\delta/\left(\sqrt{2}r_1\right)$ is connected with distance r_1 between points M_1 and Q.

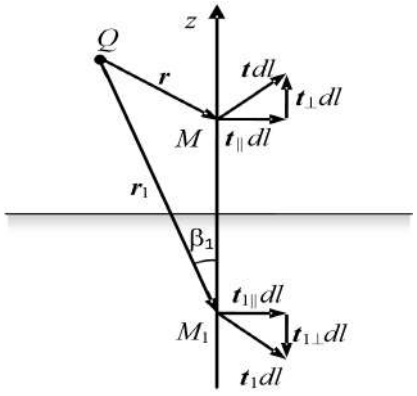

Fig. 3. Location the contour element $\boldsymbol{t}dl$ and its mirror reflection $\boldsymbol{t}_1 dl$ relative to the observation point Q

The first and second terms in (7) and (8) describe the solution of the problem for perfect skin-effect when $\delta \to 0$ [20]. At a value of the penetration depth other than zero the impact of electro-physical properties of the medium is taken into account by the third term.

The electromagnetic field (7) and (8) at an arbitrary point of the dielectric half-space is created by all sources, including the current of the initial contour, eddy currents in conducting medium, sources of magnetization of the medium and electric charges at the interface between the media. We can say that this total field decreases from the value at the interface during its diffusion into conducting body. The presence of the third term in (7) and (8) determines the difference between the tangential components of the field intensities on the surface from their values $\dot{\boldsymbol{E}}_\tau$, $\dot{\boldsymbol{H}}_\tau$, which correspond to the field in the approximate model of the perfect skin effect.

General feature of decrease of non-uniform electromagnetic field in the conducting half-space. The availability of the exact solution to the general problem allows, first of all, to analyze the features of the penetration of non-uniform field into a conducting half-space without restrictions on the values of the electro-physical parameters and the field frequency.

As it follows from (2) and (4), the distribution of any component of the electric and magnetic field intensities in the skin-layer, depending on the coordinate z, is associated with exponential function $K(z/\delta,\chi)$ (5) in the integrands. The factor $\sqrt{1+\left[\chi/\left(\mu\sqrt{i}\right)\right]^2}$ in the exponent affects to the field decrease law. If the influence of the second term $\left[\chi/\left(\mu\sqrt{i}\right)\right]^2$ is absent, it corresponds to the decrease law of the uniform field. Since $\mathrm{Re}\left(\sqrt{1+\left[\chi/\left(\mu\sqrt{i}\right)\right]^2}\right)>1$, the decrease of the non-uniform electromagnetic field created by the current contour is always faster than that of the uniform field. Taking into account the principle of superposition, this conclusion will be valid for any system of initial closed contours and therefore is valid in the general case of arbitrary external field.

Thus, faster decrease of non-uniform electromagnetic field as compared to uniform field is general feature of the electromagnetic field formation at its diffusion into conducting half-space. A qualitative explanation of the found feature can be based on the analysis of the inhomogeneous field formation under the action of «standard» external sources and it is the subject of additional research.

Let us consider the influence of the parameter ε on the field penetration law, that is, the effect of the distance between the external field sources and the body surface in comparison with the penetration depth (at $\mu = 1$). The parameter ε also characterizes the field non-uniformity, since the closer the current contour is to the surface, the more non-uniform field is at its surface. This is reflected in the influence of the parameter ε on the dependences of the functions $f_1(z/\delta,\varepsilon,\beta)$ and $f_2(z/\delta,\varepsilon,\beta)$ with respect to coordinate z in (4).

Let, for example, the sources of the external field are remote at a considerable distance from the surface of a conducting body and, accordingly, for all points of the contour $\varepsilon<<1$. In this case, in (4), due to the presence of the exponential function $\exp(-\chi\cos\beta/\varepsilon)$, the value of the integrands turns out to be insignificant when $\chi\cos\beta > \varepsilon$. That is, the value of improper integrals (4) at small values ε is mainly determined by the behavior of the integrand near the lower limit of integration $\chi = 0$. This means that when integrating in (4), the influence of the factor $\sqrt{1+\left[\chi/\left(\mu\sqrt{i}\right)\right]^2}$ will slightly differ from the case when this factor is equal to one. Therefore, if $\varepsilon<<1$, then the decrease in the field from its local value on the surface at the point Q_0 will be close to the decrease in the uniform field.

If the parameter ε is not small the influence of the factor $\sqrt{1+\left[\chi/\left(\mu\sqrt{i}\right)\right]^2}$ is much more. In this case, the elements of the contour as a source of the external field are located closer to the interface between the media and the decrease of the electromagnetic field will occur according to a different law with larger decrease rate in depth.

A specific example when the penetration depth $\delta=\sqrt{2/(\omega\mu\mu_0\gamma)}$ is comparable to the dimensions of the contour illustrates the general conclusion of three-dimensional field decrease. An additional argument for the validity of the conclusion can also be a comparison of the results of calculating the decrease of non-uniform electromagnetic field, performed using the obtained analytical expressions and using the numerical method in the Comsol package [22].

The calculation was performed for a circular contour located in a plane perpendicular to flat interface, as shown in Fig. 4. The radius of the contour is R = 0,05 m, the minimum distance from the contour to the interface is h_0 = 0,02 m, the electrophysical properties of the medium are as follows: μ = 1, $\gamma = 10^5$ 1/(Ω·m). In contrast to the analytical method, in the numerical calculation, the current contour was selected in the form of a conductor with a square cross-section $2r\times2r$ at r = 0,004 m. In the numerical calculation, the problem was solved in a limited area, the dimensions of which significantly exceed the contour radius. Different values of the field penetration depth and, accordingly, the values of the ratio δ/R or $\varepsilon_m=\max(\varepsilon)=\mu\delta/\sqrt{2}h_0$ are obtained by choosing the field frequency.

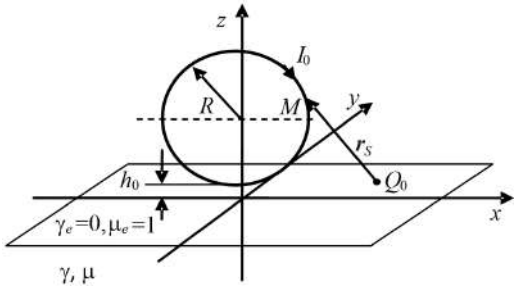

Fig. 4. Electromagnetic system with a circular current contour located in the plane perpendicular to the interface

The results of calculating the electric and magnetic field intensities are shown in Fig. 5,*a-c*. In the upper group of figures, arrows show the distribution of the induced current density $\boldsymbol{j}_i = \gamma \boldsymbol{E}_i$ in the vertical plane passing through the center of the circular contour. The results of these calculations, performed by the numerical method, confirm the theoretical conclusion about the zero value of the vertical components of the electric field intensity and current density. The curves in the figures below show the change with depth for component of the amplitude of the electric field intensity, normalized to the value of the field at the surface $E_x^* = \left|\dot{E}_x\right| / \left|\dot{E}_x(z=0)\right|$. The coordinate value in conducting medium is normalized to the value of the field penetration depth. The dotted lines show the decrease of the uniform field. Solid lines correspond to analytical calculations, individual points marked with squares correspond to the results of numerical calculations. The bottom row of figures shows dependences for different components of the magnetic field intensity, also normalized to the amplitude values of the corresponding field components at the surface of the conductive medium $H_k^* = \left|\dot{H}_{ik}\right| / \left|\dot{H}_{ik}(z=0)\right|$, where $k = x, y, z$.

Note, in contrast to the electric field, the vertical component of the magnetic field intensity in conducting half-space in this case of a three-dimensional field is not equal to zero.

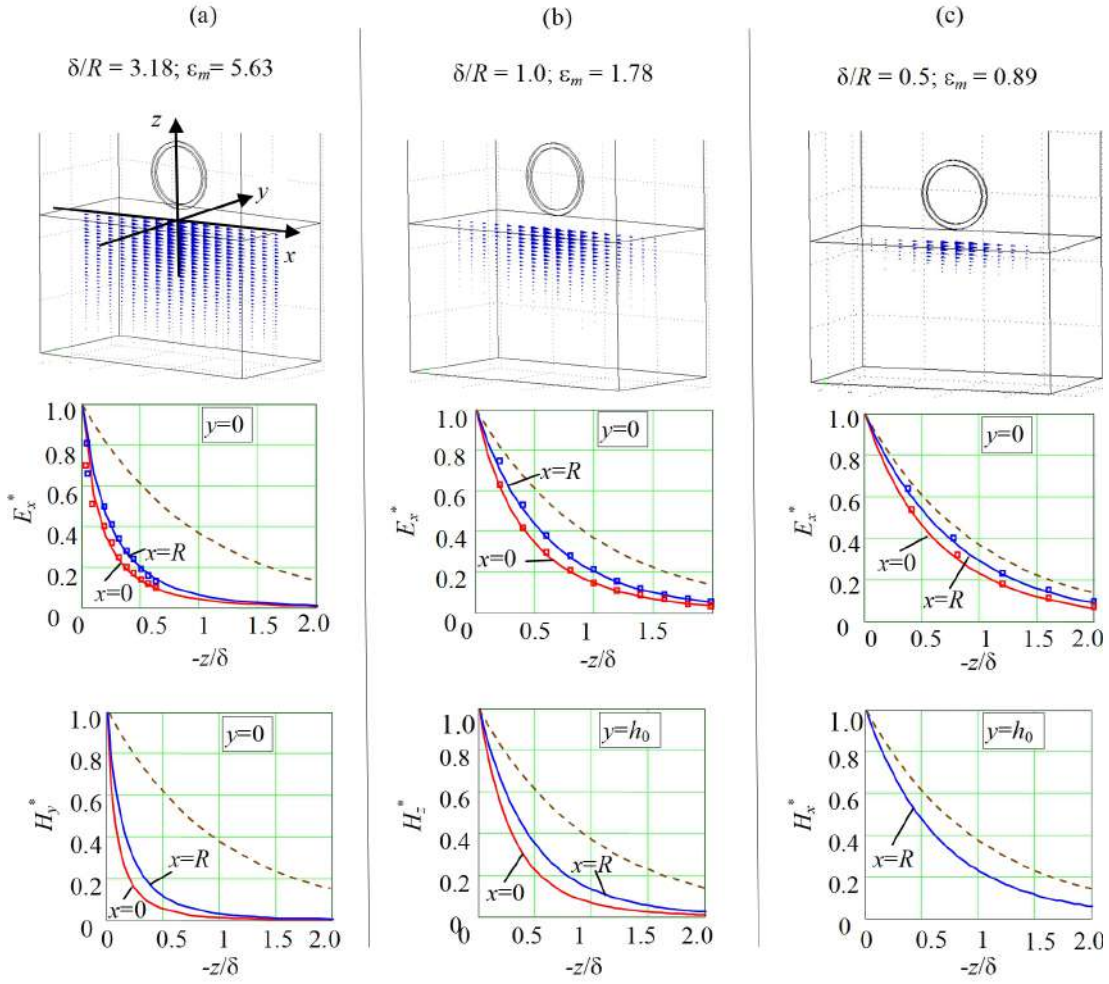

Fig. 5. Depth distribution of the normalized amplitudes for the components of the electric E_x^* and magnetic H_x^*, H_y^*, H_z^* intensities in conducting half-space for non-uniform three-dimensional field created by the specific system in the form of circular current contour near the flat interface between media

It is seen that with a decrease in the penetration depth δ in comparison with the radius of the contour R or with the distance h_0, the penetration law both electric and magnetic fields approaches the slowest decrease of uniform field. Immediately below the contour at $x = 0$, $y = 0$, where the contour section most closely approaches to the interface, decrease is more pronounced than at $x = R$. This is explained by the fact that at $x = R$, the contour sections are at greater distance from the surface, and therefore the non-uniformity of the external field distribution near the surface is less than in the case when $x = 0$.

Dashed curve in Fig. 5,*b* for vertical component of magnetic field has a conditional meaning, since in the approximate model of the diffusion of uniform field the component of the magnetic field intensity normal to the surface is equal to zero. However, for diffusion of a three-dimensional non-uniform field, this component is nonzero.

For the considered system on the plane $x = 0$, the field component $\dot{H}_x$ is equal to zero, and therefore in Fig. 5,*c* the corresponding curve is missing.

Penetration of non-uniform electromagnetic field in the case of strong skin effect. The general feature of faster decay of non-uniform field in comparison with uniform one is the basis for analyzing the decrease of the field, when introduced parameter is small $\varepsilon < 1$ and not necessarily going to zero. This parameter depends on the position of the source point M on the contour. This section deals with arbitrary electromagnetic systems for which the maximum value $\varepsilon_m = \max(\varepsilon)$ of all ε is a small parameter.

Comparison of decay of non-uniform and uniform fields. To confirm that the penetration law of non-uniform field is approached the exponential decrease of uniform field, let us compare the functions $f_1(z/\delta,\varepsilon,\beta)$ and $f_2(z/\delta,\varepsilon,\beta)$ in (4), taking into account the factor $\sqrt{1+\left[\chi/\left(\mu\sqrt{i}\right)\right]^2}$ in the exponent with the same functions $f_{10}(z/\delta,\varepsilon,\beta)$ and $f_{20}(z/\delta,\varepsilon,\beta)$, but provided that the factor is taken to be equal to one, which corresponds to decrease of uniform field. For the electric field intensity, these functions are related to the directions of the current parallel and perpendicular to the interface. For the magnetic field intensity, the corresponding functions that follow from (3) can be similarly considered.

Let us first consider changes in functions $f_1(0,\varepsilon,\beta)$ and $f_2(0,\varepsilon,\beta)$ at the surface ($z = 0$). The dependences of the modules of these functions on the value $\rho/h = \tan\beta$ at $\mu = 1$ and various values of the small parameter $\varepsilon < 1$ are shown in Fig. 6.

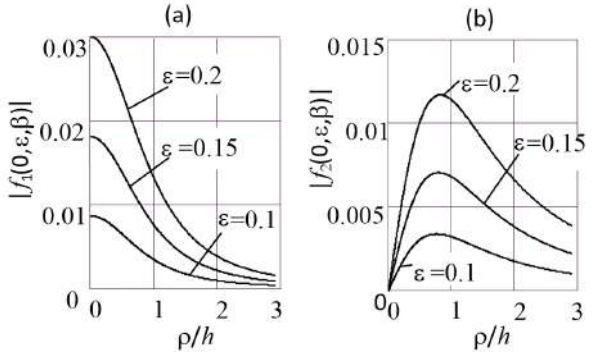

Fig. 6. Changes in the functions $|f_1(0,\varepsilon,\beta)|$ and $|f_2(0,\varepsilon,\beta)|$ at the interface depending on the relative distance $\rho/h = \tan\beta$ for small values of the parameter $\varepsilon < 1$ and $\mu = 1$

It can be seen that sections with different directions of the current are involved in different ways in the creation of the tangential component of the electric field intensity on the body surface. The horizontal component of the current gives the largest value of integrand in (1) just below the current element. The largest value from the vertical component of the current is realized at a certain distance from the point M_0 in the radial direction at a distance ρ approximately equal to the height at which the contour element is located.

The curves in Fig. 7,*a* show values of the modules of functions dependents on the depth for direction of the current parallel to the interface at $\mu = 1$: solid lines correspond to the function $|f_1(z/\delta,\varepsilon,\beta|$, dashed lines correspond to the function $|f_{10}(z/\delta,\varepsilon,\beta|$. The results are given for the case $\beta = 0$ where the function $|f_1(0,\varepsilon,\beta|$ at the surface takes the largest values. The curves for different values of the small parameter ε are obtained by choosing the corresponding values of the height h above the surface on which the contour element is located. A comparison confirms the statement about the insignificant influence of the functional dependence of the integration variable in the exponential function. The quantitative values of the deviation that arise when the factor $\sqrt{1+\left[\chi/\left(\mu\sqrt{i}\right)\right]^2}$ is replaced by one are shown in Fig. 7,*b* in the form of a relative deviation value $\Delta_1 = ||f_1| - |f_{10}||/|f_1|$.

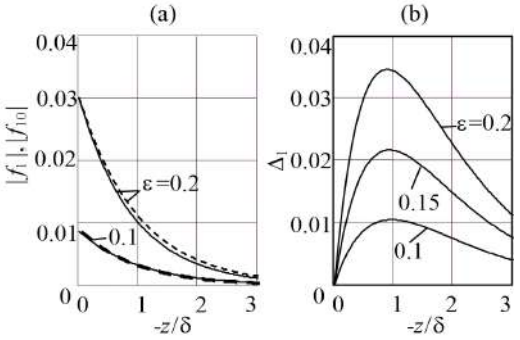

Fig. 7. Comparison of the decrease of non-uniform and uniform fields for functions f_1 and f_{10} corresponding to the direction of the current parallel to the interface between media for the small value of the parameter $\varepsilon < 1$ and $\mu = 1$

Similar results are also valid for the term of the integrand in the contour integral (1) related to the vertical direction of the current. Comparative values of functions $f_2(z/\delta,\varepsilon,\beta)$, $f_{20}(z/\delta,\varepsilon,\beta)$ and the values of their relative deviation $\Delta_2 = ||f_2| - |f_{20}||/|f_2|$ are shown in Fig. 8. In this case, the observation point is selected near the maximum value of the function $|f_2(0,\varepsilon,\beta)|$ at the interface at $\rho = h$, ($\beta = \pi/4$).

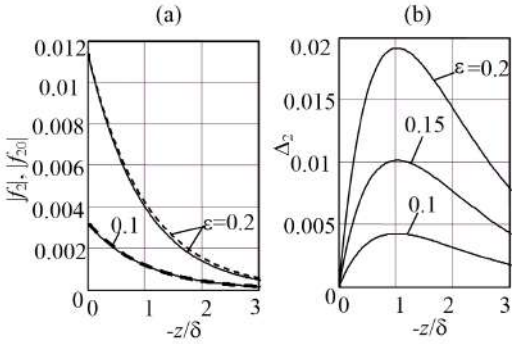

Fig. 8. Comparison of the decrease of non-uniform and uniform fields for functions f_2 and f_{20} corresponding to the direction of the current perpendicular to the interface for the small value of the parameter $\varepsilon < 1$ and $\mu = 1$

From the presented calculations, it can be seen that with decrease in the value of the small parameter ε, the error from replacing the factor in the exponential by one rapidly decreases, approximately inversely proportional to the ε^2. Similar results turn out to be valid for the magnetic field intensity.

The following conclusion can be made from this. With a strong skin effect, when the maximum value of the introduced parameter ε_m is small, the electromagnetic field decrease from the local value on the surface, approximately according to the penetration law of

uniform field. Since the penetration law depends on the value of the parameter ε_m, the concept of strong skin effect can be extended from the point of view of the possibility of using the penetration law of uniform field. The skin effect can be considered strong when the product of the relative magnetic permeability and the penetration depth $\mu\delta$ is small not only with respect to the characteristic dimensions of conducting body, but also of the entire electromagnetic system, including the distance from the surface of body to the external sources.

Taking into account the boundary conditions ($z=0: \dot{\boldsymbol{E}}_{e\|}=\dot{\boldsymbol{E}}_{i\|}, \dot{\boldsymbol{H}}_{e\|}=\dot{\boldsymbol{H}}_{i\|}, \dot{\boldsymbol{H}}_{e\perp}/\mu=\dot{\boldsymbol{H}}_{i\perp}$) and the expressions for the field intensities in the dielectric half-space (7) – (9), the approximate expressions in the conducting half-space take the following form

$$\dot{\boldsymbol{E}}_i \approx e^{pz}\dot{\boldsymbol{E}}_i(z=0)=e^{pz}\dot{\boldsymbol{E}}_{e\|}(z=0)= e^{pz}i\omega\frac{\mu_0\dot{I}_0}{4\pi}\oint_l \boldsymbol{e}_z\times\left[\boldsymbol{t}_1\times\nabla G_e\big|_{z=0}\right]dl, \quad (10)$$

$$\dot{\boldsymbol{H}}_i \approx e^{pz}\dot{\boldsymbol{H}}_i(z=0)=e^{pz}\left[\dot{\boldsymbol{H}}_{e\|}(z=0)+\dot{\boldsymbol{H}}_{e\perp}(z=0)/\mu\right], \quad (11)$$

where the components of the magnetic field intensities at the dielectric surface are as follows

$$\dot{\boldsymbol{H}}_{e\|}(z=0)=\dot{\boldsymbol{H}}_{e1}(z=0)+\dot{\boldsymbol{H}}_{e2}(z=0)+ \frac{\dot{I}_0}{4\pi}\oint_l\left\{\left[\boldsymbol{t}_\|\times\boldsymbol{e}_z\right]\frac{\partial^2 G_e}{\partial z^2}-\boldsymbol{t}_\perp\times\nabla\left(\frac{\partial G_e}{\partial z}\right)\right\}\Bigg|_{z=0}dl, \quad (12)$$

$$\dot{\boldsymbol{H}}_{e\perp}(z=0)=\frac{\dot{I}_0}{4\pi}\oint_l \boldsymbol{t}_\|\times\left\{\nabla\left(\frac{\partial G_e}{\partial z}\right)-\frac{\partial^2 G_e}{\partial z^2}\boldsymbol{e}_z\right\}\Bigg|_{z=0}dl.$$

The expressions (10) – (12) presented as two factors are approximate only in relation to the dependence on the coordinate z. On the surface at $z = 0$, they take into account the non-uniformity of the electromagnetic field and give the values of the field intensities without restrictions on the value of the parameter $\varepsilon = \varepsilon_1$.

The next two questions are related to the introduced extended concept of the strong skin effect. First, what is the difference at the interface between the intensities of the non-uniform field $\dot{\boldsymbol{E}}_i(z=0)$ and $\dot{\boldsymbol{H}}_i(z=0)$ in (10) – (12) from the values of the tangent components $\dot{\boldsymbol{E}}_\tau$ and $\dot{\boldsymbol{H}}_\tau$ for the model of the perfect skin effect. Second, what is the error of replacing the penetration law of non-uniform field with the penetration law of uniform one, depending on the value of the small parameter.

Non-uniform electromagnetic field at the interface between media. For small values ε_1, at an arbitrary point of the dielectric half-space, including at the interface between the media the expressions (10) and (11) can be simplified. In this case the function G_e can be represented by an asymptotic series, limited by a certain number of terms N [25]

$$G_e \approx \sum_{n=0}^{N}G_n=\sum_{n=0}^{N}\frac{2}{\sqrt{i}}a_n(\mu)\int_0^\infty\left(\frac{\chi}{\sqrt{i}}\right)^n\exp\left(-\frac{\chi\cos\beta_1}{\varepsilon_1}\right)J_0\left(\frac{\chi\sin\beta_1}{\varepsilon_1}\right)d\chi= \quad (13)$$

$$=\sum_{n=0}^{N}2(-1)^n a_n(\mu)\left(\frac{\varepsilon_1}{\sqrt{i}}\right)^{n+1}r_1^{n+1}\frac{\partial^{(n)}}{\partial z^n}\left(\frac{1}{r_1}\right),$$

where $a_n(\mu)$ are the Taylor series coefficients of the function $1/w_1=\sum_{n=0}^{\infty}a_n(\mu)\left(\chi/\sqrt{i}\right)^n$.

The use of asymptotic expansion (13) for field intensities (1), (3) or (7), (8) on the surface made it possible to find approximate values of the field at the boundary and to establish some general features of the field formation. Finding the corresponding relations is given in [23].

Firstly, in the found analytical expressions, the electromagnetic field on the surface is determined only by the known distribution of the field of external sources at the boundary

$$\dot{\boldsymbol{E}}_\|(z=0)=\sum_{n=0}^{N}\dot{\boldsymbol{E}}_{\|\,n}=\varsigma\sum_{n=0}^{N}2a_n(\mu)\left(\frac{\mu}{p}\right)^n\left\{\frac{\partial^{(n)}}{\partial z^n}\boldsymbol{e}_z\times\dot{\boldsymbol{H}}_{0\|}\right\}\Bigg|_{z=0}; \quad (14)$$

$$\dot{\boldsymbol{H}}_\|(z=0)=\sum_{n=0}^{N+1}\dot{\boldsymbol{H}}_{\|\,n}=-\sum_{n=0}^{N+1}2a_{n-1}(\mu)\left(\frac{\mu}{p}\right)^n\left\{\frac{\partial^{(n)}\dot{\boldsymbol{H}}_{0\|}}{\partial z^n}\right\}\Bigg|_{z=0}; \quad (15)$$

$$\dot{\boldsymbol{H}}_{i\perp}(z=0)=\sum_{n=0}^{N}\dot{\boldsymbol{H}}_{i\perp n}=-\sum_{n=0}^{N}2\frac{a_n(\mu)}{\mu}\left(\frac{\mu}{p}\right)^{n+1}\left\{\frac{\partial^{(n+1)}\dot{\boldsymbol{H}}_{0\perp}}{\partial z^{n+1}}\right\}\Bigg|_{z=0}, \quad (16)$$

here, it is taken into account $\varepsilon_1 r_1/\sqrt{i}=\mu/p$; it is accepted $a_{-1} = –1$; $\dot{\boldsymbol{H}}_0$ is the magnetic field intensity of external sources in dielectric medium at the interface. If the external field is created by a single current contour, then

$$\dot{\boldsymbol{H}}_0=-\frac{\dot{I}_0}{4\pi}\oint_l\frac{\boldsymbol{t}\times\boldsymbol{r}}{r^3}dl. \quad (17)$$

From (14) – (16) it can be seen that the electromagnetic field is determined not only by its local value on the surface, which corresponds to $n = 0$. It also depends on the derivatives of the field with respect to the coordinate, that is, on the non-uniformity of the external field at the interface between the media. In this respect, the electromagnetic field at the boundary differs from the values $\dot{\boldsymbol{E}}_\tau$ and $\dot{\boldsymbol{H}}_\tau$ in the perfect skin effect model. The difference is associated with the field of eddy currents in conducting medium, the distribution law of which depends on the degree of remoteness of the external field sources in comparison with the penetration depth. The component of the magnetic field intensity normal to the boundary, which is absent in the perfect model, is determined only by the derivatives with respect to the coordinate z of the same external field component.

Secondly, the found expressions (14) – (16) made it possible to generalize the Leontovich impedance boundary condition for the case of diffusion of non-uniform electromagnetic field into conducting medium. The impedance boundary condition, which establishes the relation between the tangential components of the electric and magnetic field intensities at the interface, for individual terms of the asymptotic series is the following

$$a_{n-1}(\mu)\dot{\boldsymbol{E}}_{\|\,n}=-a_n(\mu)\varsigma\boldsymbol{e}_z\times\dot{\boldsymbol{H}}_{\|\,n}. \quad (18)$$

It follows from (18) that the Leontovich approximate impedance boundary condition is valid only for the first two terms of the asymptotic series. The deviation takes

place starting from $n = 2$ (ε^2), for which (18) gives $\dot{\boldsymbol{E}}_{\|2} = \left[1 - 1/\left(2\mu^2\right)\right]\boldsymbol{e}_z \times \dot{\boldsymbol{H}}_{\|2}$. The requirement for fulfilling assumption in the approximate impedance boundary condition that the normal field component is equal to zero is more stringent. It holds only for the zero term of the asymptotic series and it is violated already at ε^1.

Influence of the small parameter value to the field penetration low with the strong skin effect. Let us perform a quantitative assessment of the influence of the small parameter value ε to the change in the penetration law of the electromagnetic field into conducting half-space. The analysis is carried out based on the expansion of expressions (4) in the asymptotic series, where for small ε the Taylor series expansion of the factor in the integrand is used near the zero value of the integration variable χ.

Unlike (9), for the asymptotic expansion of improper integrals (4), it is necessary to use not only the expansion in a power series of the function $w_1^{-1}(\chi)$, but also the expansion of the exponential function (5). Taking into account, except one, next term in the expansion of the factor $\sqrt{1+\left[\chi/\left(\mu\sqrt{i}\right)\right]^2}$, approximate expression for exponential function (5) will be as follows

$$\exp\left(\sqrt{2i}\frac{z}{\delta}\sqrt{1+\left(\frac{\chi}{\mu\sqrt{i}}\right)^2}\right) \approx \left[1+\sqrt{2i}\frac{z}{\delta}\cdot\frac{1}{2\mu^2}\left(\frac{\chi}{\sqrt{i}}\right)^2\right]\exp\left(\sqrt{2i}\frac{z}{\delta}\right), \quad (19)$$

where it is considered that the ratio z/δ does not exceed several units.

Taking into account (19), the functions $f_1(z/\delta,\varepsilon,\beta)$ and $f_2(z/\delta,\varepsilon,\beta)$ in (4) can be approximately represented as following (below we use the combined designation $f_{1,2}(z/\delta,\varepsilon,\beta)$ for the two functions)

$$f_{1,2}\left(\frac{z}{\delta},\varepsilon,\beta\right) \approx \exp\left(\sqrt{2i}\frac{z}{\delta}\right)\left[f_{1,2}(0,\varepsilon,\beta)+\sqrt{2i}\frac{z}{\delta}\cdot\frac{1}{2\mu^2}k_{1,2}(0,\varepsilon,\beta)\right], \quad (20)$$

where $k_{1,2}(0,\varepsilon,\beta)$ differ from $f_{1,2}(0,\varepsilon,\beta)$ by the presence of factor $\left(\chi/\sqrt{i}\right)^2$ in the integrands (4).

After substitution $1/w_1 = \sum_{n=0}^{\infty} a_n(\mu)\left(\chi/\sqrt{i}\right)^n$, the functions $k_{1,2}(0,\varepsilon,\beta)$ and $f_{1,2}(0,\varepsilon,\beta)$ can be represented as expansion in asymptotic series, similarly G_e to (15) for $z = 0$

$$\begin{cases} f_1(0,\varepsilon,\beta) = \sqrt{i}\sum_{n=0}^{N} a_n f_{1,n}, \; f_2(0,\varepsilon,\beta) = \sqrt{i}\sum_{n=0}^{N} a_n f_{2,n}, \\ k_1(0,\varepsilon,\beta) = \sqrt{i}\sum_{n=0}^{N} a_n f_{1,n+2}, \; k_2(0,\varepsilon,\beta) = \sqrt{i}\sum_{n=0}^{N} a_n f_{2,n+2}, \end{cases} \quad (21)$$

where

$$f_{1,n} = \int_0^{\infty}\left(\chi/\sqrt{i}\right)^{n+1}\exp\left(-\frac{\chi\cos\beta}{\varepsilon}\right)J_0\left(\frac{\chi\sin\beta}{\varepsilon}\right)d\chi,$$
$$f_{2,n} = \int_0^{\infty}\left(\chi/\sqrt{i}\right)^{n+1}\exp\left(-\frac{\chi\cos\beta}{\varepsilon}\right)J_1\left(\frac{\chi\sin\beta}{\varepsilon}\right)d\chi. \quad (22)$$

To obtain the final expressions, it is sufficient to use expressions (14) – (16) of the expansion into asymptotic series of the electric and magnetic intensities at the interface. In this case, for the additional term containing $k_{1,2}(0,\varepsilon,\beta)$, the same expressions will be valid, in which the values of the degree of functions and derivatives change from n to n+2. Besides, since in (20) only one additional term of the series is taken into account, the functions $k_{1,2}(0,\varepsilon,\beta)$ must also contain only one term of the expansion. With the same exactness the functions $f_{1,2}(0,\varepsilon,\beta)$ can contain no more than three terms of the series. As a result, using the value of the field intensity at the interface (14), the expression in which the difference from unity for the factor in the exponential function is taken into account will be as following

$$\dot{\boldsymbol{E}}_i \approx 2e^{pz}\boldsymbol{e}_z \times \left\{ \begin{array}{l} \dot{\boldsymbol{H}}_{0\|} - \frac{\mu}{p}\frac{\partial\dot{\boldsymbol{H}}_{0\|}}{\partial z}\Big|_{z=0} + \left(\frac{\mu}{p}\right)^2\left(1-\frac{1}{2\mu^2}\right)\frac{\partial^{(2)}\dot{\boldsymbol{H}}_{0\|}}{\partial z^2}\Big|_{z=0} + \\ + \left(\frac{\mu}{p}\right)^2\frac{pz}{2\mu^2}\frac{\partial^{(2)}\dot{\boldsymbol{H}}_{0\|}}{\partial z^2}\Big|_{z=0} \end{array} \right\}. \quad (23)$$

Similarly, using the values of the components of the magnetic field intensities at the boundary (15), (16) and the expansion of the exponential function (19), we can also write approximate expressions for the decrease of the non-uniform magnetic field in the conducting half-space

$$\dot{\boldsymbol{H}}_{i\|} \approx 2e^{pz}\left\{ \begin{array}{l} \dot{\boldsymbol{H}}_{0\|} - \frac{\mu}{p}\frac{\partial\dot{\boldsymbol{H}}_{0\|}}{\partial z}\Big|_{z=0} + \left(\frac{\mu}{p}\right)^2\left(1-\frac{1}{2\mu^2}\right)\frac{\partial^{(2)}\dot{\boldsymbol{H}}_{0\|}}{\partial z^2}\Big|_{z=0} + \\ + \left(\frac{\mu}{p}\right)^2\frac{pz}{2\mu^2}\frac{\partial^{(2)}\dot{\boldsymbol{H}}_{0\|}}{\partial z^2}\Big|_{z=0} \end{array} \right\}, \quad (24)$$

$$\dot{\boldsymbol{H}}_{i\perp} \approx -\frac{2}{p}e^{pz}\left\{ \begin{array}{l} \frac{\partial\dot{\boldsymbol{H}}_{0\perp}}{\partial z}\Big|_{z=0} - \frac{\mu}{p}\frac{\partial^{(2)}\dot{\boldsymbol{H}}_{0\perp}}{\partial z^2}\Big|_{z=0} + \left(\frac{\mu}{p}\right)^2\left(1-\frac{1}{2\mu^2}\right)\frac{\partial^{(3)}\dot{\boldsymbol{H}}_{0\perp}}{\partial z^3}\Big|_{z=0} + \\ + \left(\frac{\mu}{p}\right)^2\frac{pz}{2\mu^2}\frac{\partial^{(3)}\dot{\boldsymbol{H}}_{0\perp}}{\partial z^3}\Big|_{z=0} \end{array} \right\}. \quad (25)$$

For the components of the electromagnetic field $\dot{\boldsymbol{E}}_{i\|} = \dot{\boldsymbol{E}}_i$ and $\dot{\boldsymbol{H}}_{i\|}$, directed parallel to the interface between the media, the deviation from the penetration law of uniform field takes place for the terms of series proportional to the second-order derivative of the field intensities at the surface. The deviation for the component of the magnetic field intensity perpendicular to the surface $\dot{\boldsymbol{H}}_{i\perp}$ occurs for the term of series proportional to the third-order derivative. This is due to the absence of local value of the field at the surface in (18) which already contains a common factor proportional to the value ε.

As follows from (23) – (25), the deviation of the penetration law of non-uniform electromagnetic field in conducting medium from the penetration law of uniform one appears when the small parameter is taken into account in the second power ε^2. This conclusion is in agreement with the calculation results shown in Fig. 7,*b* and 8,*b*. In addition, it follows from (23) – (25) that the maximum value of the modulus of the additional term takes place at the maximum value of the function $\left|pz\exp(pz)\right| = \left|\left(\sqrt{2}z/\delta\right)\exp\left(z/\delta\right)\right|$, which is realized at $-z = \delta$. This value also agrees well with the ratio z/δ in Fig. 7,*b* and 8,*b* when the deviation reaches its maximum value.

As can be seen from (23) – (25), for all components of the electromagnetic field with strong skin effect, the deviation of the penetration law of non-uniform

electromagnetic field from the penetration law of uniform one is determined by the value of the same parameter

$$\left(\frac{\mu}{p}\right)^2 \frac{pz}{2\mu^2} \sim \left(\frac{\varepsilon}{\mu}\right)^2 \frac{z}{\delta}. \qquad (26)$$

Estimate (26) takes into account only the difference between the field penetration laws. The total relative error associated with the use of the model of perfect skin effect will be much more, since this model also does not take into account the field non-uniformity at the interface.

Conclusions.

The exact analytical solution of the three-dimensional problem of quasi-stationary electromagnetic field in the system «current contour of arbitrary configuration – conducting half-space» allows to obtain some general substantiated consequences of the field formation. These consequences, considered in the paper, are as follows.

1. It has been established that non-uniform electromagnetic field, upon penetration into conducting half-space, decreases in depth always faster than uniform field. Quantitative characteristic of the field decrease rate can be considered the parameter proportional to the ratio of the penetration depth of uniform field to the distance from external sources to the interface between dialectic and conducting media. With decrease in this parameter, the field is decreased slower, tending to the slowest decrease of uniform electromagnetic field, when the quantitative parameter tends to zero.

2. From the point of view of the possibility of using the penetration law of uniform field the concept of a strong skin effect can be extended. The skin effect can be considered strong when the penetration depth is small not only with respect to the characteristic dimensions of conducting body, but also of the entire electromagnetic system, including the distance from the surface of body to the external sources. In this case, the introduced quantitative parameter is small.

3. In the case of strong skin effect in its extended interpretation the non-uniformity of the electromagnetic field affects both the values of the field intensities at the interface between the media and the field penetration law into conducting body. The effect of field non-uniformity at the boundary surface is expressed in the fact that the electric and magnetic field intensities, in addition to local values, contain derivatives of the external sources field with respect to the coordinate perpendicular to the interface. The found analytical expressions for the field intensities in the form of asymptotic series make it possible to generalize the Leontovich impedance boundary condition to the diffusion of non-uniform field into conducting half-space. The mathematical model of the uniform field penetration into conducting medium to study the penetration of the non-uniform electromagnetic field is valid up to the introduced small parameter in the first degree. At the same time, the use of exponential decrease of the uniform field from its value at the boundary, determined with regard for its non-uniformity, is valid up to the small parameter already in the second power. The same limitation is valid when using the Leontovich approximate impedance boundary condition.

Further theoretical work is possible in the direction of a more general description of the non-uniform field of sources, not being limited to external sources in the form of current contours. The development of the theory is also possible in the direction of the formulation of boundary value problems, taking into account the known, as it shown, field at the interface between media. The found features of the field formation can make a practical importance when simulating processes, for example, by integral methods in devices with three-dimensional electromagnetic fields. The peculiarities of the distribution of the non-uniform electromagnetic field on the surface and in the skin layer of conducting body imply the study of its influence on the energy and force characteristics, the distribution of the Poynting vector and the Maxwell stress tensor.

Acknowledgment. The research was partially supported by the project 0115U004398 of the Institute of Electrodynamics of the National Academy of Sciences of Ukraine.

Conflict of interest. The author declare no conflict of interest.

REFERENCES

1. Rudnev V., Loveless D., Cook R.L. *Handbook of induction heating*. London, Taylor & Francis Ltd, 2017. 772 p. doi: https://doi.org/10.1201/9781315117485.

2. Lucía O., Maussion P., Dede E.J., Burdío J.M. Induction Heating Technology and Its Applications: Past Developments, Current Technology, and Future Challenges. *IEEE Transactions on Industrial Electronics*, May 2014, vol. 61, no. 5, pp. 2509-2520. doi: https://doi.org/10.1109/tie.2013.2281162.

3. Acero J., Alonso R., Burdio J.M., Barragan L.A., Puyal D. Analytical equivalent impedance for a planar circular induction heating system. *IEEE Transactions on Magnetics*, Jan. 2006, vol. 42, no. 1, pp. 84-86. doi: https://doi.org/10.1109/tmag.2005.854443.

4. Babutskii A.I., Chrysanthou A., Ioannou J. Effect of pulsed electric current treatment on corrosion of structural metals. *Strength of Materials*, 2009, vol. 41, no. 4, pp. 387-391. doi: https://doi.org/10.1007/s11223-009-9142-3.

5. Gallo F., Satapathy S., Ravi-Chandar K. Melting and crack growth in electrical conductors subjected to short-duration current pulses. *International Journal of Fracture*, 2010, vol. 167, no. 2, pp. 183-193. doi: https://doi.org/10.1007/s10704-010-9543-0.

6. Vasetsky Y.M., Kondratenko I.P. Electromagnetic field of the inductor for local electric pulse effects on metal products, *Technical Electrodynamics*, 2020, no 4, pp. 11-14. (Ukr). doi: https://doi.org/10.15407/techned2020.04.011.

7. Psyk V., Risch D., Kinsey B.L., Tekkaya A.E., Kleiner M. Electromagnetic forming – A review. *Journal of Materials Processing Technology*, 2011, vol. 211, iss. 5, pp. 787-829. doi: https://doi.org/10.1016/j.jmatprotec.2010.12.012.

8. Gayakwad D., Dargar M.K., Sharma P.K., Rajesh purohit, Rana R.S. A Review on Electromagnetic Forming Process. *Procedia Materials Science*, 2014, vol. 6, pp. 520-527. doi: https://doi.org/10.1016/j.mspro.2014.07.066.

9. Batygin Y., Barbashova M., Sabokar O. *Electromagnetic Metal Forming for Advanced Processing Technologies*. Springer, Cham, 2018. doi: https://doi.org/10.1007/978-3-319-74570-1.

10. Yuferev S.V., Ida N. *Surface Impedance Boundary Conditions: A Comprehensive Approach*. CRC Press, 2010. 412 p. doi: https://doi.org/10.1201/9781315219929.

11. Landau L.D., Lifshitz E.M. *Electrodynamics of Continuous Media*. Elsevier Ltd, 1984. 475 p. doi: https://doi.org/10.1016/b978-0-08-030275-1.50024-2.
12. Knoepfel H. *Pulsed High Magnetic Fields*. Canada: John Wiley & Sons, Limited, 1997. 372 p.
13. Leontovich M.A. On the Approximate Boundary Conditions for Electromagnetic Field on the Surface of Highly Conducting Bodies. *Propagation of electromagnetic waves*, Moscow, USSR Academy of Sciences Publ., 1948, pp. 5-20 (Rus).
14. Rytov S.M. Calculation of skin effect by perturbation method. *Journal of Experimental and Theoretical Physics*, 1940, vol. 10, iss. 2, pp. 180-190. (Rus).
15. Mitzner K.M. An integral equation approach to scattering from a body of finite conductivity. *Radio Science*, 1967, vol. 2, iss. 12, pp. 1459-1470. doi: https://doi.org/10.1002/rds19672121459.
16. Kravchenko A.N. *Boundary Characteristics in Electrodynamics Problems*. Kyiv, Naukova Dumka Publ., 1989. 218 p. (Rus).
17. Fridman B.E. Skin effect in massive conductors used in pulsed electrical devices: I. Electromagnetic field of massive conductors. *Technical Physics*, 2002, vol. 47, no. 9, pp. 1112-1119. doi: https://doi.org/10.1134/1.1508074.
18. Berdnik S.L., Penkin D.Y., Katrich V.A., Penkin Y.M., Nesterenko M.V. Using the concept of surface impedance in problems of electrodynamics (75 years later). *Radio physics and radio astronomy*, 2014, vol. 19, no. 1, pp. 57-80. doi: https://doi.org/10.15407/rpra19.01.057.
19. Liu X., Yang F., Li M., Xu S. Generalized Boundary Conditions in Surface Electromagnetics: Fundamental Theorems and Surface Characterizations. *Applied Sciences*, 2019, vol. 9, no. 9, p. 1891. doi: https://doi.org/10.3390/app9091891.
20. Vasetsky Yu.M., Dziuba K.K. An analytical calculation method of quasi-stationary three-dimensional electromagnetic field created by the arbitrary current contour that located near conducting body. *Technical Electrodynamics*, 2017, no 5, pp. 7-17. (Rus). doi: https://doi.org/10.15407/techned2017.05.007.
21. Vasetsky Yu.M., Dziuba K.K. Three-dimensional quasi-stationary electromagnetic field generated by arbitrary current contour near conducting body. *Technical Electrodynamics*, 2018, no 1, pp. 3-12. doi: https://doi.org/10.15407/techned2018.01.003.
22. Vasetsky Yu.M., Dziuba K.K., Kucheriava I.M., Mazurenko I.L. The penetration of nonuniform electromagnetic field of current contour in conducting medium. *Technical Electrodynamics*, 2018, no 5, 11-14. (Ukr). doi: https://doi.org/10.15407/techned2018.05.011.
23. Vasetsky Yu. Nonuniform electromagnetic field at the interface between dielectric and conducting media. *Progress in Electromagnetics Research Letters*, 2020, vol. 92, pp. 101-107. doi: https://doi.org/10.2528/pierl20050802.
24. Simonyi K. *Foundation of electrical engineering*. Elsevier Ltd, 1963. 865 p. doi: https://doi.org/10.1016/c2013-0-02694-1.
25. Vasetsky Yu., Mazurenko I., Dziuba K. Conditions for Application of Asymptotic Method to Electromagnetic Field Analysis in System of «a Current Loop – an Eletroconducting Body». *Computational Problems of Electrical Engineering*, 2014, vol. 4, no. 1, pp. 91-96. Available at: http://science.lpnu.ua/sites/default/files/journal-paper/2017/sep/6032/19.pdf (accessed 20.12.2020).

Received 29.12.2020
Accepted 03.02.2020
Published 05.04.2021

Yu.M. Vasetsky[1], *Doctor of Technical Science, Professor,*
[1] Institute of Electrodynamics of the National Academy of Sciences of Ukraine,
56, Peremohy Avenue, Kyiv, 03057, Ukraine,
e-mail: yuriy.vasetsky@gmail.com

How to cite this article:
Vasetsky Yu.M. Penetration of non-uniform electromagnetic field into conducting body. *Electrical Engineering & Electromechanics*, 2021, no. 2, pp. 43-53. **doi: 10.20998/2074-272X.2021.2.07.**

UDC 621.3 **doi: 10.20998/2074-272X.2021.2.08**

N. Benchouia, M. Saaidia

OPTIMIZATION AND RELIABILITY OF THE POWER SUPPLY SYSTEMS OF A COMPRESSOR STATION

As gas pipeline systems become larger and more complex, the importance of optimally operating and planning these facilities has increased. The capital costs and operating expenses of pipeline systems are so large that even small improvements in the use of the system can involve large sums of money. ***Purpose****. This article proposes a method to improve the reliability and optimization of power supply systems for compressor stations.* ***The novelty*** *of the proposed work is the development of a new mathematical model that allows the choice of the most appropriate maintenance policies in the best way to significantly reduce costs as well as to optimize useful key performance indicators – failure rate, average time between breakdowns, the average repair time for equipment in compressor station electrical supply systems. Applying graph theory to represent this mathematical model from the schematic diagram of the different energy sources with respect to the five compressor stations is adequate.* ***Methods.*** *The problem that arises for the future operator or operator is, among others, how to balance two main aspects: a technical aspect and an economic aspect. The proposed methodology introduces a research algorithm to calculate the optimal values of the operating parameters of the power supply systems of compressor stations by combining technical and economic aspects in order to reduce costs and increase performance indicators. The proposed algorithm can be implemented in FORTRAN code.* ***Results.*** *The algorithm developed is an efficient tool for calculating maintenance costs and allows by means of programming to define the most appropriate maintenance policy. On the other hand, this technique could be used as an essential economic evaluation indicator for other equipment in order to choose among all the technically possible solutions the one which allow obtaining the best economic result.* ***Practical value.*** *The proposed algorithm has been examined in this third variant of the supply system with two turbogenerators. The result of the optimization shows a clear preference for selecting station C for the pipeline as this presents the minimum cost which is the definition of the algorithm optimizer. Then, it is important to adopt the most recommended maintenance policies and practices in order to ensure the availability of the power supply systems and to avoid unplanned outages with the resulting loss of production.* References 12, table 2, figures 7.

Key words: **power supply system, reliability, optimization, economic aspects, technical aspects, graph theory.**

У міру того як газопровідні системи стають дедалі більшими та складнішими, зростає значення оптимального функціонування та планування цих об'єктів. Капітальні витрати та експлуатаційні витрати трубопровідних систем настільки великі, що навіть незначні вдосконалення у використанні систем можуть залучити великі суми грошей. ***Мета****. У статті пропонується метод підвищення надійності та оптимізації систем електропостачання компресорних станцій.* ***Новизна*** *запропонованої роботи полягає у розробці нової математичної моделі, яка дозволяє найкращим чином вибрати найбільш відповідні політики технічного обслуговування, щоб значно скоротити витрати, а також оптимізувати корисні ключові показники ефективності – рівень відмов, середній час між поломками, середній час ремонту обладнання в системах електропостачання компресорної станції. Застосування теорії графів для представлення цієї математичної моделі на принциповій схемі різних джерел енергії щодо п'яти компресорних станцій є достатнім.* ***Методи****. Задача, яка виникає у майбутнього або діючого оператора, полягає, серед іншого, у тому, як збалансувати два основні аспекти: технічний аспект та економічний аспект. Запропонована методологія вводить алгоритм дослідження для розрахунку оптимальних значень робочих параметрів систем електропостачання компресорних станцій шляхом поєднання технічних та економічних аспектів з метою зменшення витрат та збільшення показників ефективності. Запропонований алгоритм може бути реалізований у програмі на мові програмування FORTRAN.* ***Результати****. Розроблений алгоритм є ефективним інструментом для розрахунку витрат на технічне обслуговування та дозволяє за допомогою програмування визначити найбільш відповідну політику технічного обслуговування. З іншого боку, цю методику можна використовувати як важливий показник економічної оцінки для іншого обладнання, щоб вибрати серед усіх технічно можливих рішень те, яке дозволяє отримати найкращий економічний результат.* ***Практичне значення****. Запропонований алгоритм був перевірений у третьому варіанті системи живлення з двома турбогенераторами. Результат оптимізації показує чітку перевагу щодо вибору станції С для трубопроводу, оскільки це представляє мінімальну вартість, яка є визначенням оптимізатора алгоритму. Тоді важливо прийняти найбільш рекомендовані політики та практики технічного обслуговування, щоб забезпечити доступність систем електропостачання та уникнути незапланованих відключень із наслідком втрат виробництва.* Бібл. 12, табл. 2, рис. 7.

Ключові слова: **система електропостачання, надійність, оптимізація, економічні аспекти, технічні аспекти, теорія графів.**

Introduction. Compressor station (CS) is an integral and an essential part of a gas pipeline, providing gas transportation by means of power equipment. It serves as a control element in the complex of buildings, belonging to the trunk gas pipeline. The pipeline operation mode is defined through the compressor station operation parameters.

Power supply system (PSS) is a combination of sources and systems of conversion, transmission and electric energy distribution. Power supply system does not usually include consumers (or electricity receivers).

The following requirements are to be met by power supply systems:

- reliability and continuity of power supply to consumers;
- quality of electric energy on consumer input;
- safety of PSS elements maintenance;
- unification (modularity, standardization);
- economic efficiency (includes such concepts as energy efficiency and energy conservation);
- ecological compatibility;
- ergonomics [1].

As natural gas pipeline systems have grown larger and more complex, the importance of optimal operation

and planning of these facilities has increased. The investment costs and operating expenses of pipeline networks are so large that even small improvements in system utilization can involve substantial amounts of money saving [2].

For electric power supply systems, intended to provide the work of processing facilities with a continuous cycle (such systems include compressor stations of trunk gas pipelines) reliability and maintainability are considered to be the main properties. Problems of durability and safety of the system are not too much crucial. For modern electrical driven, equipped with powerful synchronous motors, problems of stability and vitality of the systems and their power supply are considered to be additional important properties [1].

In a gas transmission network, the overall operating cost of the system is highly dependent upon the operating cost of the compressor stations of the network. In fact, this compressor station's operating cost is generally measured by the quantity of the consumed fuel. According to [3], the operating cost of running the compressor stations represents between 25 % and 50 % of the total company's operating budget.

Recently, the issues of reliability improvement and configuration optimization of power supply systems of industrial facilities have been gaining significance [4]. Reliability is all that is required for a product to function without failure, or with a failure frequency low enough to be acceptable in its intended use. Its conservation concerns the Maintainability which takes care of what must be done so that a product is brought back under conditions as close as possible to those foreseen at the beginning of its operation.

Many researchers have presented and described proposed optimization and reliability methods for power supply systems of a compressor station. Literature reviews have been written to summarize the methods and the achievements. In [5] authors have illustrated the different influencing factors for the economic success of a gas compression station. Important criteria include first cost, operating cost (especially fuel cost), capacity, availability, life cycle cost, and emissions. Decisions about the layout of compressor stations such as the number of units, standby requirements, type of driver and type of compressors have an impact on cost, fuel consumption, operational flexibility, emissions, as well as availability of the station. An overview of important mathematical optimization and artificial intelligence (AI) techniques used in power optimization problems. Applications of hybrid (AI) techniques have also been discussed in [6]. The statistical data on the failures of the elements of the electrical power systems for the gas pumping compressor stations is studied in [7]. The distribution functions of operating time between failures, operating time between unplanned repairs, restoration time are chosen for power supply systems' elements. Parameters of Weibull distribution function are determined. The reliability of power supply system for gas pumping compressor station is simulated. Comparative analysis of the system reliability with hot and cold reserve is processed. The role of elements and their parameters for ensuring reliability are determined. The rational boundaries for increasing reliability for the most important system elements are determined in [7]. In [8] authors solve the reliability design problem which is a very interesting problem often encountered in the energy industry. It is formulated as a sequence of redundancy optimization problems (ROP). The resolution of this problem uses a developing Ant Colony Optimization (ACO) method. This new algorithm for choosing an optimal series-parallel power structure configuration is proposed. It minimizes the total investment cost subject to availability constraints.

However, many of the algorithms currently used by the system operators and planners are based on heuristics and have severe limitations. Therefore, optimization algorithms used during operations need to be timely in detecting problems and suggesting corrective actions.

The goal of the paper is the proposal of a tool allowing to optimize the power supply systems of a real existing compressor station, taking into account the technical aspect and the economic aspect on the basis of a mathematical model which makes it possible to increase the reliability of the entire operation of the mechanism and to considerably ensure its availability in order to minimize the total expenditure of the electrical supply system of the BISKRA station, Algeria.

Subject of investigations. This paper carries out a comprehensive study of calculation and optimization of the power supply systems of compressor stations with the essential objective of choosing among all the technically possible solutions those which allows obtaining the best economic result.

In this article, a new flexible and efficient model and an optimization algorithm is proposed in order to solve the problem of reliability, maintainability and availability of operation in order to minimize the costs of the power supply systems of natural gas compression stations.

This paper is structured as follows: in Section 2, the description of the compressor station and the technological process used in the model formulation are presented; in Section 3, a development optimization criterion is introduced; the development of the power system optimization algorithm is presented in Section 4. The results showing the graphic presentation of the calculation and the performance of the proposed formulation are presented in Section 5. Finally, in Section 6, conclusion on the achieved results is presented.

Presentation of the compressor station. In [9] the gas pipeline GK1 (40'') GK2 (42'') is designed to ensure the connection between the departure terminal of HASSI R'MEL and the arrival terminal of SKIKDA, as well as the supply of the SONELGAZ (The Algerian Electricity production and distribution company) distribution centers in eastern Algeria.

Construction of the pipeline began in 1968 for it to be commissioned in its first phase in 1971.

In its first phase, the gas pipeline ensured a flow of 5.7×10^9 m³/year with no in-line compressor station (free flow).

In its second phase and with increasing energy requirements, two compressor stations were installed (stations B and D) to achieve a flow rate of 9.2×10^9 m³/year.

In its third phase, the gas pipeline is operated with five in-line compression stations thus ensuring maximum speed with a flow rate of 12.7×10^9 m³/year.

The natural gas pipe between HASSI R'MEL and SKIKDA has a length of 574.87 km. It is designed to service at an absolute pressure of 71.05±0.4 bars and a maximum temperature of 60 °C over its entire length.

The departure terminal controls the inlet pressure of 71.05±0.4 bars absolute of the pipe. The arrival terminal is able to maintain downstream pressure from 43 to 45 bars absolute. The annual flow from HASSI R'MEL is 12.7×10^9 m^3/year (optimal conditions in summer and winter). Table 1 details the operating conditions of the five stations such as compressor suction pressure, compressor suction temperature, maximum power, etc.

Table 1

Service condition of stations

Station / Condition	A	B	C	D	E
Compressor (in service + reserve)	3+1	3+1	3+1	3+1	3+1
Gas flow per machine (kg/h)	455.93	449.96	442.46	439.80	432.30
Compressor suction pressure (bar)	50.49	48.15	48.30	48.41	50.14
Temperature compressor suction (°C)	38.06	44.86	43.94	44.60	40.93
Compressor cooling point (bar)	73	73	73	73	73
Compressor discharge temperature (°C)	–	–	–	–	–
Maximum station output (bar)	71.5	71.5	71.5	71.5	71.5

Description of the technological process. The station's gas compression system begins at the filter inlet manifold located in the northeast corner of the facility site (or refers to the north of the facility, not true north).

The gas passes through vertical filters that retain moisture and filings making the gas suitable for recompression in the station compressors to the turbocompressors (TC) suction manifold.

In [9] the «A», «B», «C» and «D» turbocompressors are individually connected to this manifold. The suction line of each compressor is 60.96 cm in diameter (see Fig. 1).

The gas is sucked into the compressor or its pressure is increased to 73 bars absolute. It is discharged into the discharge manifold through the 60.96 cm discharge line of each compressor. The discharge manifold directs gas to a calibrated orifice where the rate of flow is determined. The gas then passes into the after cooler where its temperature is reduced to a value not exceeding 60 °C.

From the coolers, the gas passes through the 101.6 cm mainline. The pressure losses in the gas refrigerants are 1.5 bars absolute; so at the exit of the station, we will have the extreme values of pressure and temperature which are 71.5 bars absolute and 60 °C.

For this technological process to be ensured, the turbocompressors must be in good working order. So the adopted power supply system plays a key role.

According to statistical calculations, failures of fuel systems have a direct influence on the reduction of the operating time of turbochargers (restarting, fuel and oil losses, etc.). This is why the analysis of adequate feeding systems for this type of process becomes an absolute necessity.

Figure 1 shows the technological process of the compressor station. We find that failures in the power supply system directly affect the decrease in uptime of turbocompressors.

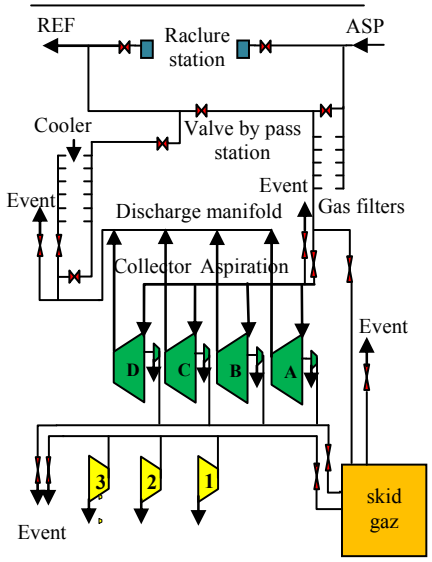

Fig. 1. Technological process of a compressor station

Proposed optimization methodology. The methodology of the proposed study is based on the calculation and optimization of the power supply systems of compressor stations on the basis of two main aspects: a technical aspect and an economic aspect.

Technical aspect. The technical aspect is the ability of the power supply system to provide the compressor station with the electrical energy of a required quality without interruption; which means to reduce the damage due to accidental failures (interruption in electrical energy) by increasing the reliability of the power supply system while maintaining the economic conditions surrounding the problem. The process of reliability evaluation may be done using two major groups of statistical indicators: λ, MTBF (Mean Time Before Failure) and MTTR (Mean Time To Repair) are the two main indicators of reliability used industrially [10].

Failure rate λ represents the failure rate or the damage rate. It characterizes the speed of variation of reliability over time for a given work period, total duration in active service

$$\lambda = \frac{\text{Total number of failures during service}}{\text{Total operating time}}. \quad (1)$$

In practice, the failure rate can be constant, but also increasing or decreasing over time, with gradual change and without discontinuity.

The failure rate is the probability that an entity will lose its ability to perform a function during the interval, knowing that it has not failed between [0, t]; we note it:

$$\lambda(t) = \frac{1}{MTBF}. \quad (2)$$

MTBF is often translated as being the average of good functioning but represents the average of the times between two failures (*TBF*):

$$MTBF = \frac{\sum TBF}{N}, \quad (3)$$

where N is the number of failures.

MTTR is average time to repair which expresses the average time for repair spots. It is calculated by adding the active times maintenance as well as additional maintenance times, all divided by the number of interventions:

$$MTTR = \frac{\sum \text{intervention time for } N \text{ failures}}{N}, \quad (4)$$

repair rate μ is

$$\mu = \frac{1}{MTTR}. \quad (5)$$

Economic aspect. In the economic study comparing the different variants of the power supply system, the factors directly influenced by reliability considerations are investments (installation expenditure), on one hand, and maintenance expenses, supervision expenses, expenses due to loss of electrical power and transformers and depreciation expenses on the other hand. These expenses are called operating expenses [11].

Therefore, the solution to be adopted must minimize the total expenditure on the power supply system in question, which is given by the following formula:

$$C_t = P_n.C_{inst} + C_{op} + D \to \min, \quad (6)$$

where P_n is the normative coefficient of investment efficiency; C_{inst} is the installation (capital) expenses for power system components by line; C_{op} is the operating expenses; D is the damage due to accidental power system failures.

P_n depends on the period of depreciation of the invested capital as follow:

$$P_n = \frac{1}{T_d} = 0.12, \quad (7)$$

where the period of depreciation as follows:

$$T_d = (8 \div 10), \text{ year}. \quad (8)$$

C_{inst} is given by the following formula:

$$C_{inst_l} = I_0 \cdot l, \quad (9)$$

where I_0 is the kilometric price, (DA/km, DA – Algerian Dinar) and l is the length of line, km.

For transformers:

$$C_{inst_{TR}} = N \cdot I_{TR}, \quad (10)$$

where N being the number of transformers to install and I_{TR} is the price of a processor, DA.

For turbogenerators:

$$C_{inst_{TG}} = N \cdot I_{TG}, \quad (11)$$

where N is the number of turbogenerators; I_{TG} is the price of a turbogenerator, DA.

C_{op} is given by the following formula:

$$C_{op} = C_{losses} + d_{an} + C_m, \quad (12)$$

where C_{losses} is the expenditure due to loss of electrical energy in the line and transformers, can be represented as follows:

$$C_{losses} = (\Delta w_l + \Delta w_{TR}) \cdot C_0, \quad (13)$$

where Δw_l represents the losses of electrical energy in the line:

$$\Delta w_l = \left(\frac{S_{\max}}{V_n} \right)^2 \cdot r_0 \cdot l \cdot \tau_{\max} \cdot 10^3, \quad (14)$$

where $S_{\max}$ is the maximum apparent power passing through the line (in MVA) depending on the parameters: V_n is the electrical power transmission rating, kV; r_0 is the specific resistance of the line, Ω/km; l is the length of line, km; $\tau_{\max}$ is the maximum time of loss of electrical energy during one year, h/year; Δw_{TR} is the losses of electrical energy in the transformer:

$$\Delta w_{TR} = \Delta P_0 \cdot T_f + \Delta P_a \cdot K_l^2 \cdot \tau_{\max}, \quad (15)$$

where ΔP_0 is the active power losses in the magnetic circuit (not depending on load), kW; T_f is the transformer operating time during one year (T_f = 8760 h); ΔP_a is the active power losses in windings created by Joule effect, kW; K_l is the transformer load factor (K_l = 0.7); C_0 is the cost of one kilowatt hour of electrical energy, DA/kWh.

Annual depreciation expenses d_{an} to offset expenses due to wear and tear of power system components is given by the following formula:

$$d_{an} = \frac{\alpha(\%)}{100} \cdot I, \quad (16)$$

where α is the depreciation rate; it varies from one element to another (for the line α = 2.4 %; for the transformer α = 6.4 %; for the turbogenerator α = 6.5); I is the clean investment; C_m is the maintenance, inspection and supervision expenses. These are directly related to the degree of reliability and safety level imposed on the power system:

$$C_m \approx 0.20 \cdot d_{an}. \quad (17)$$

Damage due to accidental power system failures D:

$$D = 1.08 \cdot \Delta w_a \cdot C_0, \quad (18)$$

where 1.08 is the reserve coefficient which takes into account the accidental downtime of less than 0.1 hours; Δw_a is the electrical energy not delivered for one year due to accidental failure of the power supply system, kW·h/year.

$$\Delta w_a = P_M \cdot 8760 \cdot Q \cdot \varepsilon \cdot \beta_m \cdot \beta_q, \quad (19)$$

where P_M is the maximum active power (calculated) of the compressor station, kW; Q is the total probability of accidental failure of two power system circuits.

Practice has shown that accidental failures follow an exponential law:

$$Q = \tau \cdot \left(1 - e^{-\lambda}\right)/8760, \quad (20)$$

where τ is the total repair time of the power supply system expressed in hours; λ is the total failure rate of the power supply system expressed in 1/year; ε is the coefficient of the carried power limitation in the damage regime:

$$\varepsilon = \frac{P_M - P_a}{P_M}, \quad (21)$$

$$P_a = 1.4 \cdot S_{nTR} \cos\varphi, \quad (22)$$

where P_a is the allowable power of the transformer in the damage regime (in our study we considered the failure of two circuits of the power supply system, ($P_a = 0 \Rightarrow \varepsilon = 1$); β_m and β_q are respectively the filling coefficients of the monthly and daily load diagrams for a compression station: β_m = 0.97; β_q = 0.94.

Development of power system optimization algorithm. It is based on the graph theory which consists of developing a mathematical model based on the layout diagram of the different power sources compared to the five compressor stations. Figure 2 illustrates the graphic presentation of power supply system of compressor stations.

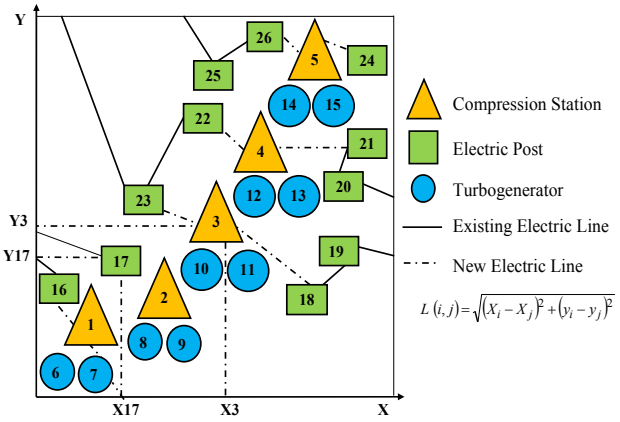

Fig. 2. Graphic presentation of power supply system of compressor stations

The power supply system is completely represented mathematically by a matrix $\boldsymbol{A}$ (N, M) which determines the connection between the compressor stations and the power sources (existing power line presents in Fig. 3).

This mathematical model allowed us to develop a calculation flowchart taking into account three essential conditions:

- substations (power sources) must have a reserve of electrical energy;
- a compressor station can only be powered from two power sources;
- the distance between the power source and a compressor station L must be less than the critical distance L_{CR} which depends on the nominal voltage of electric power transmission and power:

$$L(i,j) < L_{CR}, \tag{23}$$

where

$$L(i,j)=\sqrt{(X_i-X_j)^2+(y_i-y_j)^2}, \tag{24}$$

where (X_i, y_i) is the coordinates of the i^{th} electrical post or compressor station; (X_j, y_j) is the coordinates of j^{th} the electrical post.

Power sources										
Compression station	N	6	7	8	9	–	–	–	–	M
	1	0	1	0	0	0	1	0	0	0
	2	1	0	0	1	0	0	0	0	0
	3	0	0	1	0	1	0	0	0	0
	4	0	0	0	0	0	0	1	1	0
	5	0	0	0	0	1	1	0	0	0
Power sources	6	–1	0	0	–1	0	0	–1	0	0
	7	0	–1	0	0	–1	0	0	0	0
	8	0	0	–1	0	0	0	–1	0	0
	l	–	–	–	–	–	–	–	–	–
	l	–	–	–	–	–	–	–	–	–
	N	–	–	–	–	–	–	–	–	–

Optimization criteria:

$$C_t = P_n \cdot C_{inst} + C_{op} + D \rightarrow \min$$

C_t – total expenditure, DA;
P_n – normative coefficient, $P_n = 0.12$;
C_{inst} – installation expenses, DA;
C_{op} – operating expenses, DA;

$$C_{op} = C_{losses} + d_{an} + C_m$$

C_{losses} – expenses due to losses of electrical energy in lines and transformers;
d_{an} – annual depreciation expenses;
C_m – maintenance expenses, $C_m = 0.20 \cdot d_{an}$;
D – damage due to accidental failures of PSS, DA.

$$A(i,j) = \begin{cases} -1 & \text{if } (A_i, A_j) \in E(G) \text{ – points connected by an existing line} \\ 0 & \text{if } (A_i, A_j) \notin E(G) \text{ – no connections between points} \\ 1 & \text{if } (A_i, A_j) \in E(G) \text{ – points connected by a new line} \end{cases}$$

Fig. 3. The developed mathematical model of power supply system of compressor stations (where $A(i,j) = -1$ is connection between power sources (existing line); $A(i,j) = 0$ is no connection; $A(i,j) = 1$ is connection between power sources and compressor stations (new line)

Figure 4 shows the flow chart of the algorithm for optimization of n-electric power supply systems of compression stations. It allows, in its first part, to calculate the installation and operating expenses by different variants of the power supply system and in the second part, it allows us to calculate the damage due to accidental failures by different variants of the power supply system. This allows us to choose at the same time the most optimal variant of the power supply system which total expenses will be minimal.

Calculation of reliability parameters. The 100 % confidence in electrical equipment does not exist. So the concept of reliability only gives us the degree of confidence in this equipment. It leads to studies of failure rate (λ), repair time (τ), time of proper operation, etc. It becomes the link between the technological aspect and the economical aspect [11, 12]. For this reason, the reliability of an electrical power system is the probability that it will perform its mission satisfactorily and under specified environmental conditions.

Considering reliability economically as high availability is expensive. It is certain that the cost price of the power supply system has to be increased if we want the failure rate of the system to be reduced.

Figure 5 shows the expenditure curves according to reliability. This approach attempts to determine the appropriate sums to invest in reliability is to compare the costs caused by failures (that is, the costs resulting from poor reliability) with the costs necessary to provide greater reliability. It is clear when increasing the reliability of the power system it means reducing the risk of its failure (reducing damage).

This power supply system is a set of electrical equipments belonging to the group of repairable elements. Therefore; reliability is characterized by the failure rate (λ) and repair time (τ).

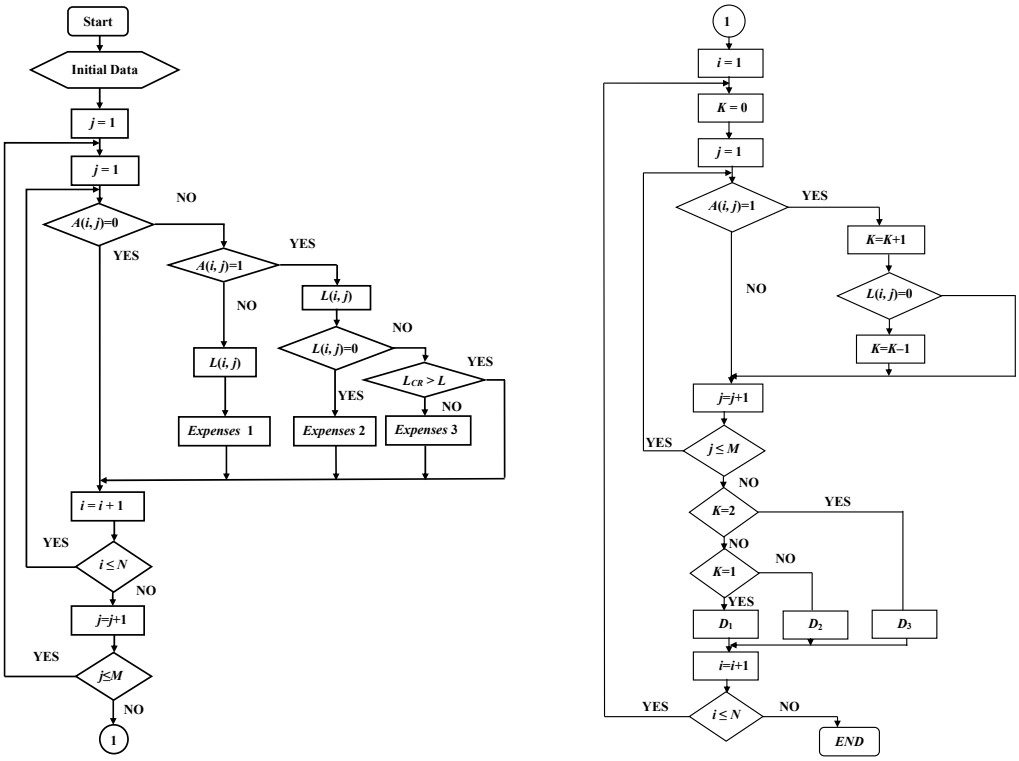

Fig. 4.The proposed and developed optimization algorithm of the power supply system

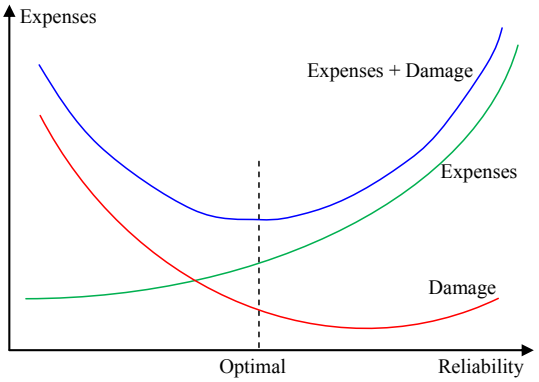

Fig. 5. Expenditure curves according to reliability [11]

Then the proper functioning of the power supply system results from the proper functioning of the various elements that compose it. In other words, the overall reliability requirement is reflected in the form of specific reliability requirements for each element.

These elements can be mounted in only two methods: in series or in parallel (or mixed). Three variants of the power supply system were considered for compressor stations:

a) from two electric lines;

b) from a single electric line and a turbogenerator (stand-alone power plant);

c) from two turbogenerators.

Our case study is based on this third variant of the supply system, i.e. from two turbogenerators.

Figure 6 shows the calculation of the reliability parameters λ, τ of the power supply system of compressor stations from two turbogenerators.

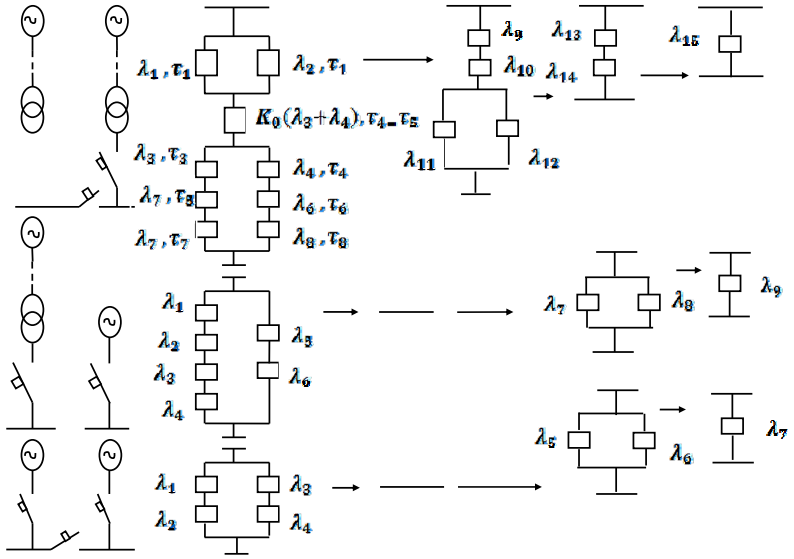

Fig. 6. Calculation of the reliability parameters λ, τ of the power supply system of compressor stations for the three variants

First variant of the power supply system – from two power lines.

First transformation.

$$\lambda_{1,2} = \lambda_1 \cdot \lambda_2 \cdot (\tau_1 + \tau_2) = \lambda_9 ; \quad (25)$$

$$\tau_{1,2} = \frac{\tau_1 \cdot \tau_2}{\tau_1 \cdot \tau_2} = \tau_9 , \quad (26)$$

where λ_1 and λ_2 are the failure rates of post 1 and post 2 respectively; τ_1 and τ_2 are the repair times of post 1 and post 2 respectively;

$$\lambda_{3,5} = \lambda_3 + \lambda_5 + \lambda_7 = \lambda_{11} ; \quad (27)$$

$$\lambda_{4,6} = \lambda_4 + \lambda_6 + \lambda_8 = \lambda_{12} ; \quad (28)$$

$$\tau_{3,5} = \frac{\lambda_3 \cdot \tau_3 + \lambda_5 \cdot \tau_5 + \lambda_7 \cdot \tau_7}{\lambda_3 + \lambda_5 + \lambda_7} ; \quad (29)$$

$$\tau_{4,6} = \frac{\lambda_4 \cdot \tau_4 + \lambda_6 \cdot \tau_6 + \lambda_8 \cdot \tau_8}{\lambda_4 + \lambda_6 + \lambda_8} , \quad (30)$$

where λ_7 and λ_8 are the failure rates of the circuit breaker 0.4 kV; λ_3 and λ_4 are the failure rates of lines L_1 and L_2; λ_5 and λ_6 are the failure rates of transformers 1 and 2; τ_3 and τ_4 are the repair times of lines L_1 and L_2; τ_5 and τ_6 are the repair times of transformers 1 and 2.

Second transformation.

$$\lambda_{eq_1} = \lambda_{1,2} + K_0(\lambda_3 + \lambda_4) = \lambda_{13} ; \quad (31)$$

$$\tau_{eq_1} = \frac{\lambda_{1,2} \cdot \tau_{1,2} + K_0(\lambda_3 + \lambda_4) \cdot \tau_3}{\lambda_{1,2} + K_0 \cdot (\lambda_3 + \lambda_4)} = \tau_{13} ; \quad (32)$$

$$\lambda_{eq_2} = \lambda_{3,5} . \lambda_{4,6} (\tau_{3,5} + \tau_{4,6}) = \lambda_{14} ; \quad (33)$$

$$\tau_{eq_2} = \frac{\tau_{3,5} . \tau_{4,6}}{\tau_{3,5} + \tau_{4,6}} = \tau_{14} , \quad (34)$$

where K_0 is the coefficient of the climatic conditions influence; $K_0(\lambda_3+\lambda_4)$ is the failure rate of the lines L_1 and L_2 simultaneously; τ_0 is the repair time of the two lines $\tau_0 = \tau_3 = \tau_4$.

Third transformation.

$$\lambda_{15} = \lambda_{13} + \lambda_{14} ; \quad (35)$$

$$\tau_{15} = \frac{\lambda_{13} \cdot \tau_{13} + \lambda_{14} \cdot \tau_{14}}{\lambda_{13} + \lambda_{14}} . \quad (36)$$

Finally, the expression of the probability of failure of the power supply system from two electric lines can be represented as follows:

$$Q = \tau_{15} \cdot \left(1 - e^{-\lambda_{15}}\right) / 8760 . \quad (37)$$

Second variant of the power supply system – from a single electric line and a turbogenerator.

First transformation.

$$\lambda_7 = \lambda_1 + \lambda_2 + \lambda_3 + \lambda_4 ; \quad \lambda_8 = \lambda_5 + \lambda_6 \quad (38)$$

$$\tau_7 = \frac{\lambda_1 \cdot \tau_1 + \lambda_2 \cdot \tau_2 + \lambda_3 \cdot \tau_3 + \lambda_4 \cdot \tau_4}{\lambda_1 + \lambda_2 + \lambda_3 + \lambda_4} ; \quad (39)$$

$$\tau_8 = \frac{\lambda_5 \cdot \tau_5 + \lambda_6 \cdot \tau_6}{\lambda_5 + \lambda_6} , \quad (40)$$

where $\lambda_1 - \lambda_4$ are the failure rate of the electrical post, overhead line, transformer and the circuit breaker 0.4 kV respectively; $\tau_1 - \tau_4$ are the failure rate of the turbogenerator and the circuit breaker 0.4 kV respectively; λ_5 and λ_6 are the failure rate of turbogenerator and the circuit breaker 0.4 kV respectively; τ_5 and τ_6 are the repair times of the turbogenerator and the circuit breaker 0.4 kV respectively.

Second transformation.

$$\lambda_7 = \lambda_7 \cdot \lambda_8 (\tau_7 + \tau_8) ; \quad \tau_9 = \frac{\tau_7 \cdot \tau_8}{\tau_7 + \tau_8} . \quad (41)$$

The expression of the probability of failure of the power supply system is:

$$Q = \tau_9 \cdot (1 - e^{-\lambda_9}) / 8760 . \quad (42)$$

Third variant of the power supply system – from two turbogenerators.

First transformation.

$$\lambda_5 = \lambda_1 + \lambda_2 ; \quad \lambda_6 = \lambda_3 + \lambda_4 , \quad (43)$$

$$\tau_5 = \frac{\lambda_1 \cdot \tau_1 + \lambda_2 \cdot \tau_2}{\lambda_1 + \lambda_2} ; \quad \tau_6 = \frac{\lambda_3 \cdot \tau_3 + \lambda_4 \cdot \tau_4}{\lambda_3 + \lambda_4} , \quad (44)$$

where λ_1, λ_3 and λ_2, λ_4 are the failure rate turbogenerator and the circuit breaker 0.4 kV respectively; τ_1, τ_3 and τ_2, τ_4 are the repair times of the turbogenerator and the circuit breaker 0.4 kV respectively.

Second transformation.

$$\lambda_7 = \lambda_5 \cdot \lambda_6 (\tau_5 + \tau_6) ; \quad \tau_7 = \frac{\tau_5 \cdot \tau_6}{\tau_5 + \tau_6} . \quad (45)$$

The expression of the probability of failure of the power supply system is:

$$Q = \tau_7 \cdot \left(1 - e^{-\lambda_7}\right) / 8760 . \quad (46)$$

The general formula of damage caused by accidental power system failures for all three variants is:

$$D = 1.08 \cdot P_M \cdot 8760 \cdot Q \cdot \varepsilon \cdot \beta_m \cdot \beta_q \cdot C_0 , \text{ DA.} \quad (47)$$

The Table 2 illustrates the reliability parameters of electrical equipment for different voltages.

Table 2

Reliability parameters of electrical equipment for different voltages

Electrical equipment	Failure rate λ, 1/year	MTBF, h	Repair time τ, h	MTTR, h
Airline (100 km)				
30 kV	2.2	0.454	5.6	0.178
60 kV	2.0	0.5	5.6	0.178
220 kV	1.4	0.714	6.5	0.153
Circuit breaker				
(6 –10) kV	0.005	200	10	0.1
30 kV	0.005	200	10	0.1
60 kV	0.005	200	10	0.1
220 kV	0.02	50	24	0.041
Transformer				
(6 –10) kV	0.023	43.478	70	0.014
30 kV	0.018	5.555	90	0.011
60 kV	0.02	50	100	0.01
220 kV	0.02	50	100	0.01
Turbogenerator				
0.4 kV	5.80	0.172	70	0.014

Graphical presentation of the calculation. The operating procedure for the calculation of the optimization algorithm of the power supply systems of the five compressor stations has wide limits by combining the different variants of the power supply system that may exist.

In our case, as an explanation, we are limited to three variants of the electrical supply system for two compression

stations, knowing that each compression station has two independent power stations (turbogenerators).

Figure 7 clearly, shows the graphic presentation of the calculation of the three variants of the electrical supply system for two compression stations.

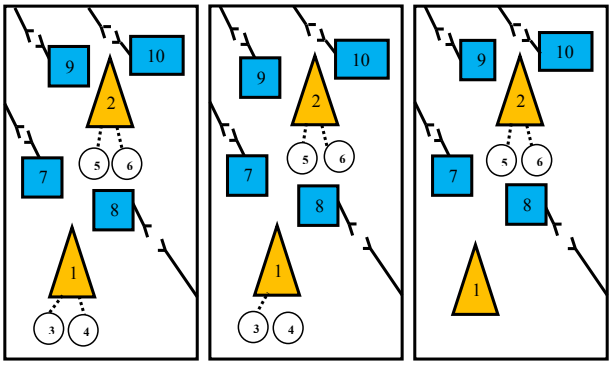

Fig. 7.Graphic presentation of the calculation

First variant. By keeping the local power supply system from two autonomous power plants of each compressor station, the calculation gave us the total expenses C_{t1}.

Second variant. By replacing a stand-alone power plant with a electric line, that is to say, power is supplied from a substation and a stand-alone power plant, the total expenditure which was found to be C_{t2} is lower than the total expenditure C_{t1} ($C_{t1} > C_{t2}$).

Third variant. The power supply to a compressor station is provided by two independent electric lines, which allowed us to obtain the total expenses as C_{t3} below the total expenses C_{t2} ($C_{t1} > C_{t2} > C_{t3}$), the variant of the most optimal power supply system with the minimum total expenditure ($C_t \rightarrow \min$).

Calculation procedure on the computer.

Initial data.

A. Expenditure calculation.

1. see if $A(i,j) = 1$
2. calculation of $L(i,j)$
3. see if $L(i,j) \le L_{cr}$
4. calculation of installation and operating expenditure for $L(i,j)$ (post $j \rightarrow CS_i$)
5. if $L(i,j) = 0$
6. calculation of operating and installation expenses for turbogenerators ($TA_j \rightarrow CS_i$).
7. if $A(i,j) = -1$
8. calculation of operating expenditure for the existing line (post $i \rightarrow$ post j)
9. calculation: $C_p(i,j) = \sum_{i=1}^{n}\sum_{j=1}^{m} C_p(i,j)$. (48)

B. Damage calculation.

1. if $A(i,j) = 1$
2. see if $K = 2$
3. calculation of damages for the two-line PSS.
4. see if $K = 1$
5. calculation of damage for the single-line PSS and a turbogenerator.
6. see if $K = 0$
7. calculation of the damage for the PSS with two turbogenerators
8. calculation: $D(i) = \sum_{i=1}^{5} D(i)$, (49)
9. sum total expenditure:

$$D(i,j) = \sum_{i=1}^{n}\sum_{j=1}^{m} C_P(i,j) + \sum_{i=1}^{5} D(i), \quad (50)$$

10. calculation of total expenditure for each variant according to the matrix (mathematical model of PSS chosen for the five (5) CS).
11. take the most optimal variant, the total expenditure of which will be minimal.

Conclusion.

This paper proposed a recent optimization technique based on the proposal of an algorithm combining two technical and economic aspects to help the operator to minimize the failures of the power supply systems directly influencing the reduction of the uptime of the turbocompressors (restart fuel and oil losses, etc.). In this study, we calculated the reliability parameters of three variants of the power supply system that were considered for compressor stations, from two electric lines, a single electric line, and a turbogenerator. Then, we calculated the damage. A graphical presentation by graph theory of this developed model is adequate.

From the calculation results, it can be concluded that currently taking into account the economic criterion and the initial data retained, the supply of electrical energy to the gas compression station «C» located at CHAIBA, is carried out from two autonomous sources, but from the point of view of reliability (technical criteria) or clearly sees that the power supply of the above-mentioned station, from two independent external lines is imposed.

From the results of the research, it can be said that the presented algorithm, developed in the FORTRAN programming language, greatly facilitates the calculation of the damage to the power system of any compressor station.

In the future, with the construction of new distribution stations near the gas compressor stations and the actual data, it can be seen that the variant of the supply system from two independent external lines is the most optimal. This allowed us to calculate the preventive power supply of two independent substations and impose the appropriate maintenance policies.

Conflict of interest. The authors declare that they have no conflicts of interest.

REFERENCES

1. Tikhomirova E. *Provision of electric power to CS of TGP, using renewable energy sources (on the example of wind turbines)*. Master of science thesis EGI, KTH, The Royal Institute of Technology, School of Industrial Engineering and Management, Stockholm, 2012, 86 p. Available at: https://www.diva-portal.org/smash/get/diva2:617506/FULLTEXT01.pdf (accessed 20.10.2020).

2. Ríos-Mercado R.Z., Borraz-Sánchez C. Optimization problems in natural gas transportation systems: A state-of-the-art review. *Applied Energy*, Jun. 2015, vol. 147, pp. 536-555. doi: https://doi.org/10.1016/j.apenergy.2015.03.017.

3. Luongo C., Gilmour B., Schroeder D. Optimization in natural gas transmission networks: A tool to improve operational efficiency. *Proceedings of the Third SIAM conference on optimization*, Boston, USA, 1989.

4. Turysheva A.V., Baburin S.V. Justification of power supply system's structure of oil and gas facilities using backup energy

sources with associated petroleum gas as the energy carrier. *International Journal of Applied Engineering Research*, 2016, vol. 11, no. 1, pp 749-755. Available at: https://www.researchgate.net (accessed 20.10.2020).
5. Kurz R., Lubomirsky M., Brun K. Gas Compressor Station Economic Optimization. *International Journal of Rotating Machinery*, vol. 2012, article number 715017, 9 p. doi: https://doi.org/10.1155/2012/715017.
6. Bansal R.C. Optimization methods for electric power systems: An overview. *International Journal of Emerging Electric Power Systems*, Jan. 2005, vol. 2, iss. 1, article number 1021. doi: https://doi.org/10.2202/1553-779x.1021.
7. Baburin S.V., Kovalchuk M.S. Analysis of power supply systems reliability for gas pumping compressor stations. *2018 IEEE Conference of Russian Young Researchers in Electrical and Electronic Engineering (EIConRus)*, Moscow and St. Petersburg, Russia, 2018, pp. 566-569. doi: https://doi.org/10.1109/eiconrus.2018.8317161.
8. Massim Y., Zeblah A., Benguediab M., Ghouraf A., Meziane R. Reliability evaluation of electrical power systems including multi-state considerations. *Electrical Engineering*, Aug. 2004, vol. 88, no. 2, pp. 109-116, doi: https://doi.org/10.1007/s00202-004-0262-2.
9. *Prévision de consommation d'électricité à moyen terme*. Direction de planification SONELGAZ, Juin 1984. (Fra).
10. *Military Handbook 338. Electronic Reliability Design Handbook*, October 1998. Available at http://everyspec.com/MIL-HDBK/MIL-HDBK-0300-0499/MIL-HDBK-338B_15041 (accessed 20.10.2020).
11. Villemeur A. *Sûreté de fonctionnement des systèmes industriels : fiabilité, facteurs humains, informatisation*. Paris: Eyrolles, 1988. (Fra).
12. Pages A. *Fiabilité des systèmes d'alimentation électrique*. Paris, 1980. (Fra).

Received 20.12.2020
Accepted 25.01.2020
Published 05.04.2021

Nedjem-Eddine Benchouia [1], *Ph.D., HDR,*
Mohamed Saaidia [2], *Ph.D.,*
[1] Department of Mechanical Engineering,
Mohamed-Cherif Messaadia University,
Souk Ahras mailbox 1553, Souk-Ahras, 41000, Algeria,
e-mail: n.benchouia@univ-soukahras.dz
[2] Department of Electrical Engineering,
Mohamed-Cherif Messaadia University,
Souk Ahras mailbox 1553, Souk-Ahras, 41000, Algeria,
e-mail: mohamed.saaidia@cu-soukahras.dz

Appendix 1 – Proposed program in FORTRAN code

```
! PSS SC Program
Dimension X(9),Y(9),W(11),V(11),pril(11,9),uam(11,9),
+upe(11 ,9),uen(11,9),d1(11,9),d(2),prixg(11,9),td30(9),
+tao30(9),tdl30(11,9),tdc30(11,9),taoc30(11,9),t30(2),
+s30(2),e30(2),d30(2),X30(2),h30(2),C30(2),
+prob(2)
Integer a(11,9)
Real l(11,9),lcr1
Data td30/0.,0., 0.,0., 0.5,0.5, 0.5,0.5,0.5/
+tao30/0.,0., 0.,0., 0.02,0.02,0. 02,0.02,0.02/
Data X/55.,55.,89.,89.,32.5,115.,118.,27.5,62.5/
+Y/62.5,62.5,97.5,97.5,82.5,82.,107.,161.5,152./
Data W/55.,89.,55.,55.,89.,89.,32.5,115.,118.,97.5,62.5/,
+V/62.5,97.5,62.5,62.5,97.5,97.5,82.5,82.,107.,161.5,152/
Data Pril1/20./,Pritr1/100./,Alp1/0.02/,ALP2/0.06/,
+ALP3/0.07/,prig/3500./,r01/0.77/,R02/0.64/,taom/5948./,
+delp/3.1/,delpc/18./,ch/0.7/,betm/0.97/,betq/0.94/,
+tdtr1/0.02/,tddis/0.002/,tdg/5.8/,taol1/5.6/,
+taodis/1.75/,taog/70./,pm/2214.24/,epsi/1./,u1/30./,
+s/1232.5/,u2/60./,c0/0.00055/,taotr1/90./,tdl1/2.2/
Data a/1,0,-1,0,0,0,0,0,0,0,0,0,0,0,-1,0,0,0,0,0,0,0,0,0,
+0,0,-1,0,0,0,0,0,0,0,0,0,0,0,-1,0,0,0,0,0,1,0,0,0,0,
+0,-1,0,0,0,0,0,-1,0,0,0,0,0,-1,0,0,0,0,0,0,0,0,0,0,-1,
+-1,0,0,0,0,0,0,0,0,0,0,0,-1,-1,0,1,0,0,0,0,0,0,0,0,
+-1/
Data lcr1/50./
Open (unit=15,file='bou.d',status='unknown')
J=1
6   do 4 i =1,2
If(a(i,j).eq.0) goto 4
l(i,j) = sqrt((x(j)-w(i))**2+(y(j)-v(i))**2)
if(l(i,j).eq.0.) goto 15
if(l(i,j).gt.lcr1) goto 4
pril(i,j)=pril1*l(i,j)+(pritr1)
uam(i,j)=(alp1*(pril1*l(i,j))+(alp2*pritr1))
uen(I,j)=0.2*uam(I,j)
upe(I,j)=(((s**2/u1**2)*r01*l(I,j)*taom)+
+((delp*8760)+(delpc*ch**2*taom)))*c0
d1(I,j)=0.12*pril(I,j)+uam(I,j)+uen(I,j)+upe(I,j)
write(15,12)i,j,d1(I,j)
goto 4
15  prixg(I,j)=prig
Uam(I,j) = alp3*prixg(I,j)
Uen(I,j)=0.2*uam(I,j)
d1(I,j)=0.12*prixg(I,j)+uam(I,j)+uen(I,j)
write(15,12)I,j,d1(I,j)
12  format(3x,»d1(«,i2,»,»,i2,»)= «,e11.4)
4   continue
J=j+1
If(j.le.9)goto 6
J=1
3   do 7 i=3,11
If(a(I,j).eq.0) goto 7
L(I,j)=sqrt((x(j)-w(i))**2+(y(j)-v(i))**2)
D1(I,J)=((s**2/60**2)*r02*l(I,j)*taom)*c0
Write(15,12)I,j,d1(I,j)
13   format(3X,»d1(«,i2,»,»,i2»,)=«e11.4)
7    continue
J=j+1
If (j.le.9) goto 3
I=1
80   k=0
Do 10 j=1,9
If(a(I,j).ne.1) goto 10
K=k+1
If(L(I,j).ne.0) goto 10
K=K-1
10   continue
If(k.eq.2.) goto 14
If(k.eq.1) goto 16
If(k.eq.0) goto 18
14   do 20 j=1,9
If(a(I,j).ne.1) goto 20
If(l(I,j).gt.lcr1) goto 20
If(l(I,j).eq.0) goto 20
tdl30(I,j)=tdl1*l(I,j)/100
tdc30(I,j)=tdl30(I,j)+tdtr1+tddis
taoc30(I,j)=((tdl30(I,j)*taol1)+(tdtr1*taotr1)+
+(tddis*taodis))/tdc30(I,J)
20   continue
T30(i)=0
S30(i)=0
E30(i)=1
D30(i)=1
X30(i)=1
H30(i)=1
C30(i)=0
```

```
Do 30 J=1,9
If(a(I,j).ne.1) goto 30
If (l(I,j).gt.lcr1) goto 30
If (l(I,j).eq.0) goto 30
t30(i)=t30(i)+tdl30(I,j)
e30(i)=e30(i)*td30(j)
s30(i)=s30(i)+tao30(j)
d30(i)=d30(i)*tao30(j)
c30(i)=c30(i)+taoc30(I,j)
h30(i)=h30(i)*taoc30(I,j)
x30(i)=x30(i)*tdc30(I,j)
30   continue
Td9 =e30(i)*s30(i)/8760
Td34=0.2*t30(i)
Td12=td9+td34
Tao9=d30(i)/s30(i)
Tao12=((td9*tao9)+(td34*tao34))/td12
Td13=x30(i)*c30(i)/8760
Tao13=h30(i)/c30(i)
Td14=td12+td13
Tao14=((td12*tao12)+(td13*tao13))/td14
Prob(i)=(tao14*(1-exp(-td14)))/8760
D(i)=1.08*pm*8760*prob(i)*epsi*betm*betq*c0
Write(15,26) I,d(i)
26   format(3x',d(',i1,')=',e11.4)
Goto 100
16   do 60 j=1,9
If(a(I,j).ne.1) goto 60
If(l(I,j).gt.lcr1) goto 60
If(l(I,j).eq.0) goto 60
Tdl30(I,j)=tdl1*l(I,j)/100
Tdc30(I,j)=tdl30(I,j)+td30(j)+tdtr1+tddis
Taoc30(I,j)=((tdl30(I,j)*taol1)+(td30(j)*tao30(j))+
+ (tdr1*taotr1)+(tddis*taodis))/tdc30(I,j)
60   continue
Do 107 j=1,9
If(a(I,j).ne.1) goto 107
If(l(I,j).gt.lcr1) goto 107
If(l(I,j).eq.0) goto 107
Td8=tdg+tddis
Tao8=((tdg*taog)+(tddis*taodis))/td8
Td9=(tdc30(I,j)*td8)*(taoc30(I,j)+tao8)/8760
Tao9=taoc30(I,j)*tao8/(taoc30(I,j)+tao8)
107   continue
Prob(i)=(tao9*(1-exp(-td9)))/8760
D(i)=1.08*pm*8760*prob(i)*epsi*betm*betq*c0
Write(15,26)I,d(i)
Goto 100
18   td5=tdg+tddis
Tao5=(tdg*taog+tddis*taddis)/td5
Td7=(td5**2)*(tao5+tao5)/8760
Tao7=tao5/2
Prob(i)=(tao7*(1-exp(-td7)))/8760
D(i)=1.08*pm*8760*prob(i)*epsi*betm*betq*c0
Write(15,26) I,d(i)
100  i=i+1
If(i.le.2) goto 80
Close (unit =15)
Stop
End
```

Result

```
d1( 1, 1)=  0.7140E+03
d1( 1, 5)=  0.1281E+06
d1( 2, 6)=  0.1288E+06
d1( 3, 1)=  0.0000E+00
d1( 4, 2)=  0.0000E+00
d1( 5, 3)=  0.0000E+00
d1( 6, 4)=  0.0000E+00
d1( 7, 5)=  0.0000E+00
d1( 8, 6)=  0.0000E+00
d1( 8, 7)=  0.2224E+05
d1( 9, 7)=  0.0000E+00
d1(10, 8)=  0.6184E+05
d1(11, 8)=  0.3204E+05
d1(11, 9)=  0.0000E+00
,d(1)= 0.2011E+00
,d(2)= 0.2011E+00
```

How to cite this article:
Benchouia N., Saaidia M. Optimization and reliability of the power supply systems of a compressor station. *Electrical Engineering & Electromechanics*, 2021, no. 2, pp. 54-63. **doi: 10.20998/2074-272X.2021.2.08.**

UDC 621.3 **doi: 10.20998/2074-272X.2021.2.09**

M.F. Mehdi, A. Ahmad, S.S. Ul Haq, M. Saqib, M.F. Ullah

DYNAMIC ECONOMIC EMISSION DISPATCH USING WHALE OPTIMIZATION ALGORITHM FOR MULTI-OBJECTIVE FUNCTION

Introduction. *Dynamic Economic Emission Dispatch is the extended version of the traditional economic emission dispatch problem in which ramp rate is taken into account for the limit of generators in a power network.* ***Purpose.*** *Dynamic Economic Emission Dispatch considered the treats of economy and emissions as competitive targets for optimal dispatch problems, and to reach a solution it requires some conflict resolution.* ***Novelty.*** *The decision-making method to solve the Dynamic Economic Emission Dispatch problem has a goal for each objective function, for this purpose, the multi-objective problem is transformed into single goal optimization by using the weighted sum method and then control/solve by Whale Optimization Algorithm.* ***Methodology.*** *This paper presents a newly developed metaheuristic technique based on Whale Optimization Algorithm to solve the Dynamic Economic Emission Dispatch problem. The main inspiration for this optimization technique is the fact that metaheuristic algorithms are becoming popular day by day because of their simplicity, no gradient information requirement, easily bypass local optima, and can be used for a variety of other problems. This algorithm includes all possible factors that will yield the minimum cost and emissions of a Dynamic Economic Emission Dispatch problem for the efficient operation of generators in a power network. The proposed approach performs well to perform in diverse problem and converge the solution to near best optimal solution.* ***Results.*** *The proposed strategy is validated by simulating on MATLAB® for 5 IEEE standard test system. Numerical results show the capabilities of the proposed algorithm to establish an optimal solution of the Dynamic Economic Emission Dispatch problem in a several runs. The proposed algorithm shows good performance over the recently proposed algorithms such as Multi-Objective Neural Network trained with Differential Evolution, Particle swarm optimization, evolutionary programming, simulated annealing, Pattern search, multi-objective differential evolution, and multi-objective hybrid differential evolution with simulated annealing technique.* References 17, tables 3, figures 5.

Key words: **whale optimization algorithm, dynamic economic emission dispatch, ramp rate, multi-objective problem, economic emission.**

Вступ. *Динамічна економна диспетчеризація викидів – це розширена версія традиційної задачі економної диспетчеризації викидів, в якій враховується коефіцієнт нарощування для межі генераторів в енергомережі.* ***Призначення.*** *Динамічна економна диспетчеризація викидів розглядала питання економії та викидів як конкурентні цілі для оптимальних задач диспетчеризації, і для розв'язання задачі потрібне певне вирішення конфліктів.* ***Новизна.*** *Метод прийняття рішень для розв'язання задачі динамічної економної диспетчеризації викидів має мету для кожної цільової функції, для цього багатоцільова задача трансформується в оптимізацію однієї цілі за допомогою методу зваженої суми, а потім контролюється/розв'язується за допомогою алгоритму оптимізації китів.* ***Методологія.*** *У цій роботі представлена нещодавно розроблена метаевристична методика, заснована на алгоритмі оптимізації китів для розв'язання задачі динамічної економної диспетчеризації викидів. Основним натхненням для цієї методики оптимізації є той факт, що метаевристичні алгоритми стають популярними з кожним днем завдяки своїй простоті, відсутності вимог до інформації про градієнт, легкості обходу локальних оптимумів та можливості бути використаними для ряду інших задач. Цей алгоритм включає в себе всі можливі фактори, які забезпечать мінімальні вартість та викиди задачі динамічної економної диспетчеризації викидів для ефективної роботи генераторів в енергомережі. Запропонований підхід добре працює для розв'язання задач і наближення рішення до найкращого оптимального.* ***Результати.*** *Запропонована стратегія перевірена шляхом моделювання на MATLAB® для 5 стандартних тестових систем IEEE. Чисельні результати демонструють можливості запропонованого алгоритму для встановлення оптимального рішення задачі динамічної економної диспетчеризації викидів за кілька прогонів. Запропонований алгоритм демонструє хорошу ефективність порівняно з нещодавно запропонованими алгоритмами, такими як багатоцільова нейронна мережа, навчена з використанням диференціальної еволюції, оптимізація рою частинок, еволюційне програмування, імітаційний відпал, пошук за шаблоном, багатоцільова диференціальна еволюція та багатоцільова гібридна диференціальна еволюція з імітаційним методом відпалу.* Бібл. 17, табл. 3, рис. 5.

Ключові слова: **алгоритм оптимізації китів, динамічна економна диспетчеризація викидів, швидкість наростання, багатоцільова задача, економна емісія.**

1. Introduction. Power plants based on fossil fuel emit health hazardous gases into the surrounding environment. Air pollution due to these gases can not only affect human life but can compromise the animals and birds life. It also damages visibility, material quality, and causing global warming [1]. With increasing environmental concern, consumer demands high quality power with safe electricity, at lowest possible rates and with lowest possible pollution. Dynamic Economic Emission Dispatch (DEED) provide a solution to these problem by scheduling the renewable and backup power sources based on the forecast load demand to reduce cost and emission of the operating generator [2, 3].

DEED is dynamic in nature due to non-linear nature of power system and its loads. This non-linear or dynamic problem is normally solved by discretizing the whole dispatch time interval into smaller time interval in which the load is serve as constant and in steady state. To control and achieve the lowest cost and emission ratio, the individual time interval must be dispatched so that to minimize the cost and emission at that time subjected to static constraint with additional time limit known as dynamic constraint. DEED is serve as an accurate method to solve economic dispatch (ED) problem but at same time it is the most difficult method due to lengthy measurements [4].

Nowadays, meta-heuristic optimization algorithms are gaining popularity in engineering and technology field

due to its simplicity and easy to implement concept. No gradient information is required for their implementation. Not only can they circumvent regional optimizations, but they can also be applied to numerous fields [5].

In recent years, probabilistic search algorithms e.g. genetic algorithms (GA), simulated annealing (SA), and evolutionary programming (EP) are efficiently utilized to solve power network optimization issues. These methods aren't based on 1st and 2nd differences in the objective function of optimized problem [6, 7].

1. Literature review. In [8] solved the multi-purpose economic emission dispatch problem using a new technique called Dance Bee Colony with dynamic step size taking into account the valve point effect. The proposed algorithm was applied to the 6 unit and 40 unit systems, respectively. He observed that the proposed method could also solve the combined economic emission dispatch problem. In [9] studied DEED, which contains uncertainties in the development process. In addition to the classic dynamic economic emissions dispatch factor, reliability and efficiency constraints have been specifically considered to contain the disturbances of uncertainty. As a result, a fine and reserve emission function has been added to the multipurpose function as well as a fine and reserve cost function. To obtain quantitative results, we discussed the characterization of various sources of uncertainty based on statistical theory, and this optimization problem was solved numerically by an improved particle cluster optimization algorithm. In [10] announced the multi-elite guided hybrid differential evolution using a simulated annealing technique for dynamic economic emission dispatch (MOHDE-SAT). This incorporates orthogonal initialization methods into differential evolution, expanding population diversity early in the population.

In addition, we can use modified mutation operators and archive preservation mechanisms to control the rate of convergence, and adaptively monitor population diversity as evolution progresses using simulated annealing techniques and entropy diversity methods to adequately avoid early convergence problems.

Applied to 5 and 10 unit systems. In [11] versatile DEED using the PSO variant was announced. Tested PSO variants include standard PSO (SPSO), worst-case avoidance PSO (PSO AWL), and progressively increasing directional neighbors (PSO GIDNs). Researchers tested the performance of various variants of PSO AWL against variants of SPSO for DEED problems and concluded that PSO AWL outperformed SPSO for all implemented topologies.

Applied to 10 units. In 2018 a new multipurpose neural network trained with MONNDE (Differential Evolution) was presented in [12]. The MONNDE framework applies to the problem of Dynamic Economic Emission Dispatch (DEED) and is equally optimal compared to other state-of-the-art algorithms in terms of 24-hour cost and emissions. Researchers also compared the performance of fully connected and partially connected networks and found that dynamically optimizing the topology of a neural network performed better in an online learning environment than simply optimizing the network weights.

It is clear from the literature that the problem of economic emission dispatch is solved with many classical, meta-heuristic and hybrid techniques.

Another newly developed technique called Whale Optimization Algorithm (WOA) is proposed. This method has not yet been implemented in the DEED problem, but it could be a very attractive idea to use this algorithm for the DEED problem. Our focus is on applying WOA to standard test systems.

This paper develops efficient and reliable evolutionary programming based on WOA to solve the DEED problem. Here the objective functions, namely cost and emissions, are modeled. The proposed strategy is validated by simulating MATLAB® against 5 IEEE standard test system. Numerical results for a sample test system are presented to demonstrate the capabilities of the proposed approach to create a well-distributed Pareto optimal solution of the dynamic economic emission dispatch problem in a single run. The proposed algorithm is also compare with the recently proposed algorithms such as Multi-Objective Neural Network trained with Differential Evolution (MONNDE), particle swarm optimization (PSO), evolutionary programming (EP), simulated annealing (SA), Pattern search (PS), multi-objective differential evolution (MODE), and multi-objective hybrid differential evolution with simulated annealing technique (MOHDE-SAT).

2. Problem formulation. The DEED problem is flexible mathematical programming problem that consists of goals and constraints to achieve lowest cost and emission at a time. To achieve the above goal, the system equality and inequality constraints should be met. Steps involving in DEED problem are given below.

2.1. Objectives function of DEED problem. Objectives function of DEED problem consists of fuel cost and emission functions.

2.1.1 Economy. The cost function F_1 shows the hourly cost of power generators and is given as:

$$F_1 = \sum_{i=1}^{N}\sum_{m=1}^{N} F_i\left(P_i\right), \tag{1}$$

where N refers to power generators numbers.

Equation (2) shows the cost hourly non-convex cost function of power generators:

$$\begin{aligned} F_i\left(P_i\right) &= a_i + b_i P_i + c_i P_i^2 + \\ &+ \left| e_i \cdot \sin\left(f_i\left(P_{\min,i} + P_m\right)\right)\right|, \end{aligned} \tag{2}$$

where m is the present hour; a_i, b_i, c_i, e_i and f_i are all constant factors related with each generator i; $P_{\min,i}$ is the minimum power output of a generator i at m time and $P_{\min}$ is the minimum power of a generator.

2.1.2 Emission. The emission function F_2 that determine the total hazardous pollutant produce due to operation of all generators per hours as shown in equation:

$$F_2 = \sum_{i=1}^{N}\sum_{m=1}^{N} E_i\left(P_i\right), \tag{3}$$

where the emission function E determines the amount of injurious pollutants produce by power generators for 24 hours.

Equation (4) shows the harmful pollutants of non-convex function

$$E_i(P_i) = \alpha_i + \beta_i P_i + \gamma_i P_i^2 + \delta_i \exp(\lambda_i P_i), \quad (4)$$

where α_i, β_i, γ_i, δ_i and λ_i are the emission constant factors related with each generator *i*.

2.2 Constraints. DEED constraint consists of equality and inequality constraints.

2.2.1 Balance Constraints. All solution is substance to real power equality constraint. Balance constraint is define as the total output power must be equal to summation of actual power demand and losses due to transmission lines as shown in equations (5) and (6)

$$\sum_{i=1}^{N} P_i = P_{om} + P_{lm}, \quad (5)$$

$$P_{lm} = \sum_{i=1}^{n}\sum_{j=1}^{n} P_i B_{i,j} P_j + \sum_{i=1}^{n} B_{i0} P_i + B_{00}, \quad (6)$$

where $B_{i,j}$, B_{i0} and B_{00} are the loss coefficients of generators.

2.2.2 Inequality constraints.

2.2.2.1 Operating limit for each power generator. It determines the possible upper and lower power output of each generator in a network. The operating limits for each generator are defined as:

$$P_i^{\min} \le P_{im} \le P_i^{\max}, \quad (7)$$

where $P_i^{\max}$ and $P_i^{\min}$ are the maximum and minimum power output of each generator respectively.

2.2.2.2 Ramp rate limits of generating unit. The ramp limits of any generator determine the increase or decrease of maximum allowed output power between specific two limit steps. It can be define by follow equations:

$$P_{im} - P_{i(m-1)} \le UR_i, \quad (8)$$

$$P_{i(m-1)} - P_{im} \le DR_i, \quad (9)$$

where UR_i is the up ramp limit of a generator while DR_i are down ramp limit for a generator.

3. Principle of Whale Optimization Algorithm. WOA is inspire from the humpback whale hunting, which is also called bubble net feeding. This algorithm emphasizes the method of intelligent hunting mechanism of that particular whale. They hunt in a groups (size up to 12 whales), while the group leader is finding the group of fish to hunt [13]. Figure 1 shows the Bubble-net feeding behavior of humpback whales to hunt small fishes.

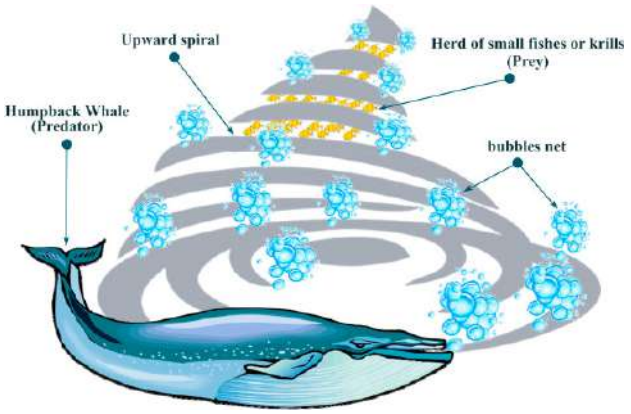

Fig. 1. Bubble-net feeding behavior of humpback whales [14]

The group of humpback whale goes under water and start to blow bubble while leader whale create larger size bubble in shape of «9». The fishes trapped in 9 shape trap due to its irregular swimming. Now the group of whale comes out with their mouths open and start hunting the trapped fishes inside the spiral bubbles. This technique of feeding is the unique behavior of this particular whale. In this research work, the bubble feed mechanism is modeled and implemented for solving the DEED problem.

The WOA approach starts with a function containing set of random solutions. The search agent update its position or location at each iteration based on randomly selected searches or best solution obtained. An «*a*» parameter is used in this method, whose value is normally reduced from 2 into 0 to achieve exploration and its utilization. Their value is adjusted every time to achieve best possible solution, finally the WOA is terminated when the solution meet the desire criteria.

4. Proposed whale optimization algorithm. The WOA is based on humpback whale hunting technology. Whales are mostly considered predators. Their favorite prey is hunting small group of fishes. The best thing about the humpback whale is their method of preying.

WOA algorithm involves steps such as encircling prey, bubble net feeding method, exploration phase and finally its implementation.

4.1 Encircling prey. Humpback whales can identify the position if prey and encircle them. Usually the location of optimal design is known, so the WOA algorithm that the current position is the best solution of targeted prey. After that starts to search for other best solution. If new best solution fined then the previous one updated with new best search agent. The encircling prey process can be expressed by equations:

$$\vec{D} = \left| \vec{C}\overrightarrow{X^*}(t) - \vec{X}(t) \right|;, \quad (10)$$

$$\vec{X}(t+1) = \overrightarrow{X^*}(t) - \vec{A}\vec{D}, \quad (11)$$

where the term *t* shows the up-to-date iteration; $\vec{A}$ and $\vec{C}$ are constant vectors, $\overrightarrow{X^*}$ is the position vector of the best solution obtained up-to-dated; $\vec{X}$ is the location vector.

It is important that $\overrightarrow{X^*}$ should be updated in each iteration if there is a better solution.

The vectors $\vec{A}$ and $\vec{C}$ are considered as shown in equations:

$$\vec{A} = 2\vec{a}\cdot\vec{r}, \quad (12)$$

$$\vec{C} = 2\vec{r}, \quad (13)$$

where vector $\vec{a}$ is linearly decreased from 2 to 0 in individual iterations (both in exploration and exploitation phases) and $\vec{r}$ is a random vector in [0, 1].

4.2 Exploitation phase. It is also called Bubble-net attacking method. This step consists of two processes.

4.2.1 Shrinking encircling mechanism. Shrinking encircling mechanism is accomplished by reducing the value of operator $\vec{a}$. This behavior is achieved by decreasing the value of $\vec{a}$. Due to this $\vec{A}$ will also

decreased in fact. $\vec{A}$ is an interval $[-\vec{a}, \vec{a}]$ having random value between $\pm\vec{a}$. The new location of search agent is selected between reference location of agent and location of present best agent.

4.2.2 Spiral updating position. The spiral position is lie between the whale position and its prey that causes the helix shaped movement of whale as shown in follow equation:

$$\vec{X}(t+1) = \vec{D'}\, e^{b\cdot l} \cos(2\pi l) + \overrightarrow{X^*}(t), \quad (14)$$

where $\vec{D'} = \left|\overrightarrow{X^*}(t) - \vec{X}(t)\right|$ and indicates the distance of the *i*-th whale to the prey (best solution obtained so far); *b* is a constant for defining the shape of the logarithmic spiral; *l* is a random number in [−1, 1].

Humpback whales swim around the prey within a shrinking circle and along a spiral-shaped path simultaneously. The mathematical model spiral behavior has a probability of 50 % because the value of operator $\vec{a}$ decide whether the movement will be circular or spiral. Follow equations shown this spiral behavior:

$$\vec{X}(t+1) = \overrightarrow{X^*}(t) - \vec{A}\vec{D} \quad if \quad P < 0.5, \quad (15)$$

$$\vec{X}(t+1) = \vec{D'}\, e^{b\cdot l} \cos(2\pi l) + \overrightarrow{X^*}(t) \quad if \quad P \geq 0.5, \quad (16)$$

where *P* is a random number in [0, 1].

In addition to the bubble-net method, the humpback whales search for prey randomly.

4.3 Search for prey (exploration phase). This is an exploration phase where humpback whales randomly search for each other position. So, $\vec{A}$ having random value of greater or less than ±1 forces the search agent to move far from reference position of reference whale. The exploration phase in this case can be calculated by follow equations:

$$\vec{D} = \left|\vec{C}\vec{X}_{rand} - \vec{X}\right|, \quad (17)$$

$$\vec{X}(t+1) = \vec{X}_{rand} - \vec{A}\vec{D}. \quad (18)$$

In the exploration phase according to a randomly chosen search agent instead of the best search agent found so far.

4.4 Implementation of WOA. The implementation of WOA is represented through flow chart in Fig. 2.

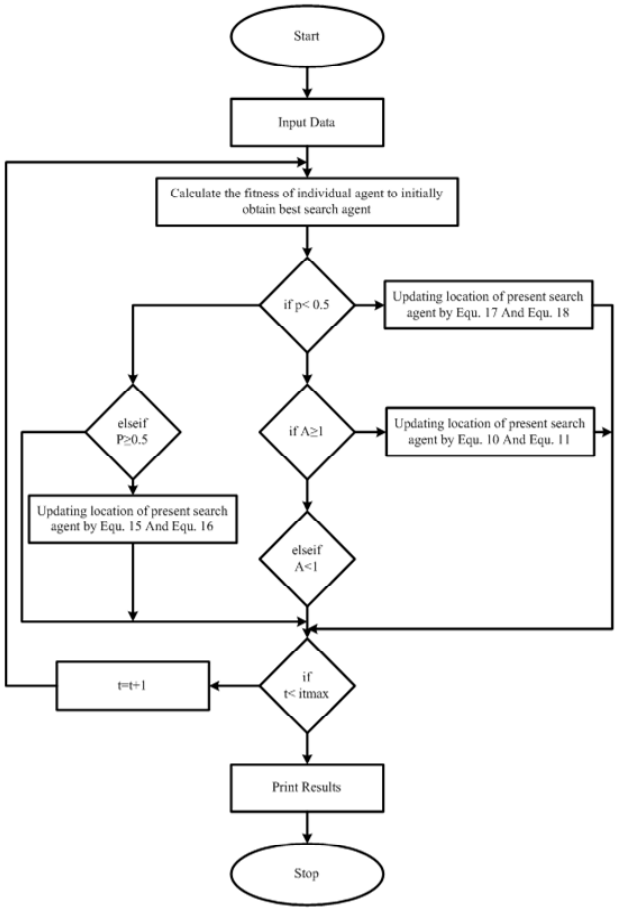

Fig. 2. The flowchart of proposed WOA

5. The simulation of the proposed multi-objective algorithm. The analyses were performed including minimum cost and emission ratio for operation of generators in a power network to show the improved performance of proposed algorithm. Furthermore, the effectiveness of proposed algorithm is checked by comparing with recently proposed algorithms such as MONNDE, PSO, EP, SA, PS, MODE, and MOHDE-SAT. All the analysis were done using MATLAB® (2018 Version) on an Intel (R) Core (TM) i5-2520M processor 2.50 GHz with a RAM 4.00 GB. Subsequent sections show the test system parameters and results after analysis.

5.1 Test system and its parameters. The proposed algorithm is tested on IEEE 5 units. The parameter of IEEE 5 units is shown in Table 1.

Table 1

Test System 1: 5 units IEEE data

Unit	P_{min}, MW	P_{max}, MW	*UR*, MW/h	*DR*, MW/h	*a*, $/h	*b*, $/MWh	*c*, $/MW^2h	*e*, rad/MW	*f*, lb/h	*α*, lb/MWh	*β*, lb/MWh	*γ*, b/MW^2h	*δ*, lb/h	*λ*, 1/MW
1	10	75	30	30	25	2.0	0.0080	100	0.042	80	–0.805	0.0180	0.6550	0.02846
2	20	125	30	30	60	1.8	0.0030	140	0.040	50	–0.555	0.0150	0.5773	0.02446
3	30	175	40	40	100	2.1	0.0012	160	0.038	60	–1.355	0.0105	0.4968	0.02270
4	40	250	50	50	120	2.0	0.0010	180	0.037	45	–0.600	0.0080	0.486	0.01948
5	50	300	50	50	40	1.8	0.0015	200	0.035	30	–0.555	0.0120	0.5035	0.02075

5.2 Results and comparisons. Table 2 shows the best fuel cost and emission for 24 hours for given load. The value of P1-P5 is selected by WOA such that load demand is fulfilled and give best fuel cost and emission result.

The 5 units test system is simulated for 8 trails having 500 search agents for 100 iterations. Table 3 presents the best cost, best emission and total cost-emission against 0.5 weight for 5 units. The results shown

in Table 3 are obtained from MONNDE, PSO, EP, SA, PS, MODE, MOHDE-SAT and proposed technique. The percentage change of other techniques with respect to proposed algorithm shows the effectiveness of proposed WOA. The proposed WOA has 4.94 % better performance than MONNDE, 8.8 % than PSO, 6.85 % than EP, 6.9 % than SA, 2.35 % than PS, 0.218 % than MODE, and 1.411 % than MOHDE-SAT.

Table 2

DEED results for 24 hrs

Load	Hour	P1	P2	P3	P4	P5	Fuel Cost	Emission
410	1	17.70	106.91	112.46	40	136.54	1317.87	510.62
435	2	45.71	98.84	118.13	40	136.30	1438.52	505.75
475	3	75	103.50	119.50	40	141.74	1515.83	579.21
530	4	75	98.79	127.53	89.81	144.58	1847.63	610.53
558	5	75	103.41	118.83	125.94	141.13	1697.07	643.38
608	6	75	98.51	130.10	168.47	143.39	2038.01	735.64
626	7	75	100.18	114.38	205.46	139.05	1832.18	806.98
654	8	75	102.71	133.92	209.16	141.95	2005.68	862.69
690	9	75	108.91	166.54	208.41	140.79	2153.24	944.19
704	10	73.88	106.36	171.88	209.76	152.17	2226.74	989.75
720	11	75	102.64	174.99	227.19	150.71	2329.29	1048.01
740	12	75	98.54	172.96	211.59	192.96	2380.45	1142.23
704	13	75	117.91	172.33	204.43	144.36	2261.61	985.77
690	14	75	104.04	166.28	213.28	141.05	2143.43	946.84
654	15	75	99.92	140.69	205.44	141.66	2037.19	854.35
580	16	75	99.24	111.07	155.44	146.10	1886.79	691.40
558	17	75	105.60	118.75	126.29	138.68	1709.21	642.50
608	18	75	101.05	126.35	168.89	144.21	2038.31	739.96
654	19	75	96.31	142.14	211.06	138.20	2023.64	856
704	20	75	113.52	171.41	211.85	142.31	2209.86	987.26
680	21	75	93.37	169.87	211.95	139.17	2092.81	918.93
605	22	75	105.93	129.87	161.95	139.68	2043.15	729.03
527	23	59.21	94.35	113.33	124.72	141.03	1615.60	583.67
463	24	45.06	97.89	111.04	74.72	138.70	1631	513.30
14577							**46475.10**	**18827.99**

Table 3

Performance comparison of WOA with other algorithms

Technique	Best cost ($)	Best emission (lbs)	Total (0.5 weight)	Change % w.r.t WOA
MONNDE [12]	49135	18233	33684.24	4.94
PSO [15]	50893	20163	35528	8.80
EP [16]	48628	21154	34891	6.85
SA [10]	48621	21188	34904.5	6.90
PS [17]	47911	18927	33419	2.35
MODE [10]	47330	18116	32723	0.218
MOHDE-SAT [10]	48214	18011	33112.5	1.411
Proposed WOA	46475.09	18827.98	32651.53	–

Figure 3 shows the graphical comparison of total cost and emission of proposed algorithms and other algorithms for 5 units. This clearly shows that the proposed WOA has the minimum total cost and emission than other algorithms.

Percentage improvement of proposed WOA with respect to other algorithms is shown in Fig. 4.

Figure 5 shows the variation of best cost among 8 trails (500 search agent and 100 iterations). Total cost and emission for each trail is 32761.39457, 32691.25187, 32870.03513, 32843.87755, 32824.84763, 33220.30359, 32651.54342, and 32745.05286, respectively. The best cost and emission is obtain at trail 7, which is 32651.54342.

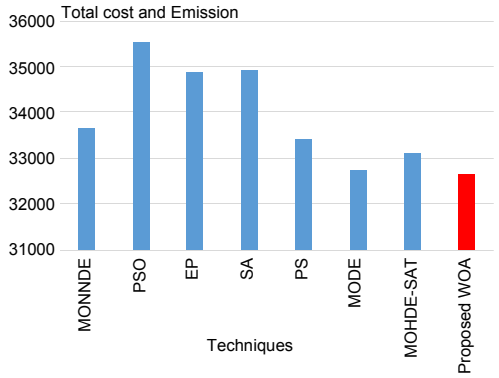

Fig. 3. Graphical comparison of total cost and emission vs. techniques

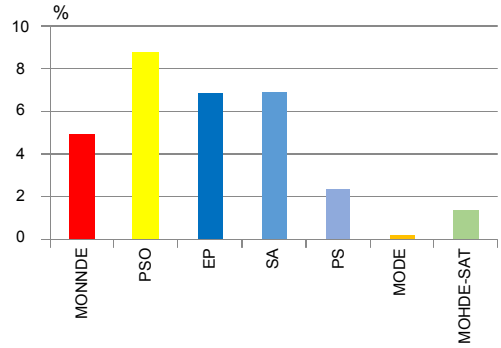

Fig. 4. Percentage improvement of proposed WOA vs. other techniques

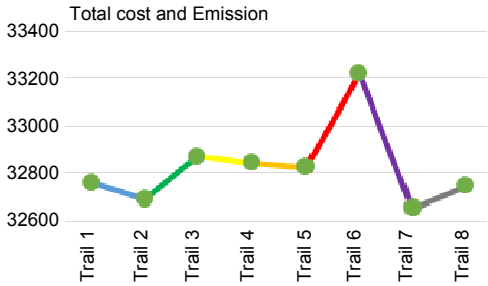

Fig. 5. Variation of best cost among 8 trails

Conclusion.

This paper presents a newly developed metaheuristic technique based on Whale Optimization Algorithm to solve the Dynamic Economic Emission Dispatch problem. The main inspiration for this optimization method is the fact that Metaheuristic algorithms are easy to implement, no gradient information requirement, easily bypass local optima, and can be used for a variety of other problems. The proposed strategy is validated by simulating on MATLAB® for 5 IEEE standard test system. Numerical results for the 5 IEEE test system are presented to show the capabilities of the proposed algorithm to establish an optimal solution of the Dynamic Economic Emission Dispatch problem in a several runs. The proposed Whale Optimization Algorithm for 5 unit has 4.94 % better performance than Multi-Objective Neural Network trained with Differential Evolution, 8.8 % than Particle swarm optimization, 6.85 % than evolutionary programming, 6.9 % than simulated annealing, 2.35 % than Pattern search, 0.218 % than

multi-objective differential evolution, and 1.411 % than multi-objective hybrid differential evolution with simulated annealing technique.

Conflict of interest. The authors declare that they have no conflicts of interest.

REFERENCES

1. Zou Y., Zhao J., Ding D., Miao F., Sobhani B. Solving dynamic economic and emission dispatch in power system integrated electric vehicle and wind turbine using multi-objective virus colony search algorithm. *Sustainable Cities and Society*, 2021, vol. 67, p. 102722. doi: https://doi.org/10.1016/j.scs.2021.102722.

2. Zare M., Narimani M.R., Malekpour M., Azizipanah-Abarghooee R., Terzija V. Reserve constrained dynamic economic dispatch in multi-area power systems: An improved fireworks algorithm. *International Journal of Electrical Power & Energy Systems*, 2021, vol. 126, part A, p. 106579. doi: https://doi.org/10.1016/j.ijepes.2020.106579.

3. Ahmed W., Sheikh J.A., Kouzani A.Z., Mahmud M.A.P. The Role of Single End-Users and Producers on GHG Mitigation in Pakistan – A Case Study. *Sustainability*, 2020, vol. 12, no. 20, p. 8351. doi: https://doi.org/10.3390/su12208351.

4. Qian S., Wu H., G Xu. An improved particle swarm optimization with clone selection principle for dynamic economic emission dispatch. *Soft Computing*, 2020, vol. 24, no. 20, pp. 15249-15271. doi: https://doi.org/10.1007/s00500-020-04861-4.

5. Azizivahed A., Arefi A., Naderi E., Narimani H., Fathi M., Narimani M.R. An Efficient Hybrid Approach to Solve Bi-objective Multi-area Dynamic Economic Emission Dispatch Problem. *Electric Power Components and Systems*, 2020, vol. 48, no. 4-5, pp. 485-500. doi: https://doi.org/10.1080/15325008.2020.1793830.

6. Wu C., Jiang P., Sun Y., Zhang C., Gu W. Economic dispatch with CHP and wind power using probabilistic sequence theory and hybrid heuristic algorithm. *Journal of Renewable and Sustainable Energy*, 2017, vol. 9, no. 1, p. 013303. doi: https://doi.org/10.1063/1.4976144.

7. Zhang Y., Liu K., Liao X., Qin L., An X. Stochastic dynamic economic emission dispatch with unit commitment problem considering wind power integration. *International Transactions on Electrical Energy Systems*, 2018, vol. 28, no. 1, p. e2472. doi: https://doi.org/10.1002/etep.2472.

8. Hadji B., Mahdad B., Srairi K., Mancer N. Multi-objective economic emission dispatch solution using dance bee colony with dynamic step size. *Energy Procedia*, 2015, vol. 74, pp. 65-76. doi: https://doi.org/10.1016/j.egypro.2015.07.524.

9. Jin J., Zhou D., Zhou P., Guo X., Sun Z. Modeling for dynamic economic emission dispatch under uncertainty. *Electric Power Components and Systems*, 2015, vol. 43, no. 14, pp. 1630-1643. doi: https://doi.org/10.1080/15325008.2015.1050613.

10. Zhang H., Yue D., Xie X., Hu S., Weng S. Multi-elite guide hybrid differential evolution with simulated annealing technique for dynamic economic emission dispatch. *Applied Soft Computing*, 2015, vol. 34, pp. 312-323. doi: https://doi.org/10.1016/j.asoc.2015.05.012.

11. Mason K., Duggan J., Howley E. Multi-objective dynamic economic emission dispatch using particle swarm optimisation variants. *Neurocomputing*, 2017, vol. 270, pp. 188-197. doi: https://doi.org/10.1016/j.neucom.2017.03.086.

12. Mason K., Duggan J., Howley E. A multi-objective neural network trained with differential evolution for dynamic economic emission dispatch. *International Journal of Electrical Power & Energy Systems*, 2018, vol. 100, pp. 201-221. doi: https://doi.org/10.1016/j.ijepes.2018.02.021.

13. Mirjalili S., Lewis A. The whale optimization algorithm. *Advances in Engineering Software*, 2016, vol. 95, pp. 51-67. doi: https://doi.org/10.1016/j.advengsoft.2016.01.008.

14. Hassan M.K., El Desouky A.I., Elghamrawy S.M., Sarhan A.M. A Hybrid Real-time remote monitoring framework with NB-WOA algorithm for patients with chronic diseases. *Future Generation Computer Systems*, 2019, vol. 93, pp. 77-95. doi: https://doi.org/10.1016/j.future.2018.10.021.

15. Basu M. Particle swarm optimization based goal-attainment method for dynamic economic emission dispatch. *Electric Power Components and Systems*, 2006, vol. 34, no. 9, pp. 1015-1025. doi: https://doi.org/10.1080/15325000600596759.

16. Basu, M. (). Dynamic economic emission dispatch using evolutionary programming and fuzzy satisfying method. *International Journal of Emerging Electric Power Systems*, 2007, vol. 8, no. 4, Article 1. doi: https://doi.org/10.2202/1553-779X.1146.

17. Alsumait J.S., Qasem M., Sykulski J.K., Al-Othman A.K. An improved pattern search based algorithm to solve the dynamic economic dispatch problem with valve-point effect. *Energy Conversion and Management*, 2010, vol. 51, no. 10, pp. 2062-2067. doi: https://doi.org/10.1016/j.enconman.2010.02.039.

Received 03.11.2020
Accepted 13.12.2020
Published 05.04.2021

Muhammad Faizan Mehdi[1], *MS in Electrical Engineering*,
Aftab Ahmad[1], *Professor*,
Syed Sadam Ul Haq[1], *MS in Electrical Engineering*,
Muhammad Saqib[1], *MS in Electrical Engineering*,
Mian Farhan Ullah[2], *Engineer, Junior Lecturer*,
[1] Department of Electrical Engineering,
University of Engineering and Technology, Taxila, Pakistan,
e-mail: faizan.mehdi8545@gmail.com,
aftab.ahmad@uettaxila.edu.pk, ssadamulhaq@gmail.com
engrsaqibkhan93@gmail.com
[2] Department of Electrical Engineering,
Wah Engineering College, University of Wah,
Quaid Avenue, Wah Cantt, Rawalpindi District,
Punjab 47040, Pakistan,
e-mail: farhan.ullah@wecuw.edu.pk

How to cite this article:
Mehdi M.F., Ahmad A., Ul Haq S.S., Saqib M., Ullah M.F. Dynamic economic emission dispatch using whale optimization algorithm for multi-objective function. *Electrical Engineering & Electromechanics*, 2021, no. 2, pp. 64-69. **doi: 10.20998/2074-272X.2021.2.09.**

Матеріали приймаються за адресою:
Кафедра "Електричні апарати", НТУ "ХПИ", вул. Кирпичова, 21, м. Харків, 61002, Україна
Електронні варіанти матеріалів по e-mail: a.m.grechko@gmail.com

Довідки за телефонами: +38 050 653 49 82 Клименко Борис Володимирович
+38 067 359 46 96 Гречко Олександр Михайлович

Передплатний індекс: 01216